DESCRIBING THE GLOBAL DISTRIBUTION AND HEALTH RESPONSE OF PARTICULATE MATTER USING MODERN COMPUTATIONAL TOOLS

by

Colin Lee

Submitted in partial fulfillment of the requirements
for the degree of Doctor of Philosophy

at

Dalhousie University
Halifax, Nova Scotia
August 2020

I dedicate this thesis to my wife, whose name I'm sure I knew at some point, but which information has been displaced by knowledge more important to the completion of this thesis.

Table of Contents

List of Tables

List of Figures

Abstract

Atmospheric aerosols have important impacts on climate and human health. This thesis advances our knowledge of the 3-dimensional distribution of atmospheric aerosols by using state of the art tools and methods to new fields or new sources of data in three applications.

First, I use adjoint modeling to provide the global health response to fine particulate matter with a diameter < 2.5 µm ($PM_{2.5}$) by implementing the Global Burden of Disease Project's Integrated Response Function. The response of global mortality to changes in local unit-mass anthropogenic emissions varied spatially by several orders of magnitude; the largest reductions in mortality for a $1\,\mathrm{kg\,km^{-2}\,yr^{-1}}$ decrease in emissions were for ammonia and carbonaceous aerosols in Eastern Europe. When comparing relative responses, the greatest reductions in mortality for a 10% decrease in emissions were found for secondary inorganic sources in East Asia.

Next, I applied the same adjoint to assimilate CALIOP Lidar profiles. Comparing mean extinction height (Z_α) between the baseline simulation and two optimised simulations to CALIOP observed Z_α, both optimisations improved the slope and offset of a linear fit across AEROCOM regions, but optimising initial conditions improved agreement ($R = 0.78$) compared to the baseline ($R = 0.72$) while optimising emissions decreased agreement ($R = 0.65$). In a global comparison of AOD, the optimised emissions greatly improved agreement with observations in the Sahara in January, but failed to capture the overall underestimate of AOD seen almost everywhere.

Finally, I used the modern machine learning framework Tensorflow to compute a high resolution ($0.01^\circ \times 0.01^\circ$) map of probability distributions of $PM_{2.5}$ fitted to ground monitoring data from the World Health Organization's cities database. This model achieved an average correlation R^2 of 0.93 and an average RMSD $= 5.00$ µg $\mathrm{m^{-3}}$ in 10-fold cross validation. Because the model outputs probability distributions at each grid location, I was able to calculate a global probability density function for population exposure to $PM_{2.5}$. Based on the global PDF, 83% of the world's population exceeds the WHO guideline of 10 µg $\mathrm{m^{-3}}$.

List of Abbreviations and Symbols Used

4DVAR	4-dimensional variational data assimilation
AE	Ångstrom exponent
AERONET	Aerosol Robotic Network
AF	Attributable Fraction; the additional premature mortality resulting from $PM_{2.5}$ exposure
AOD	Aerosol optical depth; also aerosol optical thickness
AOT	Aerosol optical thickness; also aerosol optical depth
AR	Intergovernmental Panel on Climate Change Assessment Report
CALIOP	Cloud-Aerosol LIdar with Orthogonal Polarization
CTM	Chemical transport model
FV3	Finite-Volume Cubed-Sphere Dynamical Core
GBD	Global Burden of Disease Project
GCHP	GEOS-Chem High Performance
GEMM	Global Exposure Mortality Model
GEOS	Goddard Earth Observation System
GEOS-FP	Goddard Earth Observation System – Forward Processing
GMAO	NASA Global Modeling and Assimilation Office
IER	Inegrated Exposure Response
IPCC	Intergovernmental Panel on Climate Change
ISORROPIA	"Equilibrium" in Greek; a thermodynamic equilibrium aerosol model

KPP	Kinetic preprocessor
L2	Second level of processing of CALIOP lidar profiles
lidar	light detection and ranging
MERRA	Modern-Era Retrospective analysis for Research and Applications
MISR	The Multi-angle Imaging SpectroRadiometer
ML	Machine Learning
MODIS	Moderate Resolution Imaging Spectrometer
MODIS	Moderate Resolution Imaging Spectroradiometer
NAAPS	Navy Aerosol Analysis and Prediction System
NASA	National Aeronautics and Space Administration
NWP	Numerical Weather Prediction
OI	Optimal Interpolation
$PM_{2.5}$	Particulate matter with an aerodynamic diameter < 2.5 µm suspended in air
RPMARES	An implementation of the MARS-A scheme of Binkowski and Roselle (2003)
RR	Relative Risk or Risk Ratio; the ratio of the probability of mortality of an exposed group compared to the unexposed group
SO_4	Sulphate
SSA	Single scattering albedo
TLM	Tangent Linear Model

TMRE	Theoretical minimum risk exposure; the exposure level below which it is impossible to discern an effect
TPCORE	The GMI-CTM implementation of the Flux Form Semi-Lagrangian dynamical transport scheme of Lin and Rood (1996)
VOC	Volatile organic carbon
WHO	World Health Organization

Acknowledgements

First, I would like to apologize for the perfunctoriness of these acknowledgements. Anyone mentioned herein will know me well enough to understand that I am not very good at this kind of thing, and I thank them all for that understanding.

I would like to thank my supervisor, Dr. Randall Martin.

Secondly, I would like to thank Dr. Daven Henze, who wrote the original adjoint of GEOS-Chem. His advice and guidance have made much of this work possible.

I would like to thank my committee, Drs. Jeffrey Pierce and Ian Folkins for their support and guidance. In particular, I would like to thank Dr. Pierce for all the effort he put in to help me get across the finish line (I hope).

I would also like to thank Dr. Thomas Trappenberg in the Computer Science department, and his student Will Stone, with whom I conferred while conceiving the machine learning project.

I would also like to thank many students, researchers, and technicians in both those professor's research groups for providing guidance, intellectual stimulation and comradery. In particular, Brian Boys, Crystal Weagle, Forrest Lacey, Chi Li, Jun-wei Xu, Betty Croft, Aaron van Donkelaar, Melanie Hammer, Matt Cooper, Jun Meng, Nat Knight, Andy Morrow, Graydon Snider, Shailesh Kharol, Sajeev Philip, Sara Torbatian, Akhila Padmanabha and probably others I am forgetting.

Finally I would like to thank my family and friends, for putting up with me being a student for so long.

Chapter 1

Introduction

One of the most widely studied air pollutants are suspended particles with an aerodynamic diameter less than 2.5 µm ($PM_{2.5}$). This size cutoff falls at a trough in a typical ambient atmospheric volume distribution, roughly between the accumulation and coarse modes (Seinfeld and Pandis, 2016, p. 342). Extensive in situ monitoring of $PM_{2.5}$ occurs around the globe but coverage is uneven, with dense monitoring available in populated areas in North America, Europe, and more recently Asia, but poor coverage even in densely populated regions in Africa and South America, along with very little coverage in remote regions and over the ocean.

1.1 Background and Motivation

1.1.1 Human Health and Environment

Particulate matter has direct impacts on climate, with some aerosols such as black and brown carbon absorbing radiation, while others such as SO_4 reflect shortwave radiation back to space. Particulate matter also influences climate indirectly through increasing the number of cloud droplets (the first indirect effect) and increasing the lifetime of clouds (the second indirect effect) (Boucher et al., 2013b). Because of these different impacts, the uncertainty of climate forcing associated with $PM_{2.5}$ is large; even as recently as the IPCC 5th Assessment Report, the 95% confidence interval included zero, indicating uncertainty as to not only the magnitude but also the direction of the forcing (Boucher et al., 2013b). This thesis does not focus on climate impacts, but it is worth mentioning them, as any improvement in modeling the 3D distribution of aerosols stands to improve our understanding on their impact on climate.

As Chapter 2 assumes a certain background knowledge in epidemiology, I will briefly describe a few terms and concepts which may not be familiar to atmospheric

scientists. The additional risk of a negative outcome (such as mortality) caused by exposure to a risk factor is usually quantified with a relative risk or risk ration, RR. This is the ratio of probability of the negative outcome at the exposed level to the probability of the outcome in the unexposed population (Porta, 2016). These relative risks are computed by gathering data about exposure levels and health outcomes, and comparing the outcomes between differently exposed populations. Frequently RRs are reported for inter-percentile ranges; for example, the RR of mortality for an interquartile range would be the probability of mortality in the group at the 25^{th} percentile of exposure divided by the probability of mortality at the lowest exposure. If the relationship between RR and exposure is a continuous function, this is often referred to as a health impact function or exposure response curve. The excess mortality caused by exposure to a risk factor is called the attributable fraction, which is similar to a population-weighted RR based on the population exposure(Prüss-üstün et al., 2003):

$$AF = \frac{\int P(x)RR(x)dx - 1}{\int PxRRxdx} \tag{1.1}$$

The AF can be multiplied by the baseline mortality to get the attributable deaths or response of mortality; this can lead to a situation where the two populations with the same exposure have different mortality responses because their baseline mortalities differ.

Epidemiologic research has associated $PM_{2.5}$ with human health impacts including cardiovascular disease, stroke, Alzheimer's, stroke, and cancer. The first study to show a connection between $PM_{2.5}$ and health was the Harvard Six Cities Study (Dockery et al., 1993), which found a strong association with mortality by assigning a single $PM_{2.5}$ concentration to all people in each city. This is obviously a very coarse metric, as $PM_{2.5}$ concentrations vary significantly in space even down to the hundreds of metres scale, especially for traffic-related sources (Franklin et al., 2018). Additionally, the $PM_{2.5}$ concentrations recorded for each city only ranged from 11–29 $\mu g/m^3$, which led to much discussion about the shape of the response function at higher concentrations, such as those seen in Asia (Krewski et al., 2009; Burnett et al., 2014; Nasari et al., 2016; Vodonos et al., 2018; Burnett et al., 2018). Recently, the concentration response function has been extended to much lower concentrations as well, showing an association with cardiovascular mortality down to below

5 µg/m^3(Pappin et al., 2019; Pope et al., 2019).

On the exposure side, new cohorts (groups of patients whose $PM_{2.5}$ exposure and health outcomes have been recorded), especially with a broader range of exposure levels from different parts of the world have emerged, although Africa and South America remain underrepresented. The Integrated Exposure Response (IER) model was able to increase the range of the available exposure data by including indoor air pollution (which can reach orders of magnitude higher than typical ambient concentrations) and smoking (Burnett et al., 2014). This meta analysis was able to extend the response curve to the high levels experience by people in East Asia, and was used as the basis for the Global Burden of Disease (GBD) Project's estimate of the global burden of disease due to exposure to ambient $PM_{2.5}$. The GBD estimate for global $PM_{2.5}$-related premature mortality for 2017 is 3.5 million people (http://ghdx.healthdata.org/gbd-results-tool; GBD 2017 Risk Factor Collaborators, 2018). The main drawback of the method is the assumption that indoor $PM_{2.5}$ and cigarette smoking have the same exposure response on mortality as ambient $PM_{2.5}$.

The most recent attempts to reconstruct the response curve include another meta analysis, using mainly the averages of 53 studies of ambient $PM_{2.5}$ exposure to extend the curve out to > 40 µ/m^3, and the Global Exposure Mortality Model (GEMM) which includes cohorts with exposures from 0.9 µ/m^3(Crouse et al., 2015) to 83.8 µ/m^3(Yin et al., 2017)). The Yin et al. (2017) study concluded that the GBD may have underestimated ambient $PM_{2.5}$ mortality by 20%, but this value relies heavily on the single study with the high exposure and is reduced to 6% when that one study is excluded from the analysis (Burnett et al., 2018). The GBD project goes to great lengths to ensure that the sum of mortality from each risk factor does not exceed the observed total mortality, and thus, it seems this extra 20% mortality will have to come from other risk factors if GBD chooses to update their methods.

From a policy perspective, the main goal of determining the exact shape of the exposure response curve is to determine the human health impact of $PM_{2.5}$ exposure, and provide a path for mitigation. Since $PM_{2.5}$ has many and complex sources, not all of them even under human control, it may well be very costly to decrease exposure levels. Therefore, cost-benefit analyses are required, and the benefit side of the equation requires confidence in the shape of the response curve.

Ultimately, the assessment of human exposure to $PM_{2.5}$ and from that, the shape of the exposure response curve, and the mitigation of health impacts, relies on high-quality, high-resolution estimates of surface $PM_{2.5}$ concentrations (Punger and West, 2013). These high-resolution estimates are the focus of this thesis, and the following subsections focus on the chemistry/physics of $PM_{2.5}$ and the generation of these estimates.

1.1.2 Exposure Modeling

Because measuring $PM_{2.5}$ is difficult and expensive, it is impossible to monitor everybody's exposure directly. Exposure assessment typically assumes that the bulk of each person's exposure is determined by the average outdoor $PM_{2.5}$ concentration at their residence, although this is changing as time-activity and microenvironment exposure are beginning to be considered in the literature (e.g., Malley et al., 2020; Evangelopoulos et al., 2020; Richmond-Bryant and Long, 2020). Modern exposure modeling is usually based on a combination of geophysical modeling in combination with in situ monitoring and remote sensing. This combination is driven by the shortcomings of each of the components: in situ monitoring is sparse compared to the spatial variability of $PM_{2.5}$ concentrations and population (Martin et al., 2019); although satellite remote sensing data provides more coverage than in situ monitoring, it can be difficult to interpret; and while geophysical modeling provides unlimited coverage, models have difficulty accurately reproducing existing measurements. Therefore the "best" estimates combine these sources of data to produce computationally tractable, high-resolution, high-accuracy exposure estimates (Brauer et al., 2012).

1.1.3 Aerosol Sources, Sinks and Microphysics

Aerosols can be emitted directly; these are called primary aerosols. They can also be created by the condensation of vapours, usually after chemical conversion to a less volatile form than the original emitted gas, which are called secondary aerosols. The common types of primary emissions are carbonaceous particles such as soot, usually created from combustion, sea-spray aerosols, and mineral dust. Secondary aerosols are formed from inorganic compounds such as sulphate, nitrate and ammonia, or organic compounds which are oxidised and condense out (Seinfeld and Pandis, 2016).

Natural Sources

Aerosols emitted directly by natural processes include dust, sea-salt and primary carbonaceous aerosols. Dust comes mostly from desert regions. Winds lift larger particles ($\sim$ 100 µm; Alfaro et al., 1997), but because of their weight they tend to be deposited quickly and thus do not usually contribute greatly to atmospheric aerosol. The dust that survives to be transported long distances is usually created through a process called saltation, whereby larger particles transfer their momentum to smaller particles when they impact the surface (Zender et al., 2003; Ju et al., 2018; Martin et al., 2018; Ferreira et al., 2019). Sea-spray aerosol is created by splashed droplets of sea water evaporating. These droplets can be created when waves entrain air into the top layer of the ocean, then these bubbles rise to the surface and pop, creating many tiny droplets. Primary carbonaceous aerosols such as soot, black carbon, elemental carbon (frequently used as synonyms, although there a connotational differences), and organic carbon are created by combustion processes. The main natural source of primary carbonaceous aerosols is wild fires(Brewer et al., 2019).

Aerosol precursors, usually organic compounds, can also come from natural sources. In the marine environment, biogenic activity in the surface layer can release volatile organic compounds which either themselves condense to form aerosols, or their oxidation products do (Petters et al., 2010). Plants can also release volatile and semi-volatile organic species such as terpenes, which can condense or oxidise to condensable products. A well-known example of this is the Great Smoky Mountains in the United States (Blando et al., 1998). The The Model of Emissions of Gases and Aerosols from Nature (MEGANv2.1) inventory estimates global biogenic VOC emissions at 760 Tg C yr^{-1} (Sindelarova et al., 2014).

Anthropogenic Sources

Carbonaceous aerosols are the most important primary anthropogenic emissions. They can be generated by human activities such as fossil fuel and biomass combustion. Dust is emitted by human activities including soil disturbance due to land-use changes, resuspension of road dust by traffic, and industrial processes (Pouliot et al., 2012; Philip et al., 2017). At present, I am unaware of any models that include anthropogenic activity in the calculation of sea spray aerosols. Any impacts caused by

ships, turbines or human structures such as breakwalls, engineered beaches or bridges would have a very small impact compared to the natural sources. However, one solar radiation management idea which has been proposed to mitigate the impacts of climate change is marine cloud brightening or sea spray geoengineering(e.g., Latham et al., 2012; Partanen et al., 2012, 2016), so in future a significant amount (up to 17% of total emissions, or up to 10 times the natural source of the fraction below 2.5 µm) of sea spray may be anthropogenic (Horowitz et al., 2020).

Secondary organic aerosols can also be created by anthropogenic activity that generates volatile organic carbon (VOC). These gases and semi-volatile species can be generated by fossil fuel combustion, industrial processes such as fuel refining, paint solvents, waste processing, and biomass burning. Anthropogenic emissions are a small fraction of biogenic VOCs(Glasius and Goldstein, 2016), although in some parts of the world they may contribute up to half of regional VOC emissions (Chaliyakunnel et al., 2019).

Many anthropogenic aerosols are formed by the condensation of inorganic precursor gases. The main secondary inorganic precursor gases are SO_2 or sulphur dioxide, NO_x or nitrogen oxides, and NH_3 or ammonia. These are oxidized to SO_4, NO_3, and NH_4, sulphate, nitrate and ammonium, which are the main inorganic constituents of $PM_{2.5}$. Although there are many sources of these inorganic precursor gases, each tends to be associated with a different subset of human activities.

Anthropogenic SO_2 comes mainly from coal and oil burning for industrial processes and energy generation; the EDGAR emission inventory (Crippa et al., 2018), which is used in GEOS-Chem, estimates 51.5 Tg S yr^{-1} of global anthropogenic SO_2 emissions. Anthropogenic NH_3 is primarily emitted by agricultural practices; EDGAR estimates global NH_3 emissions from fertilizer and animal waste at 33.3 Tg N yr^{-1}(Aneja et al., 2020). Anthropogenic NO_x is usually associated with traffic, as well as all the previously mentioned sources; EDGAR estimates global anthropogenic NO_x emissions to be approximately 50 Tg N Yr^{-1}. Because of of its reactiveness and loss processes which tend to be collocated, large uncertainties (11 Tg N yr^{-1}) have been reported(Beusen et al., 2008).

1.2 Tools and Methods

In this thesis, I used 3 main computation tools: the GEOS-Chem chemical transport model, the adjoint of GEOS-Chem, and the Tensorflow machine learning framework. I used GEOS-Chem and its adjoint to compute sensitivities of global $PM_{2.5}$-related mortality to aerosol precursor emissions and to perform data assimilation on CALIOP lidar profiles, while I used Tensorflow to produce a high-resolution map of surface $PM_{2.5}$ distributions from geospatial and remote sensing data, which I trained and verified with surface $PM_{2.5}$ monitoring data from the World Health Organization (WHO) Cities Database.

1.2.1 Chemical Transport Modeling Using GEOS-Chem

Computer numerical modeling provides a number of advantages in studying the 3D distribution of aerosols. Models allow us to fill in gaps in the uneven distribution of surface monitoring networks, aid in interpreting satellite remote sensing data, and allow us to account for the complex dynamical nature of the atmosphere. All these help us to understand and predict the 3D distribution of aerosols, and its sensitivity to exogenous factors such as emissions and meteorology.

To perform the work presented in this thesis I used GEOS-Chem, a chemical transport model (CTM). First released in 2001(Bey et al., 2001), the model has undergone many improvements and is currently on version 12(The International GEOS-Chem User Community, 2020). The model runs globally at $4^\circ \times 5^\circ$ or $2^\circ \times 2.5^\circ$ resolution, and regionally at up to $\frac{1}{4}^\circ \times \frac{3}{8}^\circ$ resolution in nested grids over North America(Kim et al., 2015), Europe(Protonotariou et al., 2010), East Asia(Wang et al., 2004; Chen et al., 2009; Zhang et al., 2015b) and West Africa. Recently, the ability to run parallelized across many processors was added, and is referred to as GEOS-Chem High Performance (GCHP) (Eastham et al., 2018).

GEOS-Chem takes as input mainly two kinds of data: meteorological data and emissions data. Many changes have occurred to both systems over the lifetime of GEOS-Chem.

Meteorological inputs are generally from assimilated meteorological data from the Goddard Earth Observation System (GEOS) of the NASA Global Modeling and

Assimilation Office (GMAO), that is, satellite and other observational data are assimilated using a 3D- or 4D-variational process and the resulting optimised model output is archived. GEOS-Chem has used GEOS-4, GEOS-5, GEOS-FP, and MERRA meteorology. GEOS-4 data is from an older version of the GEOS model and is now obsolete. The archives go from 1985 to 2007. GEOS-5 is also obsolete and data is available for 2003 to 2013. The current operational assimilated meteorology archive is GEOS-FP, which uses the GEOS-5 model and goes from 2012 to present. The Modern-Era Retrospective analysis for Research and Applications (MERRA) is a reanalysis which provides consistent historical data back to 1979, up until 2008(Rienecker et al., 2008, 2011). MERRA-2, which supersedes MERRA, goes from 1979 to present (Randles et al., 2017). This meteorological data is used to drive the TPCORE advection algorithm (Lin and Rood, 1996) in older versions of GEOS-Chem or the new FV3 algorithm in GCHP, because it uses a different gridding scheme (Putman and Lin, 2007).

Emissions data for GEOS-Chem has come from a variety of sources. The emissions inventories are typically compiled from the bottom up, that is, the emissions are computed from reported values for burned fuels or energy consumption multiplied by emissions factors. GEOS-Chem includes emissions of gases and particles from anthropogenic activities, including energy generation, industry, transportation, shipping, aircraft, trash burning, and other diffuse and inefficient sources, and natural source, including lightning, volcanoes, oceans, and the biosphere.

Mineral dust emissions and sea spray aerosol emissions are two natural emissions processes are of particular importance to Ch. 3 of this thesis, because it deals with optimising global aerosol emissions and a large fraction of the Earth's surface is covered by ocean or desert, and also because I implemented the adjoint of the sea spray portions of the model as part of this work. Both of these processes are the result of meteorology-dependent physical processes and are usually parametrized as a function of wind-speed in transport models.

In GEOS-Chem, the dust emissions scheme is based on the Dust Entrainment and Deposition (DEAD) scheme (Zender et al., 2003). This scheme parametrises dust emissions (F_d) as a linear function of frictional wind speed (u_*) in excess of a threshold velocity (u_{*t}) modulated by a sand blasting efficiency (α) which depends

only on soil characteristics (Alfaro et al., 1997):

$$F_d = \begin{cases} \frac{\alpha c_s \rho u_*^3}{g} \left(1 - \frac{u_{*t}}{u_*}\right) \left(1 + \frac{u_{*t}}{u_*}\right), & u_* > u_{*t} \\ 0, & u_* \leq u_{*t} \end{cases} \tag{1.2}$$

where c_s is an empirical constant determined in lab studies (White, 1979), ρ is air density, and g is the acceleration of gravity.

The sea spray aerosol scheme is the Gong (2003) scheme as implemented by Jaeglé et al. (2011). The shape of the size-dependent emissions curve is given by

$$\begin{aligned} B &= \frac{(0.380 - \log r)}{0.650} \\ \frac{dF_0}{dr} &= 1.373 u_{10}^{3.41} r^3 \left(1 + 0.057 r^{1.05} \times 10^{1.19 e^{-B^2}}\right) \end{aligned} \tag{1.3}$$

where u_{10} is the wind speed at 10 m above sea surface, and r is the particle radius at 80% RH.

In GEOS-Chem, chemistry is performed by the kinetic preprocessor (KPP) (Damian et al., 2002). In short, chemical mechanisms are specified in a special KPP language file, which the KPP system converts into FORTRAN code for the time derivative, the Jacobian, and code for numerical integration of the partial differential equations.

Gas-aerosol thermodynamic equilibrium of sulphate, nitrate and ammonium was performed by the RPMARES algorithm in older versions of GEOS-Chem (Binkowski and Roselle, 2003). For version 8-03-01 and after, the algorithm was changed to ISORROPIA-II, which describes thermodynamic algorithm for many species (Fountoukis and Nenes, 2007), although only sulphate, nitrate and ammonium were implemented in GEOS-Chem(Pye et al., 2009).

1.2.2 Surface In Situ Monitoring of Aerosols

The simplest way to measure $PM_{2.5}$ is gravimetric analysis, where air is drawn through a filter at a known rate and the mass of the filter is compared before and after. The filters can also be submitted to other analysis including light reflection, transmission, and diffraction, and destructive chemical analysis to determine the composition of the particles. Gravimetric analysis is complicated by various factors including obtaining accurate measures of the air flow rate, filter size and chemical selectivity, temperature (which can drive condensation and evaporation of particles after capture), and

humidity (which can change particle size after capture).

In the context of exposure science and comparison to model or remote-sensing data, it is worth pointing out that most in situ measurements are point measurements, that is, they represent only a very small spatial area, compared with model grid cells and satellite pixels which can be 10s to 100s of km on a side. Most people do not live right next to a sampling station inlet and so there is always the question of how representative a point measurement is for a given application.

1.2.3 Remote Sensing of Aerosols

Overview

Particulate matter interacts with electromagnetic radiation. Remote sensing is the indirect detection of aerosol through measuring light emitted by, scattered by, or transmitted through an air mass. At their roots, remote sensing algorithms are based on the observation that the transmission of light, $t(\lambda)$, through a solution, gas, or aerosol is a function of the path length, L, and the concentration, c, and extinction cross section, σ_λ, of the species. Mathematically, this is formulated as Beer-Lambert-Bouger law:

$$t(\lambda) = \frac{I(\lambda)}{I_0(\lambda)} = e^{-L\sigma\lambda c} \tag{1.4}$$

By comparing the source radiance (the sun in the case of passive remote sensing, or a known source in the case of active instruments) with the received radiance, the concentration of aerosols can be inferred given certain assumptions about path length and the composition and location of the aerosols. Remote sensing instruments can be placed on the ground, on towers, on aircraft, or on satellites. There are many viewing geometries available, but a few common ones have importance. Ground instruments looking directly up are called zenith viewing. Satellite-borne instruments that are facing directly down are called nadir viewing, and instruments which point across the atmosphere are called limb viewing.

In reality, remote sensing of aerosols is complicated by several factors: the concentration is rarely, if ever, uniform over the entire path; aerosols are not the only species causing extinction; aerosols may interact differently with different wavelengths of light; extinction is affected by aerosol shape, size, and composition; in the case of

satellites, the light source is typically reflected off the surface of the Earth rather than directly transmitted to the sensor. A number of factors and parameters are used to handle these situations when performing retrievals.

Some important aerosol optical properties are the extinction, absorption, and scattering cross sections, the extinction, absorption, and scattering efficiencies, which are the ratios of the cross sections to the true size of the particle, the single-scattering albedo (SSA), which is the ratio of the scattering cross section to the absorption cross section, and the scattering phase function which measures the fraction of radiation scattered as a function of the difference in angle from the incident angle of the radiation. The total measure of extinction along a path is called the aerosol optical depth (AOD) or optical thickness (AOT); this is the integral of the extinction coefficient ($\tau = \sigma c$ in equation 1.4). All of these parameters vary with wavelength. A measure of how AOD varies with wavelength is the Ångström exponent (AE) and is represented by α in the following equation:

$$\frac{\tau_{\lambda_1}}{\tau_{\lambda_0}} = \left(\frac{\lambda_0}{\lambda_1}\right)^{\alpha} \tag{1.5}$$

Remote Sensing Instruments Used in This Thesis

One of the most important and longest running sources of global AOD measurements is the Aerosol Robotic Network (AERONET; Holben et al., 1998). AERONET is a surface-based network of instruments which measure solar radiation by automatically following the sun. The largest difficulty with AERONET measurements is filtering cloud contamination while retaining real aerosol events which might appear like clouds to screening algorithms (Smirnov et al., 2000). Recent updates to the algorithm have improved this but difficulties still remain (Giles et al., 2019).

The Multi-angle Imaging SpectroRadiometer (MISR) was launched aboard the NASA Terra satellite in December of 1999. The sensor has 4 forward-, one nadir-, and 4 aft-facing cameras which measure the same spot on the ground at 9 different angles over a span of 7 minutes. The cameras measure 4 wavelengths (446.6, 557.5, 671.7, and 866.4 nm). The retrieval was recently updated from v22, the standard since 2007, which uses two different algorithms for land (Martonchik et al., 2009) and deep water (Kalashnikova et al., 2013). V23 also uses different algorithms over land and water, but went from 17.6 km to 4.4 km resolution and improved cloud

screening and contamination from snow-covered surfaces and whitecap waves (Garay et al., 2020).

The Moderate Resolution Imaging Spectrometer (which is inexplicably abbreviated as MODIS) is a pair of 32-wavelength instruments which fly aboard NASA satellites Aqua and Terra (SALOMONSON et al., 1989). The atmosphere product consists of 3 separate algorithms: the Deep Blue(Hsu et al., 2013) and Dark Target(Levy et al., 2013) algorithms over land, and a separate Dark Target algorithm over water. In the most recent collection, the science team has also been producing a combined product which includes information from all 3 algorithms (Sayer et al., 2014).

The Cloud-Aerosol LIdar with Orthogonal Polarization (CALIOP) instrument is a space-borne lidar aboard the Cloud-Aerosol Lidar and Infrared Pathfinder (CALIPSO) satellite, launched in 2006 (Winker et al., 2009). Unlike MODIS and MISR, CALIOP is an active remote sensing platform. Light detection and ranging (lidar) is a distance-resolved active sensing technique which involves firing short pulses of collimated light and measuring the strength of the reflected signal over time. This time is used to infer the distance at which the reflection occurred (Wandinger, 2005). This provides obvious advantages in studying the 3D distribution of aerosols; however, the active nature of the measurement also means that the horizontal spatial coverage is sparse, providing only 14 overpasses roughly-75 m-wide on the ground per day. Interpreting lidar data can be difficult because the lidar equation can be both under- and over-constrained at the same time. A space-borne lidar increases the difficulty as the low-power requirements mean a low signal-to-noise ratio, especially on the daytime leg of the orbit (Winker et al., 2009).

1.2.4 Inverse Modelling and Data Assimilation

As we have seen above, both models and measurements have strengths and shortcomings, and all modeled or measured values are uncertain to some degree. Data assimilation is the process of combining models and measurements to determine the boundary conditions, which allows the model to best reproduce those measurements while properly accounting for uncertainties in the model state and measurements. There are many “flavours” of data assimilation (i.e., optimal interpolation (OI), Kalmann

filtering, 3D- and 4D-variational, as well as empirical methods such as the successive corrections method and nudging), but they are all mathematically equivalent under certain assumptions or by limiting the analysis to certain dimensions (Kalnay, 2003). Although the different methods are mathematically equivalent, they each hold different assumptions and their applications may be more or less suitable to certain operational situations. I chose 4D-Variational (4DVAR) data assimilation for use in this thesis, because of the availability of an adjoint model for GEOS-Chem (Henze et al., 2007), which is a requirement for 4DVAR.

Data assimilation has been in use in oceanography and for numerical weather prediction (NWP) for many decades (Talagrand, 1997). The idea is to find an analysis, $\mathbf{x_a}$, that combines the background, $\mathbf{x_b}$, or "first guess" field with observations, $\mathbf{y_o}$, sometimes using an observational operator, H, to transform the model variables into the observation space, e.g., if the observations are radiances, H would be a radiative transfer model:

$$\mathbf{x_a} = \mathbf{x_b} + \mathbf{W}(\mathbf{y_o} - H(\mathbf{x_b})) \tag{1.6}$$

The optimal weights, $\mathbf{W}$, also called the gain matrix in Kalmann filtering, are found by analogy to a least-squares, maximum-likelihood, or maximum a priori analysis:

$$\mathbf{W} = \mathbf{B}\mathbf{H}^T \left(\mathbf{R} + \mathbf{H}\mathbf{B}\mathbf{H}^T\right)^{-1} \tag{1.7}$$

where $\mathbf{B}$ is the background error covariance matrix, $\mathbf{R}$ is the observation error covariance matrix, and $\mathbf{H}$ is the linearised observational operator.

4DVAR provides a model analysis (i.e., the optimised model output) which is completely consistent with the model equations. The algorithm does this by optimising the model boundary conditions such as the initial state of the atmosphere or physical production and loss (i.e., emission and deposition) so that the model run best reproduces the observations at the time the observations occur, subject to the uncertainties in the model and observations. Boundary conditions are optimised through an iterative gradient-descent algorithm, which minimizes a scalar-valued cost function of the model output. In most situations, this will be a weighted sum of squared differences between the model fields and the observations, where the weights are provided by the error covariance matrices.

In order to perform a gradient-descent optimisation, a gradient is required. This

is provided by a complimentary set of model equations called the adjoint. Mathematically, the adjoint is the transpose of the tangent linear model (TLM), which is the model equations linearized about the local model state (Wang et al., 2001). In practice, this means running the forward model equations backwards in time (it is possible to run the adjoint forwards in time but the memory requirements become prohibitive for realistic models).

The adjoint model of GEOS-Chem has existed since 2007 (Henze et al., 2007). This model allows for the calculation of the local sensitivities of scalar-valued cost functions with respect to model initial conditions or emissions. The adjoint model includes full chemistry and transport for SIA (Henze et al., 2009). By extending the model code, I used the adjoint of GEOS-Chem to compute the sensitivities of global mortality to $PM_{2.5}$ and precursor gas emissions in Chapter 2 and to perform 4DVAR assimilation of CALIOP lidar profiles in Chapter 3.

1.2.5 Machine Learning

In Chapter 4 I use the Machine Learning (ML) framework Tensorflow to generate global high-resolution maps of probability distributions of $PM_{2.5}$. Machine learning is a broad and vague term, but generally it is is the process of determining the parameters to some function or algorithm that can approximate some unknown function. The parameters are inferred from data, typically very large sets of data, often through some iterative process. A popular method is deep learning, which is based on deep artificial neural networks.

Artificial neural networks are ostensibly modeled on biological neurological systems. An artificial neuron outputs some function of a weighted sum of its inputs (Rumelhart et al., 1986). A network is divided into layers, which are groups of neurons that operate on the output of the previous layer. Data is fed into the network as a vector of all the input variables; this is called the input layer. The input layer is followed by one or more layers of artificial neurons. If artificial neurons have many inputs from the preceding layer, the network is said to be dense. If a network has multiple layers it is described as deep.

Supervised learning is the process of training a machine learning model with labeled data, i.e., a dataset where both the input and output are known. Neural networks are trained by computing some objective function on their input; for numerical data, this is typically the sum of squared difference between the network's output and the data you wish to match. The weights of the individual neurons are then tuned, usually through an iterative gradient descent. In this method, the network is initialized with random weights, and the output is computed for some subset of the available training data. The objective function is then computed on that output and the known target values for those samples. The local gradient of the cost function with respect to the artificial neurons are calculated and each weight is adjusted in the negative direction. The process is repeated, usually with different subsets of the training data, until the objective function converges to a stable value. To ensure the training is not "overfitting" the training data, another set of labeled data is withheld from the training process, the evaluation data.

Recently the inevitable increase in computing power due to Moore's law (Moore, 1998) combined with publicly available frameworks such as KERAS, Torch and Tensorflow, has lead to a renaissance in machine learning research, and especially in applying the tools to novel fields and problems. In the past 5-10 years there have been thousands of papers published on machine learning applied to air quality.

1.3 Structure of This Thesis

This thesis is an attempt to advance our knowledge of the 3-dimensional distribution of atmospheric aerosol by applying state of the art tools and methods to new fields or new sources of data. The subsequent chapters will comprise work already published or in preparation for publication.

Chapter 2 is published in the journal Environmental Science and Technology and focuses on using a new formulation of the exposure response function to fine particulate matter and the adjoint of GEOS-Chem to efficiently compute the response of human health impacts to changes in sources of anthropogenic aerosol. My contribution to that work consists of the FORTRAN code for computing the Integrated Exposure Response (IER) based cost function and injecting its forcing terms into the adjoint. I performed all the adjoint model runs to calculate the impacts reported, performed

the analysis, and generated all the graphics for the publication. The IER-based cost function I wrote has since been used in a publication quantifying the contributions of cookstove emissions to radiative forcing and human health effects (Lacey et al., 2017).

In Chapter 3, I apply the same tool, the adjoint of GEOS-Chem, to the task of assimilating lidar profile data from the space-borne lidar, CALIOP. In order to perform this 4DVAR data assimilation, I wrote FORTRAN code to ingest CALIOP L2 lidar profiles and compute the cost function. In addition, the adjoint code base did not include the full adjoint of sea salt. I implemented this adjoint code because CALIOP, as an active remote-sensing instrument, is not restricted to land, and sea salt is an important contributor to global aerosol distributions, contributing up to 30Pg of aerosol mass per year (Lewis and Scwartz, 2004).

The recent development of easy-to-use machine learning tools such as TensorFlow has created a boom in concentration and exposure estimation for particulate matter, (Rybarczyk and Zalakeviciute, 2018). In Chapter 4, I describe the application of recently popularized machine learning techniques to the problem of estimating global particulate matter concentrations from a sparse set of monitoring data. I implemented a Mixture of Gaussians model (Bishop, 1994) in TensorFlow to provide a high resolution (0.01°) global $PM_{2.5}$ concentration map, complete with quantitative uncertainty estimates. The model reproduces the surface monitoring dataset with similar accuracy as other recently published methods but with much lower computational cost.

The final chapter will attempt to draw some conclusions from the thesis as a whole and recommend future work to further advance the field from the these findings.

Chapter 2

Response of global particulate-matter-related mortality to changes in local precursor emissions[1]

2.1 Abstract

Recent Global Burden of Disease (GBD) assessments estimated that outdoor fine-particulate matter ($PM_{2.5}$) is a causal factor in over 5% of global premature deaths. $PM_{2.5}$ is produced by a variety of direct and indirect, natural and anthropogenic processes that complicate $PM_{2.5}$ management. This study develops a proof-of-concept method to quantify the effects on global premature mortality of changes to $PM_{2.5}$ precursor emissions. Using the adjoint of the GEOS-Chem chemical transport model, we calculated sensitivities of global $PM_{2.5}$-related premature mortality to emissions of precursor gases (SO_2, NO_x, NH_3) and carbonaceous aerosols. We used a satellite-derived ground-level $PM_{2.5}$ dataset at approximately 10 km x 10 km resolution to better align the exposure with population density. We used exposure-response functions from the GBD project to relate mortality to exposure in the adjoint calculation. The response of global mortality to changes in local anthropogenic emissions varied spatially by several orders of magnitude. The largest reductions in mortality for a 1 kg km^2 yr^{-1} decrease in emissions were for ammonia and carbonaceous aerosols in Eastern Europe. The greatest reductions in mortality for a 10% decrease in emissions were found for secondary inorganic sources in East Asia. In general a 10% decrease in SO_2 emissions was the most effective source to control, but regional exceptions were found.

[1]Reproduced with permission from Environmental Science and Technology: Lee, Colin & Martin, Randall & Henze, Daven & Brauer, Michael & Cohen, Aaron & Donkelaar, Aaron. (2015). Response of Global Particulate-Matter-Related Mortality to Changes in Local Precursor Emissions. Environmental science & technology. 49. 10.1021/acs.est.5b00873. Copyright 2015 American Chemical Society.

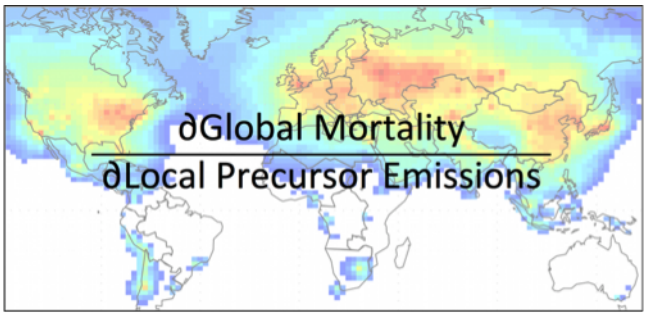

TOC/Abstract art (map boundaries from US Department of State)

2.2 Introduction

Long-term exposure to fine particulate matter with an aerodynamic diameter less than 2.5 µm ($PM_{2.5}$) is associated with morbidity and mortality(Dockery et al., 1993; Jerrett et al., 2005). $PM_{2.5}$ can be produced directly by combustion or mechanical processes, and indirectly by condensation of aerosol precursor gases. The Global Burden of Disease (GBD) project estimated that exposure to ambient $PM_{2.5}$ contributed to 3.2 million (5% of the global total) premature deaths worldwide in 2010(Lim et al., 2012). Emission control strategies can be costly and the pathways from emissions to exposure are complex(United States Environmental Protection Agency, 1999; Krupnick and Morgenstern, 2002; Cox, 2012). It is, therefore, important to determine how future changes in $PM_{2.5}$ sources would affect health outcomes. A variety of techniques have been employed to estimate the impacts of emissions on the attributable fraction of mortality due to $PM_{2.5}$ exposure(Bell et al., 2011). In general, exposure is estimated at some baseline and compared with exposure estimated after a perturbation in emissions. This comparison can be based on measured concentrations before and after a natural experiment such as the strict air-quality controls enacted for the 2008 Beijing Olympics(Li et al., 2010; Hou et al., 2010; Wu et al., 2010), or the U.S. Clean Air Act(United States Environmental Protection Agency, 1997; Chay et al., 2003). These types of studies are limited by the regional scope of the policy.

Alternatively, a chemical transport model can be used to calculate atmospheric concentrations based on different emissions scenarios. For example, Anenberg et al. (2010) used two model simulations, one with modern emissions and one with preindustrial emissions, to estimate the additional burden of disease produced by modern emissions for the whole world. West et al. (2009) perturbed NO_x emissions separately

in each of nine global regions to determine regional impacts on global O3 exposure, while Anenberg et al. (2009) similarly perturbed ozone precursor emissions together in each of five global regions. Similar methods have been used to test other specific scenarios(Liu et al., 2009; Saikawa et al., 2011). While this approach has provided valuable insights, it can be computationally prohibitive to examine more than a few specific circumstances. Adjoint models allow for the simultaneous computation of an entire field (e.g. $>$ 10,000) of responses and thus explore novel policy-relevant questions. The recent development of the adjoint of a global chemical transport model to include aerosols(Henze et al., 2007) offers an exciting opportunity to efficiently determine the responses of global mortality to changes in local emissions.

In adjoint modeling a change in the final state is transformed backwards in time to determine the sensitivities of the final state to model inputs, such as emissions. Recently, adjoint chemical transport models have been used to constrain estimates of sources of $PM_{2.5}$ (Henze et al., 2009; Wang et al., 2012; Xu et al., 2013; Koo et al., 2013). Pappin and Hakami (2013) used the gas-phase chemistry adjoint of a regional model (CMAQ) to determine the benefits of reducing emissions that contribute to trace-gas air pollutant exposure in Canada and the United States, demonstrating the utility of this novel tool in health-impact studies. The relationship between gaseous emissions and $PM_{2.5}$ concentrations is complex. The main species that result in secondary formation of inorganic $PM_{2.5}$ are sulphur dioxide (SO_2), nitrogen oxides (NO_x = NO + NO_2) and ammonia (NH_3). In the atmosphere, SO_2 is rapidly oxidized to form sulphuric acid (H_2SO_4), which readily condenses to form sulphate (SO_4^{2-}) $PM_{2.5}$. NO_x is oxidized to nitric acid (HNO_3), which can exist in the gas phase. NH_3 preferentially reacts with H_2SO_4 and remaining NH_3 will react with HNO_3 to form ammonium nitrate (NH_4NO_3) particles. The relationship between any one of the precursor gases and $PM_{2.5}$ concentrations is therefore a function of the concentrations of the others. Furthermore, secondary inorganic aerosols are part of a complex mixture of other $PM_{2.5}$ components, some of which are more readily modifiable (e.g., primary carbonaceous) than others (e.g., mineral dust, sea salt). Over the past decade SO_2 and NO_x emissions as well as $PM_{2.5}$ concentrations have decreased in North America and Europe, in contrast with increases in South Asia and East Asia(Wang et al., 2012; Klimont et al., 2013; Boys et al., 2014; van Donkelaar et al., 2015). Globally

NH_3 emissions are more uncertain and generally increasing (Galloway et al., 2008; Wang et al., 2011; Kurokawa et al., 2013).

Here, we introduce and evaluate the capability to determine the response of global $PM_{2.5}$-related mortality to local changes in inorganic $PM_{2.5}$ precursor gases and primary carbonaceous emissions through use of a full (gas- and particulate-phase) adjoint model.

2.3 Methods

To calculate responses of global premature mortality to changes in $PM_{2.5}$ sources, we employed the GEOS-Chem global chemical transport model(Bey et al., 2001; Park et al., 2004) and its adjoint(Henze et al., 2007). We included information from a satellite-derived $PM_{2.5}$ climatology(van Donkelaar et al., 2010) to improve the accuracy and spatial resolution of the model exposure, as described below. We then calculated global premature mortality at the country level based on the exposure-response relationship of the GBD project as presented by Burnett et al. (2014).

2.3.1 Estimation of exposure by satellite remote sensing

Adjoint modeling requires an initial estimate from which to calculate responses. The initial ambient $PM_{2.5}$ concentrations were obtained from satellite remote sensing and modeling. Model spatial resolution has been shown to have a significant effect on predicted health outcomes; Punger and West (2013) found a 30% difference in premature mortality due to $PM_{2.5}$ exposure calculated at 200 km resolution compared with 12 km resolution. Satellite remote sensing offers global observational information about $PM_{2.5}$ through measurement of aerosol optical depth (AOD). van Donkelaar et al. (2010) produced a long-term (2001-2006) global surface $PM_{2.5}$ dataset at a resolution of $0.1^\circ \times 0.1^\circ$ ($\sim$ 10km $\times$ 10km), by combining satellite AOD measurements with knowledge of the relationship between surface $PM_{2.5}$ and AOD from GEOS-Chem simulations and found that these data well represented $PM_{2.5}$ monitors in North America ($r = 0.77$, slope= 1.07, $n = 1057$) and elsewhere in the world ($r = 0.83$, slope= 0.86, $n = 244$). These data were used, along with surface measurements and chemical transport model estimates, in the GBD project as described by Brauer et al. (2012). We similarly used this information here. Supporting Information (SI) Table

S-1 quantifies how the spatial resolution of the $PM_{2.5}$ concentrations affects exposure. We further scaled these satellite values by 1.16 to account for their overall bias versus global ground-based $PM_{2.5}$ monitors as found by van Donkelaar et al. (2010). We then turn to a chemical transport model (GEOS-Chem; www.geos-chem.org) to temporally distribute the satellite-derived $PM_{2.5}$ dataset to be consistent with the processes used in the adjoint model. The GEOS-Chem simulation solves for atmospheric transport and chemistry of 72 chemical families, including $PM_{2.5}$ precursors such as SO_2, NH_3 and NO_x, based on emissions and assimilated meteorology; a full description of the simulation is available in section S-2 and is evaluated in section S-3. Emissions are in Table S-2. We focused on the year 2005 for which mortality and satellite data were readily available.

2.3.2 Adjoint modeling to relate mortality to $PM_{2.5}$ sources

We used the adjoint of GEOS-Chem to determine the response of global $PM_{2.5}$-related mortality to changes in emissions of carbonaceous particles and inorganic precursor gases that form a large portion of ambient $PM_{2.5}$. The GEOS-Chem adjoint(Henze et al., 2007) allows for efficient computation of the partial derivatives of some scalar-valued function of the model output, the cost function, with respect to input conditions. In this work we extended the GEOS-Chem adjoint to include calculation of sensitivity of global mortality to $PM_{2.5}$ precursor emissions. We defined a cost function (SI section S-5) as the total global premature mortality based on average ambient $PM_{2.5}$ concentrations as described in section 2.3.1. Then we used the adjoint model to calculate for the entire year the field of partial derivatives of this cost function with respect to the modeled atmospheric state at each timestep in each model grid box, which we refer to as the adjoint forcing. The adjoint evolves these forcings chemically and through transport backwards in time towards emissions. The outputs provided by the adjoint, the sensitivities, are the partial derivatives of the cost function with respect to emissions in each location. In this way, it can be said that the adjoint method is a receptor-oriented approach, which calculates the regionally distributed influences on a single outcome. After computing the model sensitivities, we multiplied the field by a constant change in emissions (either $1\,\mathrm{kg\,km^{-2}\,yr^{-1}}$ or 10%), to provide the model response of global $PM_{2.5}$-related mortality to a change

(increase or decrease) in emissions. We refer to the responses in each location (a single $2^\circ \times 2.5^\circ$ GEOS-Chem grid box) as local responses to differentiate them from regional responses aggregated over multiple grid boxes.

For this study, we calculated responses to absolute changes in NH_3, SO_2 and NO_x (inorganic precursor gases), as well as primary carbonaceous aerosols of organic matter (OM) and black carbon (BC). We considered responses to relative changes in emissions of precursor gases from mainly land-based human activities and primary carbonaceous aerosols from combustion of fossil fuels, open biomass burning and biofuel burning. We focused on these sources because they comprise the dominant, readily modifiable sources that contribute to $PM_{2.5}$ exposure. These groupings also suggest specific control policies, as they tend to come from different human activities. We did not calculate responses to changes in mineral dust, secondary organic aerosol, or sea salt, which are more challenging to modify through policy. Additionally, the current adjoint model does not include secondary organic aerosol. This widely-used model is developing rapidly to represent ongoing scientific advances in the challenging area of representing $PM_{2.5}$ concentrations and formation processes. The initial results presented in this proof-of-concept study are expected to evolve with ongoing development.

2.3.3 Global mortality attributable to $PM_{2.5}$ exposure

The ambient concentrations developed in section 2.3.1 were applied to a health-impact function to calculate premature mortality for the adjoint cost function described in section 2.3.2. Following Burnett et al. (2014), we calculated the burden of disease due to $PM_{2.5}$ as the number of deaths attributable to four leading causes: ischaemic heart disease (IHD), chronic obstructive pulmonary disease (COPD), cerebro-vascular disease (CEV) and lung cancer (LC). Burnett et al. (2014) used data from studies including outdoor air pollution, household air pollution and first- and second-hand smoking to provide a concentration-response relationship for concentrations that span the entire range of observed long-term $PM_{2.5}$ concentrations throughout the world. We focused on this concentration-response curve as the most current representation of the disease-specific outcomes for the range of concentrations worldwide. The relative

risk (RR) was calculated as:

$$\mathbf{RR} = \begin{cases} 1 + \alpha \left(1 - e^{-\beta(x-x_0)^{\rho}}\right), & \text{if} x > x_0 \\ 1, & \text{otherwise} \end{cases} \tag{2.1}$$

where x is the time-averaged $PM_{2.5}$ concentration at 10 km resolution, x0 is referred to as the theoretical minimum risk exposure (TMRE), which is defined as the concentration below which it is assumed there are no health effects, and α, β, and ρ are parameters describing the shape of the exposure-response curve. For each cause we implemented the RR function as in Eq 2.1 using parameters estimated from data from the Monte Carlo simulations performed by Burnett et al. (2014). Specific parameters and graphs of the curves are in SI Section S-6. In order to examine the sensitivity of our results to our choice of health-impact function, we compared the results using the GBD health-impact function against those of two others: 1) curves fit to the GBD RR data with no TMRE

$$\mathrm{RR} = 1 + \alpha \left(1 - e^{-\beta x^{\rho}}\right) \tag{2.2}$$

and 2) assuming a log-linear response function

$$\mathrm{RR} = e^{\beta x} \tag{2.3}$$

with the same parameters as in Anenberg et al. (2010).

From these grid-level RRs, we calculated country-level population-weighted RRs, using population data from the Gridded Population of the World dataset(for International Earth Science Information Network , CIESIN). We then converted these RRs to attributable fractions (AFs) using Eq 4:

$$\mathbf{AF} = \frac{\mathrm{RR} - 1}{\mathrm{RR}} = 1 - \frac{1}{\mathrm{RR}} \tag{2.4}$$

We used country-level demographically-weighted, cause-specific mortality data, M, from the GBD Project(Lozano et al., 2012), GPW population, P, and the AF to calculate the cost function, J, global premature mortality attributable to $PM_{2.5}$ exposure:

$$J = \sum_{k}^{\text{countries}} \left(P_k \times M_k \times \mathrm{AF}_k\right) \tag{2.5}$$

We calculated adjoint forcing, the derivative of J with respect to model concentrations, at the $2^{\circ} \times 2.5^{\circ}$ GEOS-Chem resolution. Following the methods of the GBD

project, we assumed that the health effects of exposure to $PM_{2.5}$ are independent of source and composition(Lim et al., 2012). $PM_{2.5}$ mass is the most robust indicator of mortality impacts in epidemiologic cohort studies of long-term exposure(Chen et al., 2008). This assumption was followed in the GBD, is part of WHO air quality guidelines and the recent International Agency for Research on Cancer's classification of $PM_{2.5}$ as a carcinogen(Loomis et al., 2013). This assumption also implies the assumption that each of the diseases has the same component-specific sensitivity, which is likely to also be an oversimplification. Exposure is typically a mixture including both primary and secondary PM from a multitude of sources. SI S-7 presents an evaluation of the adjoint responses. Section S-8 describes our uncertainty analysis.

2.4 Results

Figure 2.1 shows the modeled marginal damages, that is, the response of global mortality to a $1\,\mathrm{kg\,km^{-2}\,yr^{-1}}$ change in emissions at $2^\circ \times 2.5^\circ$ resolution. At the level of individual grid cells, the responses ranged from -0.1 premature deaths for NO_x to +15 premature deaths for NH_3. The highest marginal damages were for NH_3 around Moscow ($15\ \mathrm{deaths\,kg^{-1}\,km^2\,yr}$). Primary carbonaceous aerosols had the strongest overall responses of the species we studied, however, marginal damages from NH_3 emissions in eastern Europe and eastern North America exceeded those from organic matter. NH_3 had the strongest response of the secondary inorganic precursors. Responses to absolute changes in organic matter were higher than to black carbon due to differences in hygroscopicity (1 kg of emitted dry OM absorbs more atmospheric water that is retained by $PM_{2.5}$ concentrations at 35% relative humidity).

Marginal damages were generally positive and varied smoothly in space. The overall spatial patterns resembled population density. This was most true for primary carbonaceous aerosols (R=0.71) and least true for ammonia (R=0.23), which had a lower response in Northern India than would be expected by following population density. Small positive marginal damages were seen in areas without population, such as over coastal oceans, due to atmospheric transport.

Negative marginal damages, that is, a net reduction in global mortality caused by an increase in emissions, were seen only for NO_x emissions and only in two areas: off the northwestern coast of New Guinea and to the southeast of Iceland, due to

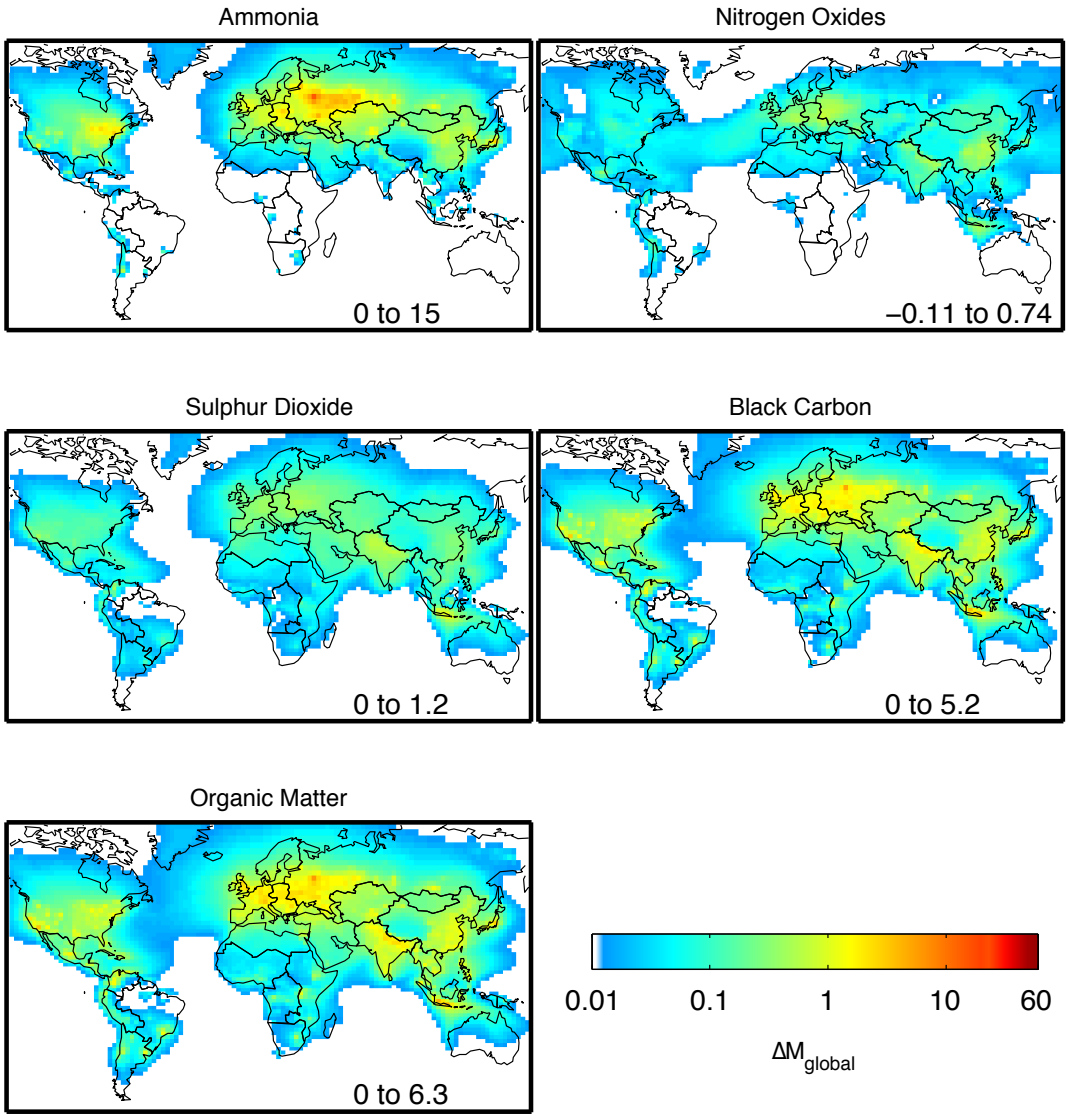

Figure 2.1: Annual response of global mortality (ΔM_{global}) attributable to a $1\,kg\,km^{-2}\,yr^{-1}$ change in local $PM_{2.5}$ precursor emissions. The color in each location indicates how increasing emissions by $1\,kg\,km^{-2}\,yr^{-1}$ in that location would change global mortality. Color scale is logarithmic. Numbers in bottom right corner represent range of sensitivities for each map. Solid lines indicate GBD region boundaries.

nonlinearities in atmospheric chemistry.

Table 2.1 and Figure S3 show marginal damages aggregated by GBD region. The highest modeled regional response to a $1\,\mathrm{kg\,km^{-2}\,yr^{-1}}$ change was for NH_3 in Eastern Europe (290 attributable deaths $\mathrm{kg^{-1}\,km^2\,yr}$). In all other regions except for Central Asia, primary organic matter had the highest modeled response of the emissions we studied. The marginal damages of BC, OM, and SO_2 emissions in South Asia were within 20% of those of East Asia. However, the modeled response of global mortality to NH_3 emissions in South Asia was an order of magnitude lower than in East Asia (6.4 vs. 56 premature deaths per kg $NH_3\,\mathrm{km^{-2}\,yr^{-1}}$).

Figure 2.2 shows the relative response, or the response in global mortality to a 10% change in emissions at $2^\circ \times 2.5^\circ$ resolution. The responses ranged from -0.5 (NO_x) to 490 (SO_2) global attributable mortalities. Responses to relative changes in emissions of the three inorganic precursors generally exceeded those for primary carbonaceous emissions.

Negative responses were small and again limited to NO_x emissions near New Guinea and Iceland.

Table 2.2 and Figure S4 show modeled responses to a 10% change in emissions aggregated by GBD region. The highest response was for SO_2 in East Asia (10,000 deaths). No single emission type dominated. East Asian emissions produced the highest response for all 5 emission types. Responses were noteworthy for Western Europe for NO_x (3,900 deaths) and South Asia for SO_2 emissions (5,600 deaths).

Table S-4 shows the rankings of the top 5 regions. Eastern Europe ranked first or second in marginal damages for all species we studied. East Asia ranked highest in all relative sensitivities.

For the health-impact function without a TMRE (Eq 2.2), the spatial pattern of the responses was nearly identical (R=0.98) to those presented here, with differences in magnitude of up to 20%.

The results obtained using a log-linear health-impact function also were spatially similar (R=0.85) to the results using the base GBD health-impact function, however responses in South and East Asia were roughly 60% stronger.

Table 2.1: Global responses to absolute changes in regional emissions. Annual global premature mortalities prevented by reducing emissions by $1\,\mathrm{kg\,km^{-2}\,yr^{-1}}$ in each of 21 GBD regions.

Region	Pop(000s)	NH_3	NO_x	SO_2	BC*	OM†
Asia Pacific, High Income	176979	13 (1.9)‡	2.0 (0.23)	3.2 (0.31)	13 (1.7)	16 (2.0)
Asia						
Central	85845	83 (7.3)	12 (0.61)	21 (1.1)	52 (3.4)	67 (4.3)
East	1347974	56 (2.2)	35 (1.6)	28 (1.0)	77 (3.2)	97 (4.0)
South	1447648	6.4 (0.41)	16 (0.84)	34 (1.7)	72 (3.7)	91 (4.7)
Southeast	579605	3.6 (0.38)	8.7 (0.49)	20 (1.3)	62 (4.5)	76 (5.4)
Australasia	24015	0.015 (0.0011)	0.47 (0.23)	5.1 (0.26)	4.1 (0.23)	5.5 (0.31)
Caribbean	33239	1.0 (0.32)	1.00 (0.13)	1.8 (0.21)	5.2 (0.67)	6.5 (0.83)
Europe						
Central	132907	36 (5.3)	10 (1.6)	11 (1.4)	39 (5.7)	49 (7.1)
Eastern	208488	290 (28)	33 (2.7)	41 (2.6)	160 (13)	200 (17)
Western	400833	60 (3.9)	13 (7.4)	27 (1.6)	90 (6.2)	110 (7.7)
Latin America						
Andean	51697	0.64 (0.087)	1.1 (0.14)	1.3 (0.15)	3.7 (0.45)	4.6 (0.55)
Central	219986	2.5 (0.27)	4.2 (0.38)	8.4 (0.88)	27 (2.9)	33 (3.5)
Southern	59838	1.9 (0.35)	1.3 (0.29)	2.1 (0.35)	6.6 (1.6)	8.2 (1.9)
Tropical	185912	0.29 (0.45)	0.49 (0.29)	3.1 (0.74)	5.5 (3.3)	6.9 (4.0)
North Africa /Middle East	395799	23 (1.0)	10 (0.39)	32 (0.96)	41 (1.6)	54 (2.0)
North America, High Income	326001	95 (4.7)	18 (0.88)	32 (1.4)	87 (5.2)	110 (6.4)
Oceania	5885	0.087 (0.057)	0.070 (0.065)	0.18 (0.049)	0.50 (0.18)	0.62 (0.21)
Sub-Saharan Africa						
Central	86332	0.28 (0.043)	0.12 (0.015)	2.0 (0.14)	3.6 (0.31)	4.5 (0.38)
Eastern	306682	0.52 (0.041)	0.58 (0.039)	6.5 (0.30)	11 (0.85)	13 (1.0)
Southern	65633	0.66 (0.15)	0.12 (0.024)	1.2 (0.12)	2.1 (0.35)	2.7 (0.43)
Western	281349	0.97 (0.14)	1.6 (0.12)	5.2 (0.34)	5.3 (0.52)	6.9 (0.65)
Total	6422647	680 (31)	170 (8.3)	290 (4.8)	760 (19)	960 (24)

* BC represents primary black carbon aerosols from fossil fuel, biomass, and biofuel combustion.
† OM represents primary organic matter aerosols from fossil fuel, biomass, and biofuel combustion.
‡ Numbers in brackets represent ±1 error standard deviation.

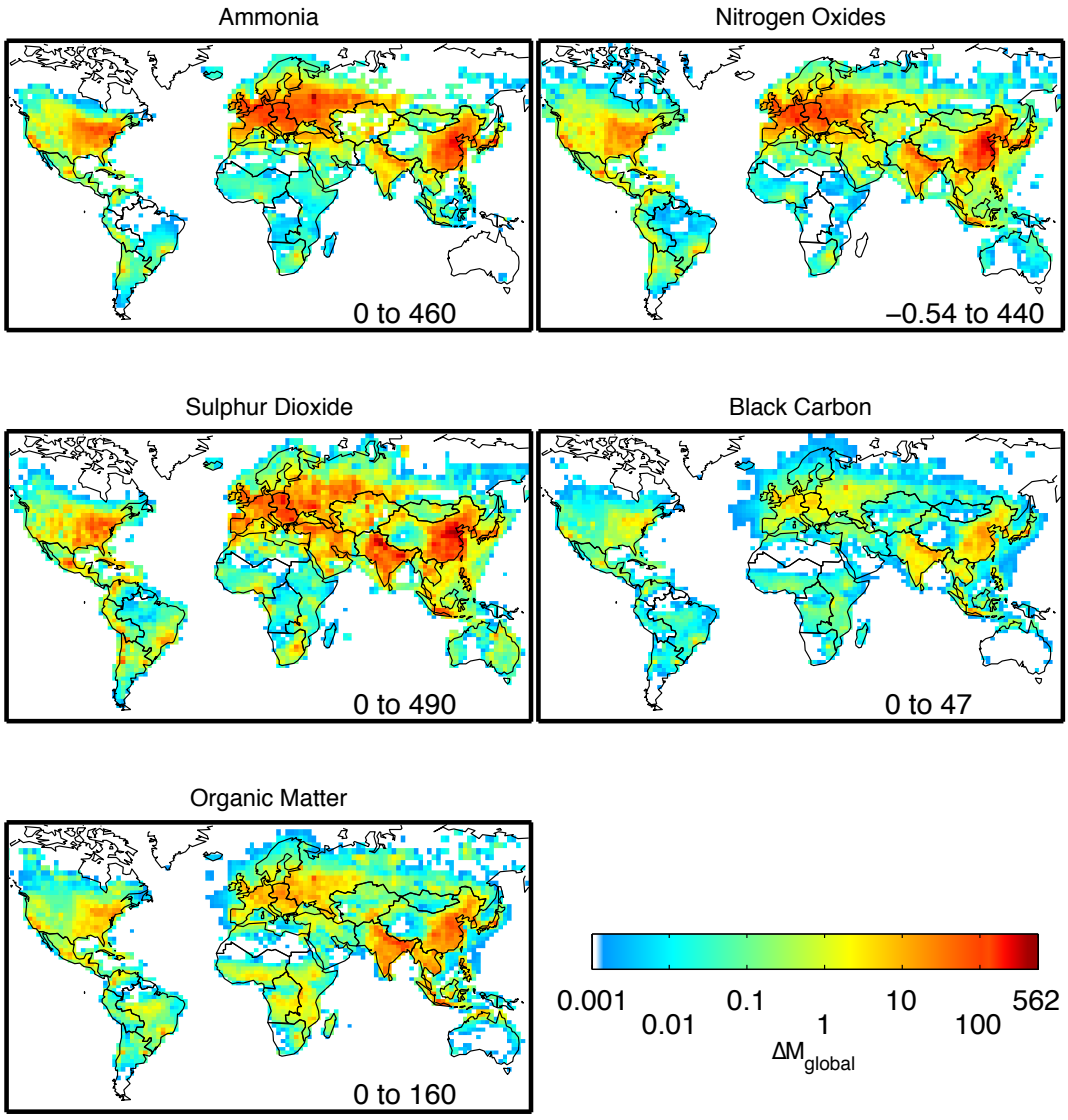

Figure 2.2: Annual response of global mortality (ΔM_{global}) attributable to a 10% change in local $PM_{2.5}$ precursor emissions. The color in each location indicates how increasing emissions by 10% in that location would change global mortality. Color scale is logarithmic. Numbers in bottom right corner represent range of sensitivities for each map. Solid lines indicate GBD region boundaries.

Table 2.2: Global responses to relative changes in regional emissions. Annual global premature mortalities prevented by reducing emissions by 10% in each of 21 GBD regions.

Region	Pop(000s)	NH_3	NO_x	SO_2	BC[a]	OM[b]
Asia Pacific, High Income	176979	730 (150)[c]	730 (140)	500 (69)	120 (26)	240 (51)
Asia						
Central	85845	400 (57)	180 (24)	860 (97)	16 (1.7)	160 (18)
East	1347974	5800 (440)	8000 (670)	10000 (730)	550 (41)	2300 (170)
South	1447648	500 (42)	1600 (130)	5600 (460)	330 (25)	2000 (160)
Southeast	579605	89 (8.4)	430 (36)	1100 (120)	170 (19)	1100 (110)
Australasia	24015	0.066 (0.010)	2.1 (0.24)	74 (11)	3.3 (0.49)	57 (8.7)
Caribbean	33239	8.2 (1.9)	34 (5.1)	99 (15)	2.5 (0.34)	15 (2.1)
Europe						
Central	132907	2400 (380)	2100 (340)	2800 (420)	72 (13)	350 (61)
Eastern	208488	5400 (740)	2600 (370)	3200 (420)	100 (25)	670 (140)
Western	400833	4000 (360)	3900 (460)	2200 (200)	150 (16)	360 (38)
Latin America						
Andean	51697	9.4 (1.5)	18 (2.3)	110 (27)	2.0 (0.39)	17 (3.8)
Central	219986	84 (17)	290 (61)	470 (90)	25 (4.2)	140 (22)
Southern	59838	29 (6.6)	37 (11)	200 (49)	6.8 (5.3)	28 (17)
Tropical	185912	14 (26)	38 (52)	140 (100)	11 (15)	85 (70)
North Africa /Middle East	395799	310 (22)	270 (16)	1900 (100)	18 (1.4)	74 (4.8)
North America, High Income	326001	2600 (170)	1800 (120)	2100 (140)	150 (16)	620 (49)
Oceania	5885	0.50 (0.62)	0.063 (0.14)	0.14 (0.062)	0.018 (0.0062)	0.14 (0.047)
Sub-Saharan Africa						
Central	86332	0.96 (0.18)	0.70 (0.16)	22 (5.3)	5.6 (0.58)	90 (8.3)
Eastern	306682	6.1 (0.59)	1.5 (0.19)	40 (6.8)	13 (1.6)	160 (16)
Southern	65633	13 (3.7)	10 (6.2)	96 (27)	2.4 (0.75)	19 (5.0)
Western	281349	12 (5.9)	8.1 (2.8)	48 (19)	5.1 (1.0)	70 (13)
Total	6422647	22000 (1000)	22000 (990)	32000 (1100)	1800 (71)	8500 (320)

[a] BC represents primary black carbon aerosols from fossil fuel, biomass, and biofuel combustion.
[b] OM represents primary organic matter aerosols from fossil fuel, biomass, and biofuel combustion.
[c] Numbers in brackets represent ±1 error standard deviation.

2.5 Discussion

This study examined the response of global $PM_{2.5}$-related mortality to changes in precursor emissions. The responses presented here are based on current scientific understanding of the factors affecting global $PM_{2.5}$ concentrations, combined with current scientific understanding of $PM_{2.5}$-related mortality. The exposure distribution, exposure-response functions, and mortality distribution used in this study build from the substantial effort undertaken as part of the GBD project. The responses generated using this novel method can therefore highlight some important geographical patterns, such as the large global benefits from reducing South Asian SO_2 emissions instead of NH_3 emissions. We presented responses to both absolute and relative changes in emissions. Responses to absolute changes (i.e., marginal damages) are more easily interpreted since they are less dependent on the initial emission rates. Responses to relative changes are of more relevance for some policy applications such as reducing vehicle-miles traveled.

In general, the response of global mortality to changes in precursor emissions was proportional to population distribution. Responses were enhanced by high relevant baseline mortality rates in Eastern Europe, East Asia, and Indonesia. The relationship of population with relative responses was stronger than with marginal damages because emissions tend to be correlated with population. Precursor emissions near dense populations have the largest opportunity to affect exposure. Long-range transport also can be important and has been extensively studied(on Hemispheric Transport of Air Pollution, 2010). Some indication of the distances over which transport affects exposure can be seen in Figure 2.1, where responses > 0.01 death $\mathrm{kg}^{-1}\,\mathrm{km}^2\,\mathrm{yr}$ can be seen over the ocean hundreds of kilometers from populated shorelines.

Striking regional differences were found in responses. Global mortality was 2-10 times less sensitive to relative changes in emissions from South Asia than from East Asia, in part because emissions and relevant baseline mortality rates in the South Asia region tend to be lower. Eastern Europe ranked first in marginal damages to all emissions studied except SO_2, in part due to high regional relevant baseline mortality rates for the diseases related to air pollution. Furthermore, the baseline $PM_{2.5}$ concentrations in Eastern Europe make the RR highly sensitive (4–10 times more sensitive than Eastern China or Northern India) to changes in $PM_{2.5}$ concentrations

because the slope of the RR curve decreases with increasing $PM_{2.5}$ concentrations (SI Figure S-2). Primary carbonaceous aerosols had the strongest overall marginal damages because carbonaceous material is emitted as particulate matter, whereas with secondary inorganics, only in limiting cases will precursor gases undergo 100% conversion to the aerosol phase. Fann et al. (2009) similarly found large marginal damages from carbonaceous emissions compared with emissions from secondary inorganic precursors.

NH_3 marginal impact was both the strongest response of the secondary inorganic precursors and the least related to population. Formation of $PM_{2.5}$ as $(NH_4)_2SO_4$, NH_4HSO_4, or NH_4NO_3 yields more mass formed than emitted. Low responses in northern India arise from a large reservoir of NH_3 that has already reacted with the available SO_4^{2-} and NO^{3-}. Our results are consistent with a recent European Topic Centre review that found overall, NH_3 was likely to be the most important $PM_{2.5}$ precursor species for continental Europe and especially the United Kingdom (Beauchamp et al., 2013). Nonetheless, our NH_3 responses may be greater than actual responses in maritime-influenced regions such as the Mediterranean, because the Na^+-NO^{3-} reaction (Athanasopoulou et al.) is not included in the aerosol thermodynamics in the model version we used. Our NH_3 sensitivities in Europe were 0.4 to 0.8 of the original values for the month of January when we decreased NO_x emissions by 50% to simulate losing NO_3^- to $NaNO_3$.

Our finite difference tests (section S-7) indicated that conclusions drawn from these responses were as good as those calculated by perturbing emissions to the forward model for a range of changes in emissions up to at least 10% from current rates. Moreover, these local sensitivities for several species were calculated using approximately three times the computing resources of a single forward model run. Computing local sensitivities by the finite-difference method of perturbing emissions would require tens of thousands of forward model runs.

The dominant sources of uncertainty in the simulation responses arose from representation of $PM_{2.5}$-formation processes and from uncertainty in health-impact function parameters (section S-8). The quality of the results from this method will continue to improve as results from region-specific $PM_{2.5}$ mortality cohort studies become available, and as higher-resolution simulations better capture the relation between

$PM_{2.5}$ and emissions(Cohan and Napelenok, 2011).

It is possible that the model has missed not only the magnitude, but also the sign of the true sensitivity, as a result of nonlinearities in the $PM_{2.5}$ formation process and differences between the true state of the atmosphere and the modeled state caused, for example, by processes not included in the model. In the future, the very tool we used in this study, the adjoint, could be used to assimilate observations, improving the accuracy of emission inventories and model parameters so that the modeled state better represents the true state (Xu et al., 2013).

The exposure response function produced by Burnett et al. (2014) included a TMRE. In order to represent this, our fit parameters included a TMRE ranging from 7.0 for IHD to 8.4 for stroke. Epidemiological research to date has not found an exposure threshold where $PM_{2.5}$ reductions provided no benefit (Correia et al., 2013; Crouse et al., 2012). For example, a recent population-based study in Canada observed no deviation from linearity in the relationship between concentrations and mortality even at concentrations as low as 5 µg m^{-3}, which is approaching the lowest measured concentrations in populated areas (Crouse et al., 2012). Eliminating the TMRE linearly changed our results (R=0.98), indicating that the spatial relationships we found are robust.

Like the GBD project, this study assumed that the health effects of exposure to $PM_{2.5}$ are independent of source or composition. While this may not be true, the current evidence is insufficient to determine composition-dependent exposure-response curves. The role of chemical composition as a determinant of toxicity attributable to ambient particulate matter is an active research area (Heal et al., 2012; Kelly and Fussell, 2012). Future changes to exposure-response functions, which incorporate information about $PM_{2.5}$ composition, could be readily incorporated into the framework presented here, for example by applying component-specific concentration-response functions. Other metrics such as disability-adjusted life years or monetary health benefits could also readily be implemented.

We calculated these sensitivities based on population distributions, demographics, and relevant baseline mortality rates from the year 2005, and for that reason our estimates pertain to the burden of disease attributable to exposure to $PM_{2.5}$ in 2005 and should not be assumed to reflect the burden that might be avoided in the future

(Murray et al., 2004). Changes to the burden of disease due to exposure to $PM_{2.5}$ that might be expected to occur in the future as a result of changes in the relative contribution of various pollution sources would depend importantly on future cause-specific mortality rates for cardiovascular and respiratory diseases, and lung cancer. These rates changed dramatically between 1990 and 2010 and would be expected to change further in the future due to changes in population age distributions and other factors (Lozano et al., 2012; Mathers and Loncar, 2006). Increasing urbanization is also likely to change exposure to particulate matter (Grimm et al., 2008). Therefore, it is advisable to periodically update this analysis to reflect current demographics and exposure in future.

In this study, changes in global mortality were not attributed to a particular area. These results are, therefore, most relevant to global policy. In order to determine how mortality in a specific area is affected by changes in another (or the same) specific area, the adjoint would need to be run with the cost function defined for the area of interest. This is planned for future study of country-specific mortality.

In summary, we used the adjoint of the GEOS-Chem chemical transport model to efficiently determine the response of global mortality to changes in local emissions. We found that global mortality exhibited dramatic differences in sensitivity to emissions from different regions or different emission types. Overall, global mortality was more sensitive to absolute changes in emissions of primary carbonaceous aerosols than of secondary inorganic precursors. The highest responses for relative changes were found in secondary inorganic precursor emissions from China and in SO_2 emissions from India. These responses imply regionally dependent policies, even when the regions have similar populations. For example, controls on agricultural emissions of NH_3 in East Asia could prevent 10 times more premature deaths than would these same controls in South Asia. Our results also suggest that the benefits of China's recent controls on SO_2 emissions may be partially offset by rising NO_x and NH_3 emissions.

Chapter 3

Insights into simulated global aerosol distribution and processes from assimilation of space-based lidar profiles

3.1 Abstract

Atmospheric aerosols are frequently subject to long range transport > 1000 km. To study the pathways from sources to endpoints, it is important to properly characterise the global 3-dimensional distributions of aerosols. While other studies have used the space-borne lidar CALIOP as a validation tool or for local assimilations, we assimilated CALIOP aerosol extinction profiles for the entire globe for January and June of 2007, although there is no reason that the framework we present cannot be extended in time. Using the adjoint of GEOS-Chem, we assimilated CALIOP lidar profiles at 532 nm. In order to test the importance of emissions versus initial model conditions, we performed two separate assimilations, one optimising the models initial state (initial conditions; ICs) with a 24-hour assimilation window, and another optimising primary aerosol emissions (EMs) with a 31-day assimilation window. Because of the influence of ocean emissions on this study, we also implemented the adjoint of sea-salt chemistry and emissions, which was previously unimplemented.

Following the methods of the AEROCOM study, we compared mean extinction height (Z_α) between our baseline simulation and the two optimised simulations to CALIOP observed Z_α and found that both optimisations improved the slope and offset of a linear fit across AEROCOM regions, but ICs improved agreement (R = 0.78) compared to the baseline (R = 0.72) while EMs decreased agreement (R = 0.65).

In a global comparison of AOD, the optimised emissions greatly improved agreement with observations in the Sahara in January, but failed to capture the overall underestimate of AOD seen almost everywhere. The IC optimisation greatly improved AOD globally but showed only modest improvement over the Sahara. These

same situations are borne out by examining the profiles; optimised emissions reproduced observed profiles in the Sahara in January well, but this decreased model agreement over the mid-Atlantic ocean downwind. Conversely, the optimised ICs did only slightly better than the baseline model in the Sahara, but did not decrease agreement downwind. These results indicate a bias in Saharan dust emissions, but also a possible transport issue in the model; at present it appears to be impossible to decrease aerosol loading over the Sahara to improve agreement with observations without also decreasing loading downwind over the Atlantic, worsening agreement with observations.

3.2 Introduction

The 3-dimensional global distribution of aerosols has wide-ranging impacts on climate and air quality processes. Aerosols have positive and negative climate forcing implications in the short and long terms, (e.g., Boucher et al., 2013a). Some classes of aerosols, especially fine particulate matter with an aerodynamic size less than 2.5 µm ($PM_{2.5}$) are an important contributor to global premature mortality and morbidity (e.g., Cohen et al., 2015). Sources of $PM_{2.5}$ are complex and the impacts of aerosols are often felt far away from the sources, making it important to properly characterise the transformation and transportation of aerosol through its lifetime. Understanding and predicting the 3D distribution of aerosols is also important for the interpretation of columnar satellite observations (van Donkelaar et al., 2010). Global in situ monitoring of $PM_{2.5}$ concentrations, while improving, remains sparse in many regions, and only provides a view of surface concentrations. Interpretation of satellite measurements of the aerosol vertical profile could yield valuable information about processes affecting the global 3D aerosol distribution.

GEOS-Chem is a global chemical transport model (CTM) based on assimilated meteorology from either the GEOS-FP or MERRA-2 reanalyses (Bey et al., 2001). Transport is performed by the TPCORE algorithm (Lin and Rood, 1996). The model includes 72-chemical tracers including primary carbonaceous, dust and sea-salt aerosols, and secondary inorganic aerosol precursor gases, sulphate, nitrate and ammonia. The model runs globally at $4^\circ \times 5^\circ$ or $2^\circ \times 2.5^\circ$ resolution, with nested grids at higher spatial resolutions available at many locations. Global emissions are

provided by a number of inventories but are overwritten by regional inventories where available.

The GEOS-Chem adjoint is a complimentary set of equations to the forward GEOS-Chem CTM. The adjoint model allows for the computation of sensitivities of a scalar-valued cost function with respect to model boundary conditions, i.e., tracer concentrations at timestep 0, or emissions. 4DVAR data assimilation is a technique for combining numerical modelling with observational data which allows for sparse information to be spread through space and time by using a model adjoint (Wang et al., 2001). The technique is an iterative algorithm that uses the adjoint sensitivities to find model inputs which produce the simulation output that best matches a set of observations, given the uncertainties in the observations and model output.

The Cloud-Aerosol LIdar with Orthogonal Polarization (CALIOP) instrument is a space-borne lidar aboard the Cloud-Aerosol Lidar and Infrared Pathfinder (CALIPSO) satellite, launched in 2006 (Winker et al., 2009). CALIOP measurements of backscattered laser pulses offer height-resolved information about aerosol concentrations during both the day and night. CALIOP is also able to see through optically thin features which may otherwise confound passive measurements. CALIOP profiles have been used to validate other satellite retrievals, (e.g., Gautam et al., 2013; Clarisse et al., 2014), evaluate models, (e.g., Liu et al., 2011; Geng et al., 2015), and track plumes aloft, (e.g., Yumimoto et al., 2009; Ford and Heald, 2012); to measure backscatter from particles and phytoplankton suspended in the top layer of the ocean (Behrenfeld et al., 2013); and to improve other satellite aerosol products, for example, in cloud detection and filtering (Toth et al., 2013).

CALIOP and ground-based lidar data have been used in data assimilation previously. Yumimoto et al. (2007) assimilated a ground-based lidar network in Japan to provide improved estimates of Asian desert dust emissions. Sekiyama et al. (2009, 2011) used an 4DVAR enKF method to also retrieve Asian desert dust emissions during different seasons and meteorological conditions. Zhang et al. (2014) used CALIOP in a suite of satellite measurements to improve global distribution of aerosols in the NAAPS transport model, but CALIOP data was used only to provide a relative vertical distribution. Lynch et al. (2016) used NAAPS to assimilate MODIS AOD for an operational aerosol forecast. Both of these studies used the NAAPS model, which

does not include chemistry such as SIA formation (Witek et al., 2007). Details of operational assimilation schemes from NASA's Global Modelling and Assimilation Office (GMAO) and the European Centre for Medium-Range Weather Forecasts (ECMWF) are difficult to find, but it does not appear that CALIPSO/CALIOP profiles are currently being assimilated into any operational product.

Previous global data assimilation studies of CALIOP lidar profiles have focused on using aerosol transport models to constrain emissions of mineral dust. The adjoint of GEOS-Chem allows for not only transport of dust, but for the assimilation to account for chemically active species (Henze et al., 2007). In addition to emissions inputs, simulations also rely on an initial state, which can be adjusted to reproduce observations. Because CALIOP profiles provide data about the vertical as well as the horizontal distribution, valuable insight can be gained by examining how the assimilation optimises not only the emissions, which typically come from the Earth's surface, but also the 3D initial state from which the model state evolves over time. At the time of writing, the adjoint of GEOS-Chem is not capable of optimising both these sets of input parameters simultaneously, although that feature is under development. Similar dual parameter optimisations have been performed with a high-resolution nested simulation to optimise both emissions in the high resolution domain and the low-resolution boundary conditions used as input (Wecht et al., 2014; Jiang et al., 2015), however these studies were with gases, not aerosols, and optimised only the 3-dimensional model state in a lateral ring around the nested domain. Both studies mentioned difficulties in setting the optimisation scheme meta-parameters to balance the contributions of emissions and boundary conditions, an issue which is likely to be exacerbated by trying to optimise not only a small 3-D area but the whole global grid simultaneously with emissions. Therefore, it is important to understand how vertical and horizontal information contributes separately to these two sets of input parameters.

Another advantage of CALIOP profiles is the ability to penetrate optically thin clouds, to gain a unique view of areas invisible to passive remote sensing. Grythe et al. (2014) showed that the parts of the ocean which are least well measured by in situ monitoring are also areas which are often cloud covered. That study also showed a -45% bias versus a global sea-salt observation data set when using the sea-salt

production scheme described by Jaeglé et al. (2011), which is the same scheme used in GEOS-Chem. In general, global sea-salt is poorly constrained with global annual emissions from commonly used source functions ranging 3 orders of magnitude from 1.83 to 2,444 Pg/yr (Grythe et al., 2014, Table 2).

In this study, I present a proof-of-concept 4DVAR data assimilation of CALIOP L2 extinction profiles at 532 nm. Because it is difficult to find independent height-resolved measurements of aerosol extinction, I validate the method by comparing the model results after assimilation to other CALIOP profiles not used in the assimilation. I used the assimilation framework to separately optimise model initial conditions or emissions. To perform these tasks, I implemented a module for the adjoint of GEOS-Chem to read in CALIOP Level-2 (L2) aerosol extinction profiles at 532nm. Prior to this study, chemistry, emissions and deposition was available in the adjoint for the aerosol and precursor species we used, except for sea-salt aerosol (SSA); only the transport of SSA was implemented in the GEOS-Chem adjoint. In this study, I added adjoint code for emissions, (wet and dry) deposition, and chemistry of SSA. By expanding the use of the CALIOP profile data beyond inert tracers, we are able to more fully represent the complex state of global atmospheric aerosols. Additionally, because of the vertical information available in CALIOP profiles, we are able to compare the optimisation of emissions to the optimisation of initial conditions to help inform future endeavours to optimise both sets of parameters simultaneously. To our knowledge this is the first study to use CALIOP lidar profiles in this way.

3.3 Methods

In this study, we used the chemical transport model GEOS-Chem and its adjoint to assimilate level-2 (L2) extinction profiles at 532 nm. In section 3.3.1 we describe the CALIOP L2 profiles and our data filtering. To achieve the processing we describe with the adjoint of GEOS-Chem, we added an observational operator module that reads the NASA data files directly into the adjoint. In section 3.3.2 we describe our process for assimilating the profile data.

3.3.1 CALIOP Lidar Profiles

CALIPSO is part of the A-train of satellites which fly in a sun-synchronous orbit with an equator crossing time of approximately 1330 local time (Winker et al., 2009). The CALIOP level-1 (L1) retrievals report the range-resolved total attenuated backscatter at 532nm and 1064nm, and the perpendicularly polarized attenuated backscatter at 532nm. The L2 retrievals include a number of derived profile and layer products, such as type and extinction for clouds, aerosols and polar stratospheric clouds. Aerosol extinction profiles are calculated by fitting the measured backscatter to the two-way transmission of light, which requires an extinction-to-backscatter coefficient, S_p (Young and Vaughan, 2009). The Quality Control (QC) flag indicates whether the retrieval was able to infer S_p from clean air regions above and below the layer or used an assumed lidar ratio. The Cloud-Aerosol Discrimination (CAD) score indicates how strongly the retrieved properties of the layer indicate aerosol or cloud type. CALIOP is more sensitive to noise from background radiation than ground-based lidar due to the power constraints of being aboard a satellite; this is especially important during the day leg of the orbit. Other sources of uncertainty in the measurements include the inferred or assumed lidar ratio, the assumed molecular profile, and the calibration coefficient. These values are all accounted for in the reported L2 extinction uncertainty.

In the more than 1 decade since its launch, CALIOP AOD retrievals have been compared with other satellite products, (e.g., Chen et al., 2010; Kittaka et al., 2011), and validated against AERONET measurements (e.g., Mielonen et al., 2009; Omar et al., 2013). CALIOP backscatter profiles have been validated against ground-based lidar measurements, (e.g., Kim et al., 2008; Mamouri et al., 2009; Balmes et al., 2019), and airborne lidar measurements, (e.g., Rogers et al., 2011; Kacenelenbogen et al., 2014). Previous research has shown that the CALIOP feature detection algorithm tends to miss optically thin features beneath other features (Omar et al., 2013; Pan et al., 2015; Kim et al., 2017), resulting in "clean air" values being reported erroneously. Because of this, to avoid creating a low bias in our assimilation, we ignored "clean air" values below other features. Aerosol features below other features

were assumed to be accurate. In addition, CALIOP often requires an extinction-to-backscatter ratio, S_p, to complete extinction retrievals, which results in the application of a ratio for an assumed aerosol type (Young and Vaughan, 2009). These assumed lidar ratios have been found to slightly underestimate S_p in clean cases, especially in the case of changing surface geography (Kacenelenbogen et al., 2011; Kanitz et al., 2014), while in more polluted air masses, S_p has been shown to be both over- and under-estimated (Burton et al., 2013; Rogers et al., 2014), although recently it has been shown that some of these biases may be the result of treatment of below-detection-limit values rather than incorrect S_P assumptions (Toth et al., 2018).

CALIOP extinction detection limits vary with altitude from 0.020 km^{-1} at the surface to 0.0030 km^{-1} in the lower-to-mid stratosphere (Winker et al., 2009). The correct treatment of below-detection-limit (BDL) values is a matter of some debate (Ford and Heald, 2013; van Donkelaar et al., 2013; Toth et al., 2018). On the one hand, BDL values are imprecise, and may therefore be inappropriate for inclusion in a data assimilation. On the other hand, the presence of a BDL observation can be valuable information in the case where the model extinction is above the detection limit. For this proof-of-concept, we replaced BDL observations with the value of the detection limit (DL) for that altitude and gave them an error of $\sqrt{10}\times$DL. This allows the assimilation to include BDL observations without putting excessive weight on the exact values of those observations. It is difficult to evaluate the validity of this choice without independent observations for comparison.

CALIOP extinction values at 532nm were taken from the L2 5km aerosol profile product, version 3.01. Although version 4.10 has been released with changes to the calibration procedures (Getzewich et al., 2016), as most of the changes to calibration constants were on the order of a few percent, we do not expect the new data to change any of the conclusions of this study. Measurements were filtered based on the QC flag field, allowing only constrained and unconstrained retrievals, and a CAD score between -100 and -20 (Ford and Heald, 2013; van Donkelaar et al., 2013). In order to make the observations comparable to the model, for each model timestep, we aggregated the CALIOP observations during that interval into $4^\circ \times 5^\circ \times h$ (where h is the location-dependent GEOS-Chem grid box height) superobservations. Since each superobservation may be composed of multiple CALIOP observations, we only

included superobservations where at least $\frac{2}{3}$ of CALIOP observations falling within a given superobservation box met our quality screening criteria described above.

3.3.2 Data Assimilation Scheme

The adjoint of GEOS-Chem was developed in Henze et al. (2007). It has been used for sensitivity studies and data assimilation studies focusing on black carbon and other aerosol species (e.g. Xu et al., 2013; Zhang et al., 2015a; Lee et al., 2015; Xu et al., 2017; Lacey et al., 2017).

Our starting point for this study was version 35f of the GEOS-Chem adjoint, to which we added an observational operator module to perform a 4DVAR assimilation of L2 CALIOP lidar aerosol profiles. GEOS-Chem is driven by assimilated meteorology as produced by the NASA Global Modelling and Assimilation Office (GMAO). In this study we used the GEOS-5 meteorology at $4^\circ \times 5^\circ$ with 47 vertical levels. The model includes primary and secondary sulphate-nitrate-ammonia (Park et al., 2004), carbonaceous aerosols (Park et al., 2003), mineral dust (Fairlie et al., 2007), and sea-salt (Jaeglé et al., 2011). Chemistry for 116 chemical species and 43 tracer families is performed with the KPP solver (Damian et al., 2002). Heterogeneous chemistry is described by Jacob (2000) with updates(Evans, 2005; Mao et al., 2013). Relative humidity(RH)-dependent optical properties used in calculating simulated extinction and optical depth are described in Martin et al. (2003). Dust optical properties are described by (Ridley et al., 2012). In order to complete the simulations used in this study, we implemented the previously undeveloped sea-salt aerosol adjoint which allows for the tracking of emissions, chemistry, and wet- and dry-deposition of course and accumulation mode sea-salt aerosols.

4DVAR data assimilation uses spatial and temporal information from observations to find the model inputs which minimize a scalar cost function on the model output. The assimilation first computes the model state, then a scalar function of that output state, the cost function J. The gradient of that scalar cost function with respect to the model output state (the forcing) is used as input to the model adjoint. The adjoint transforms the forcing fields through the model equations into the gradient of J with respect to model input conditions, such as emissions, or initial model state. A gradient descent algorithm can then adjust all the selected input parameters simultaneously to

change the model output state in a way that decreases J. By iterating over these steps, the model output state will more accurately represent the state of the atmosphere combining the best knowledge from the model equations and the observations.

For our 4DVAR data assimilation of CALIOP L2 aerosol profiles, we define J as follows:

$$J = \frac{1}{2}\sum_{\Omega}\left(\mathbf{X}-\mathbf{X}_{\mathrm{CAL}}\right)^{\mathrm{T}}\mathbf{S}_{\mathrm{CAL}}^{-1}\left(\mathbf{X}-\mathbf{X}_{\mathrm{CAL}}\right)+\frac{1}{2}\gamma_r\left(\mathbf{p}-\mathbf{p}_a\right)^{\mathrm{T}}\mathbf{S}_p^{-1}\left(\mathbf{p}-\mathbf{p}_a\right) \quad (3.1)$$

where $\mathbf{X}$ is the vector of GEOS-Chem extinction coefficients in km^{-1}, $\mathbf{X}_{\mathrm{CAL}}$ is the vector of CALIOP retrieved extinction coefficients averaged onto the GEOS-Chem 4°x5° horizontal grid and 47 vertical levels, $\mathbf{S}_{\mathrm{CAL}}$ is the error covariance matrix of CALIOP extinction coefficients, $\mathbf{p}$ is a vector of initial aerosol mass, $\mathbf{p}_a$ is the vector of the original estimates of aerosol mass, $\mathbf{S}_p$ is the error covariance matrix of these initial concentrations, γ_r is a regularization parameter, and Ω is the domain in time and space over which observations are assimilated into the model. This cost function was implemented as a new module to the GEOS-Chem adjoint which directly ingests CALIOP L2 aerosol profile data files into the model, computing the superobservation and gridded uncertainty data online.

The adjoint model calculates the gradient of this cost function with respect to initial concentrations (ICs) or emissions (at present, not both simultaneously), ∇J_p, which is then used in an iterative solution, the L-BFGS algorithm(Morales and Nocedal, 2011), to find the initial conditions or emissions that minimize J. In practice, we ran between 20 and 60 iterations instead of to convergence, because of limits on computational resources. The cost function was still typically decreasing by around 1% per iteration by iteration 40 (compared to 5-10% for the first 10 iterations), indicating the results we present here are similar to what would be obtained if we allowed the process to run to convergence every time.

In our optimisation scheme, we set the regularization parameter to 0.01; our results are not strongly sensitive to this parameter. Results from using a regularization parameter of 10 had a correlation R > .95 with the 0.01 results, but the cost function decreased approximately 20% less per L-BFGS iteration. We set the diagonal elements of $\mathbf{S}_p$, the error variances, to the larger of 100% of the local value or the 10th percentile of that tracer's global concentration distribution. The off-diagonal elements were set

to zero, that is, errors were treated as uncorrelated in time, space and across species. The observation error variances were computed by root-mean-squaring the errors from the CALIOP L2 profiles used in each $4^\circ \times 5^\circ \times h$ box, i.e., if n observations with σ reported uncertainty were averaged together in a grid box, the error for that grid box would be $\frac{1}{\sqrt{n}}\sigma$. Once again, off-diagonal elements were set to zero.

In any data assimilation there are many free meta-parameters to choose. It would be impossible to study the sensitivity of these results to every single one. I have chosen the parameters that seem realistic in terms of allowing for the work to be computed in less than real time and trying to extract meaningful data from the observations.

In order to demonstrate the different information gleaned by our system we performed assimilation runs for January and July of 2007. Because the adjoint of GEOS-Chem does not currently provide capability to optimise both emissions and ICs at the same time, we did two separate types of optimisation. To demonstrate how CALIOP profiles affect emissions, we did 1-month emissions optimisations for January and July. In order to demonstrate the effects of CALIOP profiles on the initial state of aerosol tracers, we did consecutive 24-hour assimilations to optimise ICs. That is, we simulated from 0:00 on day 1 to 0:00 on day 2, then used the model state at the final timestep of day 1 as the new initial conditions to simulate day 2. For the model baseline condition, we simply ran each day once. For the optimised ICs condition, we ran the assimilation for day 1, then used the optimised output of day 1 to initialize day 2, making the first run of of day 2 a forecast. We then optimised day 2, and used this output to initialize day 3, and so on. By using only the forecast output in our analysis, we can avoid directly comparing with the data used in the assimilation.

3.3.3 Assessment of Assimilation Performance

Ultimately the goal of any assimilation is to improve the model's representation of the true tracer concentrations. However, CALIOP is the only available source of global 3D measurements of aerosol, making it difficult to ascertain the true state in many places where the assimilation was done. To assess the assimilation results, we compared the vertical distribution of aerosol in the various simulations, and the observations we used in the assimilation using the mean extinction height Z_α, as in Koffi et al. (2012, 2016). Mean extinction height provides a single number which

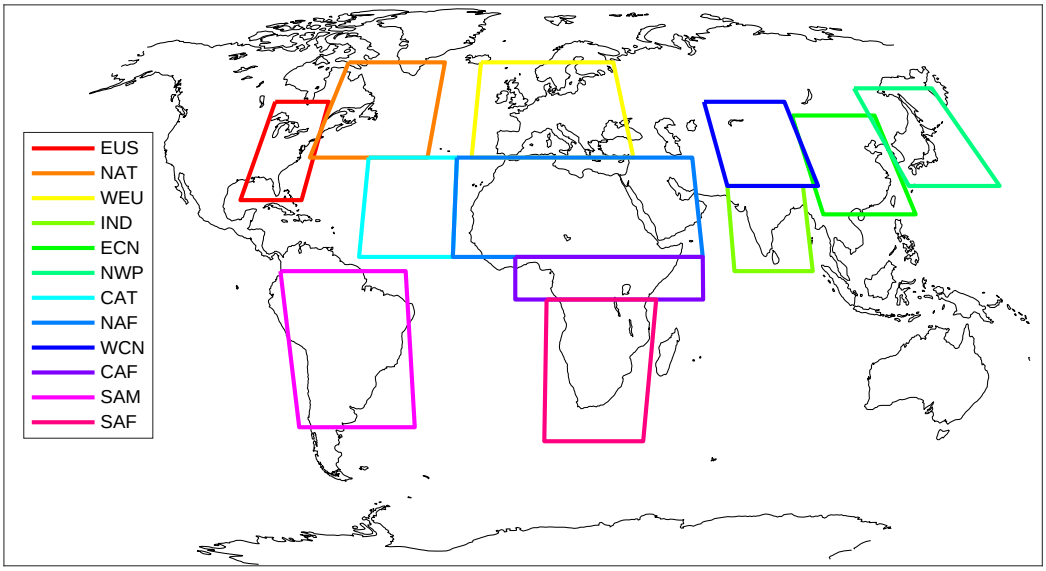

Figure 3.1: The regions used to compare mean extinction height, designed to capture different global environments and source profiles, modeled after Koffi et al. (2012, 2016).

indicates roughly at what altitude most of the extinction is located, and is calculated as:

$$Z_\alpha = \frac{\sum_{h=\text{surf}}^{6\text{km}} b_{\text{ext}} \cdot h}{\sum_{h=\text{surf}}^{6\text{km}} b_{\text{ext}}} \tag{3.2}$$

Although this metric is limited, it does provide a fast comparison between groups of columns. As in Koffi et al. (2012, 2016), we limited mean extinction height to below 6 km to avoid comparisons including the high troposphere, where CALIOP is known to have low sensitivity when aerosol concentrations are low (Winker et al., 2009, 2013). In order to examine our results in different global environments with different source profiles, while staying within the context of the current literature, we used roughly the same regions as Koffi et al. (2012, 2016), which we show in Figure 3.1. We chose to aggregate the columns because of the spatial mismatch between the roughly 75m-wide CALIOP profiles and the GEOS-Chem grid boxes which are hundreds of km on a side.

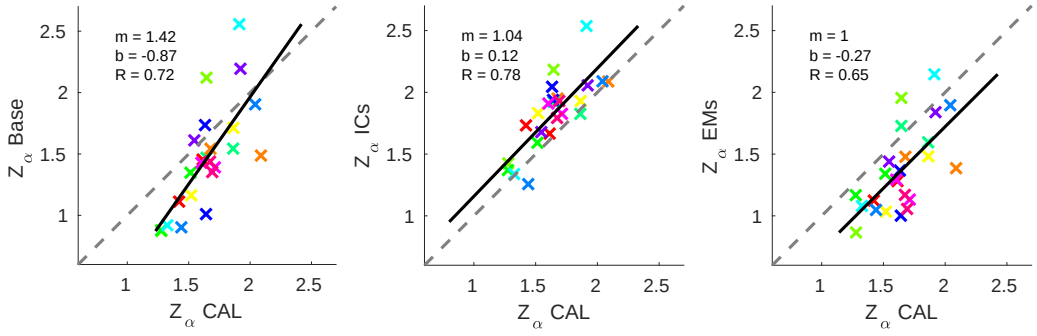

Figure 3.2: Simulated mean extinction height vs CALIOP mean extinction height for: baseline simulation (left), optimised ICs (middle) and optimised emissions (right). The colours of the markers correspond to the coloured outlines of the regions in figure 3.1.

3.4 Results

Figure 3.2 shows scatterplots of mean extinction heights for the base and optimised simulations versus CALIOP observed mean extinction heights. The base model moderately reproduces CALIOP observed Z_α with a correlation R = 0.72, albeit with a large slope (1.42) and offset (-0.87, or -53% of the mean observed Z_α). Both assimilation schemes improve the simulation's ability to reproduce observed Z_α, although IC optimisation performs (R = 0.78, slope = 1.04, offset 0.12 or 7%) better than emission optimisation (R = 0.65, slope = 1.00, offset = -0.27 or 16%). This is not entirely surprising as the emissions have less direct control over the vertical distribution, and the AEROCOM regions represent a variety of environments with different aerosol sources.

Figure 3.3 shows column AOD observed by CALIOP (top row) and the baseline GEOS-Chem simulation coincidently sampled with CALIOP (bottom row) averaged over January (left column) and July (right column) of 2007. GEOS-Chem values which fell below the CALIOP detection limits were filled to the detection limit values, as for the CALIOP observation data used in the assimilation. The simulation shows lower column AOD than CALIOP observations over most of the globe, except in northern Africa in the Sahara area, and over the mid-Atlantic ocean where GEOS-Chem shows values up to 1.3, while CALIOP only reports up to 0.59.

In general, CALIOP reports slightly higher column AOD with a global average difference $\mathrm{AOD_{GC}} - \mathrm{AOD_{CAL}} = -0.02$, with individual column differences ranging

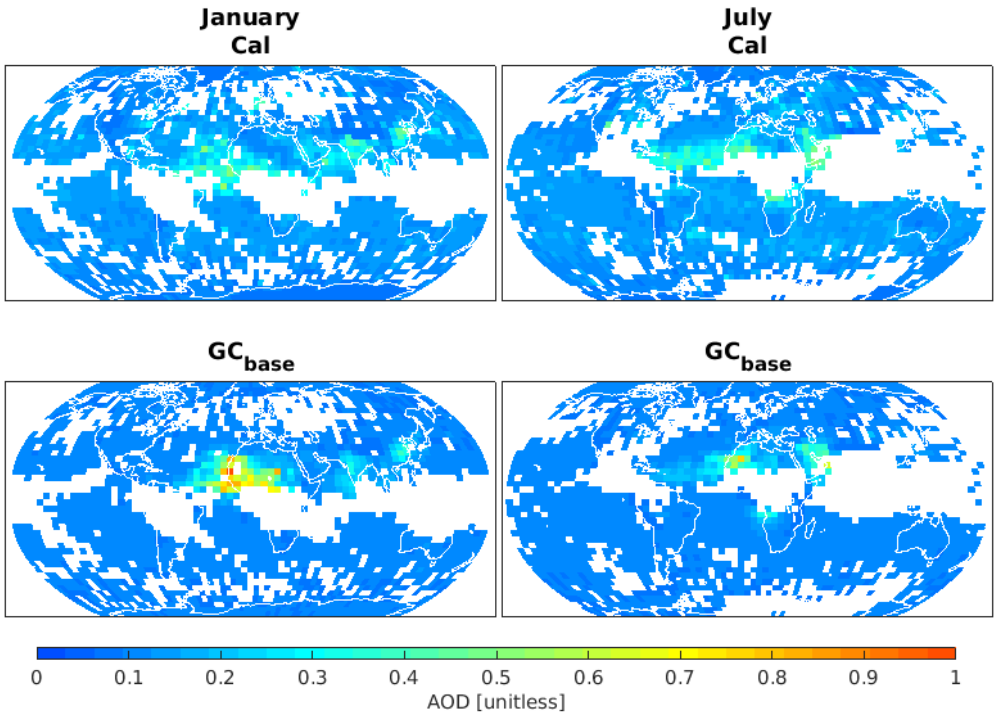

Figure 3.3: AOD below 10 km. Top row shows CALIOP superobservations averaged over January (left) and July (right0) of 2007, bottom panel shows baseline simulation sampled coincidentally with CALIOP observations.

from -0.76 to 0.98. The highest values are (i.e., areas where CALIOP extinction is lower than GEOS-Chem) observed only around the Sahara region (mean difference = 0.2), while several other areas including southern Africa and northern India show lower than average differences, indicating CALIOP extinction is higher than GEOS-Chem. Although figure 3.3 shows values only below 10 km altitude, during the study period, CALIOP reported mostly clean air above 10 km, as did the simulation.

Figure 3.4 shows how the different simulations (baseline, optimised emissions, and optimised ICs) compare to observations of average AOD below 10km, sampled at times and locations where CALIOP superobservations were available. The baseline simulation (top row) underestimates observed AOD almost everywhere globally in both January and July, but greatly overestimates AOD over the Sahara in January. The optimised emissions simulation results in an slight increase in AOD everywhere except (mean difference = -0.02) over the Sahara (mean difference = 0.02) and the Middle East. IC optimisation resulted in a larger general increase in AOD (mean difference = -0.008) but were only able to modestly decrease AOD over the Sahara in January (mean difference = 0.18) in accordance with the observations.

Figure 3.5 compares the base simulated extinction profiles, as well as simulated profiles after different optimisations, with observed extinction profiles averaged over different geographical regions. In the Land and Ocean cases, the baseline simulation underestimates aerosol extinction in the entire troposphere, but especially the bottom 1 km. Over the Sahara the situation is reversed with the baseline model overestimating aerosol extinction. The IC optimisation scheme improves results in all locations for January and July (mean improvement in RMSD: 26%) except the Sahara Outflow region in January, which showed an 8% increase in RMSD from 0.0193 for the baseline simulation to 0.0209 for the optimised results. Improvements were similar for the emissions optimisations, with an average improvement of 26%.

Figure 3.6 shows the optimised scaling factors for SSA and dust, that is, the ratio by which the local emissions are multiplied to get the optimised emissions. The optimisation generally increased SSA emissions over the whole ocean, with the exception of the northern Indian Ocean, where emissions decreased as much as 32%. The mean value for SSA scaling factors over ocean pixels was 1.5, meaning on average the optimisation increased sea-spray emissions by 50%. For dust, emissions were

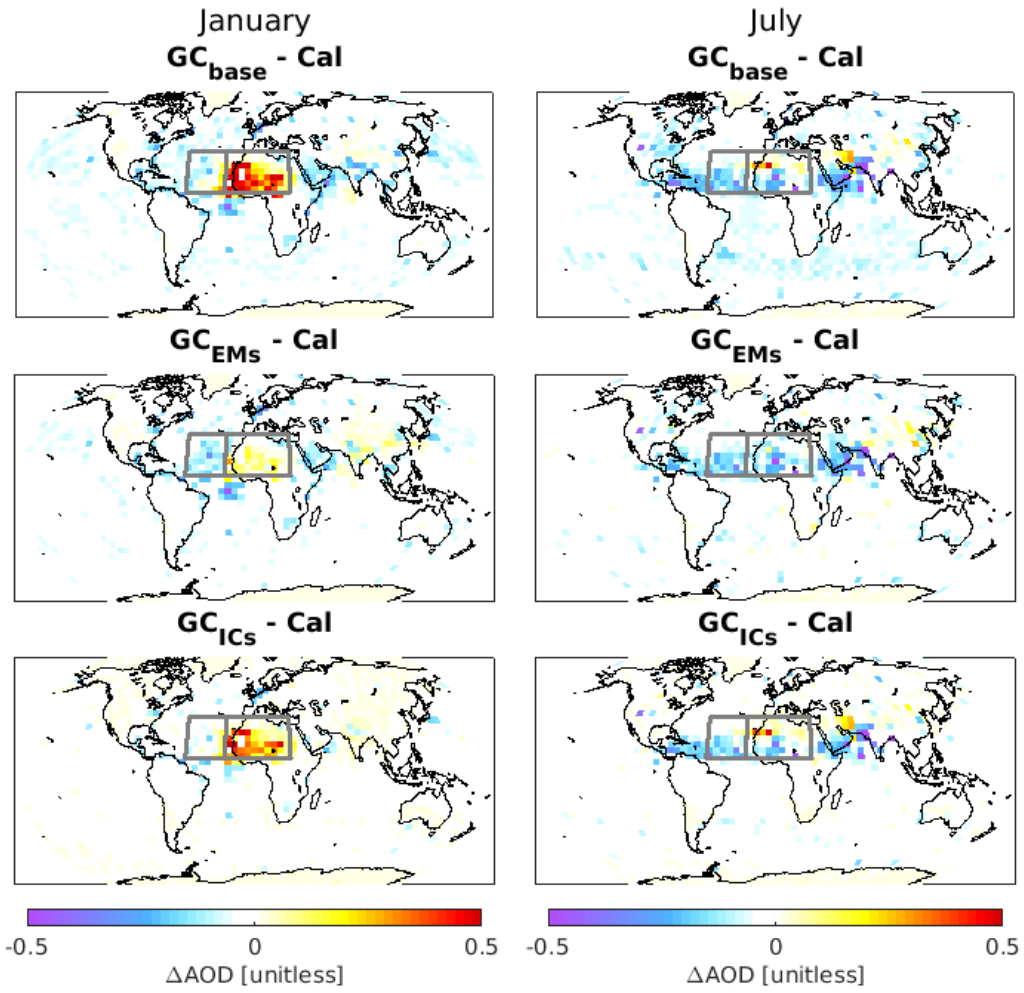

Figure 3.4: Difference between simulated column AOD and CALIOP observed AOD from: baseline simulation emissions (top row), 1-month runs with optimised emissions (middle row) and 1-day runs with optimised ICs, coincidently sampled with CALIOP superobservations, for January (left column) and July (right column) of 2007. Dark grey boxes indicate Sahara and Outflow regions used in figures 3.5.

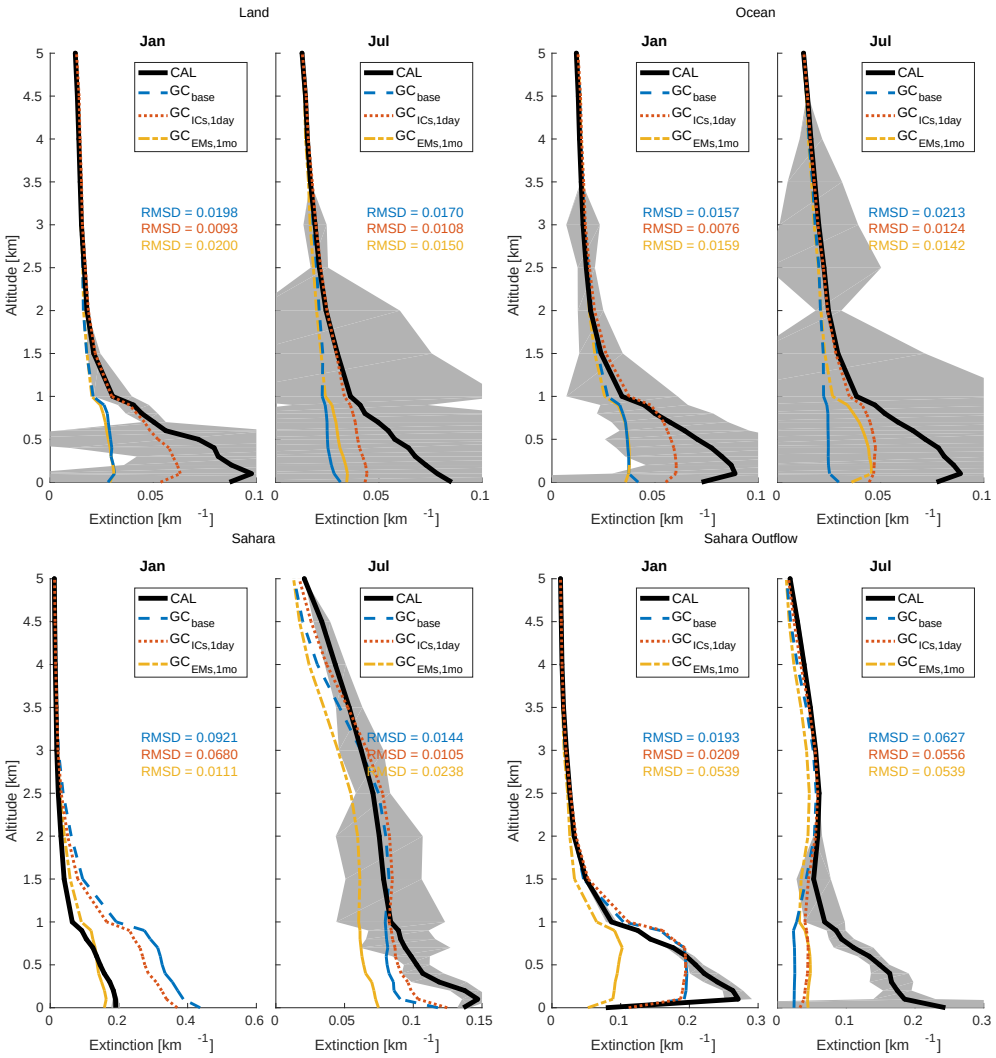

Figure 3.5: Average aerosol extinction profiles for January and July assimilation periods for all land (top left), all ocean (top right), the Sahara region (bottom left) and the Saharan outflow region over the Atlantic Ocean (bottom right). Observations are shown in solid black with grey indicating the uncertainty bounds on the average values. Other profiles show the baseline simulation, 1-day assimilation window for ICs, and 1-month assimilation for emissions.

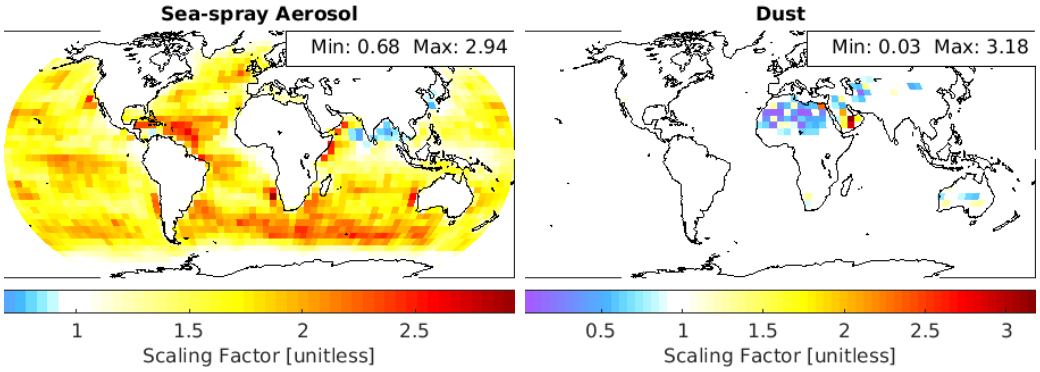

Figure 3.6: Optimised emissions scaling factors for SSA and dust for 1-month emissions optimisation averaged for January and July, 2007. The left plot shows the optimised scaling factors for SSA and the right plot shows optimised scaling factors for dust.

greatly decreased in the Sahara but increased on the Arabian peninsula. Slight shifts in dust were also present in Australia and central Asia.

3.5 Discussion

Data assimilation performs best when both the model and observations are unbiased, that is, on average, the difference between the model state or observations and the true state is zero. However, it is still not entirely clear how to obtain this condition and there is a rich literature on debiasing models and observations.

4DVAR data assimilation is generally designed to optimise the global state of the atmosphere. In this study, there were large regional differences in the performance of the assimilation. Optimised emissions were able to correct the high AOD over the Sahara in January, which may indicate that emissions are the predominant driver of concentrations there. At the same time, over the mid-Atlantic, the optimised emissions decreased agreement with observations substantially in the Sahara outflow region in January (179% increase in RMSD). The difficulty of the model to capture the observed signals in both the Sahara and the mid-Atlantic regions simultaneously may indicate a possible issue with model transport in this area. It is also possible that model, the observations, or both are not properly capturing the size distribution of aerosols in these regions leading to shifts in the burden due to incorrect deposition, or changes in the radiative properties of the plume as it moves out over the ocean.

With so many free parameters to optimise, it is impossible to guarantee that assimilation converges to the global minimum. A number of methods have been shown to improve the changes of finding the global minimum such as using the 2nd derivative or Hessian matrix or adding random noise to the descent direction, but I did not employ any of these techniques in this thesis. This would be a good future project in general for the GEOS-Chem adjoint. I did perform a simple sensitivity test where I randomly perturbed the initial conditions or emissions with 1% random noise and the model solutions correlation with $R^2 > 0.99$ with the base conditions, indicating the solution is robust to changes in the model inputs, if not guaranteeing uniqueness.

One weakness of this study is the lack of independent data for confirmation. To partially account for this, for the IC optimisations I performed comparisons between the assimilated model and CALIOP observations not used in the assimilation by using the "forecast" values. This comparison allowed me to show quantitatively that the assimilation allows us to better predict the state of the atmosphere past the available observation data, but does not account for any systematic errors or biases in the observation data. One possible source of data is the recently released NASA Atmospheric Tomography Mission (ATom) dataset (Brock et al., 2019), however, there were no observations of total aerosol data from this dataset; rather they are synthesised from a variety of instruments, most of which operate on single particles or very small sizes (< 0.5 µm).

The treatment of BDL values in the CALIOP profiles is a matter of some debate in the literature (Toth et al., 2018). Our choice to include BDL observations but set them to the detection limit may have biased our results positive compared to observations with a higher signal-to-noise ratio. There are several other choices which should be tested in this framework. One possibility would be not using BDL observations, but this would greatly reduce the number of observations available, and in the event that CALIOP reports BDL but GEOS-Chem reports elevated extinction, we have thrown away useful information. In light of this, it seems the likely that the best option would be to only include BDL observations when GEOS-Chem reports extinction above the CALIOP detection limit.

The optimised sea-spray emissions enabled by the full adjoint of sea-salt aerosol

are consistent with observations that the SSA burden is underestimated by up to 45%(Grythe et al., 2014), however, these results should be taken with a grain of salt (pun intended). The marine atmosphere tends to be fairly clean, and these results may be impacted by my decision to include BDL observations. A counter-argument to this is that I included the BDL cutoff in the GEOS-Chem profiles in Figure 3.5 and they remain well below the observed CALIOP profiles.

3.6 Conclusions

In this study, I have presented a proof-of-concept 4DVAR data assimilation framework for CALIOP L2 Lidar profiles using the GEOS-Chem CTM and its adjoint. To perform this assimilation, I updated the adjoint of the GEOS-Chem to include the adjoint of sea-salt aerosol. This will allow the adjoint model to match the forward model more closely in areas where sea-salt aerosols are present and active. I also implemented an observational operator for the assimilation of CALIP L2 Lidar profiles. With this updated adjoint, I demonstrated 4DVAR data assimilation to optimise either the initial model state or aerosol and precursor emissions. I showed that both of these assimilation schemes can highlight different areas where simulations can be improved. I showed that by optimising emissions, the models representation of $PM_{2.5}$ over the Sahara is improved, but not the outflow area, whereas optimising initial conditions improves representation of the outflow region but not over the Sahara. These two contrasting outcomes suggest improvements can be made to both emissions and model processes such as tropospheric mixing.

Chapter 4

Global Estimation of Ambient Particulate Air Pollution Concentration and Uncertainty Using Mixture Density Networks

4.1 Abstract

Epidemiological studies of fine particulate matter ($PM_{2.5}$) require accurate, high-resolution concentration data with well-characterised errors. In this study, we trained a computationally efficient artificial neural network to produce probability distributions of ambient $PM_{2.5}$ concentrations on a $0.01^\circ \times 0.01^\circ$ grid based on input data from a satellite-derived $PM_{2.5}$ data set, and population and land-use data. We show that training the model naively based only on monitoring data reproduces the monitor data with high fidelity but predicts lower concentrations ($\sim$20-30 µg m^{-3}) in the Sahara Desert than in central Africa (>100 µg m^{-3}), which is inconsistent with current understanding. To remedy this, we include roughly 2000 randomly selected locations with data taken from the high-resolution satellite-derived $PM_{2.5}$ dataset used as input to our model but give it a high uncertainty. Our model achieved an average correlation R^2 of 0.93 and an average RMSD = 5.00 µg m^{-3} in 10-fold cross validation against the World Health Organization Cities 2018 database.

4.2 Introduction

Ambient particulate matter with an aerodynamic diameter less than 2.5 µm ($PM_{2.5}$) ranks as the 10th highest risk factor for morbidity and the 5th highest for mortality (GBD 2017 Mortality Collaborators, 2018; GBD 2017 Risk Factor Collaborators, 2018), making it one of the most important environmental health issues in the world. While measurements of $PM_{2.5}$ concentrations are available for many parts of the world, the density of networks varies and still does not match the natural heterogeneity of the distribution of $PM_{2.5}$ concentrations.

The most successful techniques for estimating high-resolution $PM_{2.5}$ concentrations with geophysical models have included combining satellite measurement of aerosol optical depth, however, these techniques have only recently been able to reproduce surface-level measurements as well as statistical models based on those measurements (van Donkelaar et al., 2015; Shaddick et al., 2017; Hammer et al., 2020). At present, the high water mark is a correlation R^2 of 0.92 against surface monitor data.

The availability of user-friendly frameworks for machine learning such as TensorFlow in the past few years has created a proliferation of new statistical models based on surface monitors for $PM_{2.5}$. A recent review study conducted using PRISMA guidelines narrowed the field down to 46 papers, of which a total of 4 concerned outdoor $PM_{2.5}$ estimation (Rybarczyk and Zalakeviciute, 2018). The studies used a variety of techniques including Random Forest, Support Vector Machines, Clustering, Artificial Neural Networks (which is the approach taken in this study), or a combination of these methods. Most of the covariates used were meteorological, land-use, and proxy measurement in nature. The resulting models achieved spatial correlation R^2s ranging from 0.8–0.91 on regional observation datasets. A few studies designed to create high-resolution exposure/concentration estimates have been done recently with good results, but they have all focused on limited geographic areas such as the continental U.S. (Di et al., 2016), China (Shen et al., 2018) and Western Canada (Yao et al., 2018).

TensorFlow is an open-source machine learning framework provided and maintained by Google [https://www.tensorflow.org]. The framework allows high-level operations to be formed in the open-source programming language Python, which are then efficiently executed using low-level libraries that can take advantage of various computer hardware platforms. The available of Tensorflow allows researchers to create machine learning systems without needing to be experts on the underlying algorithms.

R-INLA is a Bayesian inference package for the R statistical programming language (Rue et al., 2009; Martins et al., 2013). Recently a geostatistical method using the R-INLA method provided a highly accurate, high-resolution global concentration map including uncertainty information (Shaddick et al., 2017). However, this

method required high computational cost, which also had a minor secondary effect of producing artefacts on the map because of the necessary geographical partitioning.

When $PM_{2.5}$ concentrations are used in exposure assessments, it is particularly important to quantify the uncertainties. Ignoring estimation errors in the exposures used to compute concentration response functions can drastically change the shape of those functions Cox (2018), while uncertainty in ambient $PM_{2.5}$ concentrations contributes over 20% of the uncertainty in $PM_{2.5}$-related mortality estimates to in China, India and Latin America (Kodros et al., 2018). In addition to being able to reproduce surface monitoring data not used in training their model with high fidelity, (Shaddick et al., 2017) produces probability distributions of $PM_{2.5}$ concentrations for each geographical point, providing not only a value but also an uncertainty. This is a major innovation as most methods produce single values, and the uncertainty of these values is usually calculated post hoc, by using propagation of error on the assumed uncertainties in the covariates (Brauer et al., 2016). Because of its flexibility, rather than simply making 1:1 predictions, machine learning can be trained to produce probability distributions(Bishop, 1994).

In this study, I use the modern machine learning framework Tensorflow to produce individual $PM_{2.5}$ probability distributions on a high-resolution ($0.01^\circ \times 0.01^\circ$) global grid. The input covariates include geophysical and land-use variables. The model is trained and verified with the WHO2018 Cities surface monitor data. This method allows high-accuracy global coverage with uncertainties and with no discontinuities and low computational cost. To my knowledge this is the first study to use these data in this way.

4.3 Methods

4.3.1 Summary

To create the high-resolution output, I ran an artificial neural network in TensorFlow on all the covariates for each location on a global $0.01^\circ \times 0.01^\circ$ grid, which is the highest resolution available for the input satellite-derived $PM_{2.5}$ (Hammer et al., 2020). The network is trained by minimizing a loss function. This is achieved through an iterative gradient descent algorithm where the gradient of the network's internal parameters

is computed with respect to the loss function, and the parameters are modified in the "downhill" direction until the loss function remains stable for several iterations (Duchi et al., 2011). To train the model, I used surface $PM_{2.5}$ monitoring data; the loss function was computed as the negative log probability that the monitor value was drawn from the distribution produced by the model.

As input to the network, I used geolocation, satellite-derived $PM_{2.5}$ data, aerosol composition from geophysical model output, and land use data. The network is run with those input variables for each location on a $0.01^\circ \times 0.01^\circ$ grid and outputs a probability distribution of $PM_{2.5}$ mass concentration values for the corresponding location; these variables are described in the next section, Section 4.3.2. I present this probability distribution as a mean and standard deviation in the results, although, in practice, the distribution can be almost any shape. Because different locations on the globe share similar land-use and geophysical model data, information about these relationships can be spread geographically by the network.

We used 200,000 iterations of a gradient descent approach to tune the network parameters to minimize the loss function averaged over all available monitors. Because the model is run separately for each point on the grid, resolution is limited only by the resolution of the input covariate data. To generate the final high-resolution data in this study, we applied the trained model to our input data at the highest resolution available for the satellite-derived product which was $0.01^\circ \times 0.01^\circ$ global grid.

4.3.2 Input Data

As predictor variables, or covariates, the network uses latitude, longitude, satellite-derived $PM_{2.5}$, $PM_{2.5}$ composition from a geophysical model, the distance to the closest grid cell with urban land-type, difference in elevation from closest geophysical-model grid-cell centre, and the percentage of the grid cell that is water. The $PM_{2.5}$ composition variables are the faction of $PM_{2.5}$ that is mineral dust, and the fraction of $PM_{2.5}$ that is sulphate, nitrate, ammonium, or organic, and are taken from the GEOS-Chem chemical transport model (CTM). The satellite-derived $PM_{2.5}$ is generated by applying vertical surface-to-column ratios from GEOS-Chem simulations to MODIS satellite aerosol optical depth (AOD) to arrive at a surface $PM_{2.5}$ concentration (van Donkelaar et al., 2015). Elevation data was taken from the ETOPO1

dataset available from NOAA (https://ngdc.noaa.gov/mgg/global/global.html). The land-type data used to determine the nearest urban land-type grid cell and percent water was from MODIS Collection 5 land cover MCQ12Q1(Friedl et al., 2010), which contains 17 different land types in 7 categories. The categories are Forests, Woodlands, Grasses/cereals, Shrublands, Croplands and mosaics, Seasonally or permanently inundated, and Unvegetated. The "Urban" type falls in the Unvegetated category.

4.3.3 Structure of the TensorFlow Model

An artificial neural network in TensorFlow model consists of m "layers." A layer is a matrix operation with output vector $v = f(\mathbf{W}_l\mathbf{u} + \mathbf{b}_l)$, where u is the output of previous layer, $\mathbf{W}_l$ is the weight matrix of layer l, $\mathbf{b}$ is the bias of the layer l, and f is a function used to limit the values each element of $\mathbf{v}$ can take.

In producing estimates of air pollution for use in exposure studies, it is important to include information on the quality of the predictions, i.e., an uncertainty metric. In order to produce this for our dataset, we trained a Mixture Density Network (Bishop, 1994) created using the TensorFlow framework. To achieve this, the output vector of the final layer consisted of the parameters, i.e., mean and variance, for k Gaussian probability distributions, and k weights, ϕ_k, such that $\sum_k \phi_k = 1$. The output of the model for each grid location was, therefore, a probability distribution $p = \sum_k \phi_k \mathcal{N}(\mu_k, \sigma_k^2)$.

Our model had two densely-connected layers, each layer with 3000 hidden nodes. The final layer consolidated the 3000 intermediate outputs from the second hidden layer down to 9 outputs, which where the weights, means and standard deviations of 3 Gaussian distributions used to model the final probability distribution of the $PM_{2.5}$ concentration at a point in space.

Machine learning models, and artificial neural networks in particular, are known to be quite sensitive to the choice of meta-parameters (e.g., the number of layers, and number of nodes per layer). Additionally, increasing the size of the network brings computational expenses, so the optimal network is one which best reproduces the validation data at the lowest computational cost. Although techniques for choosing the best meta-parameters exist, I did not use any of these. To arrive at the size of the

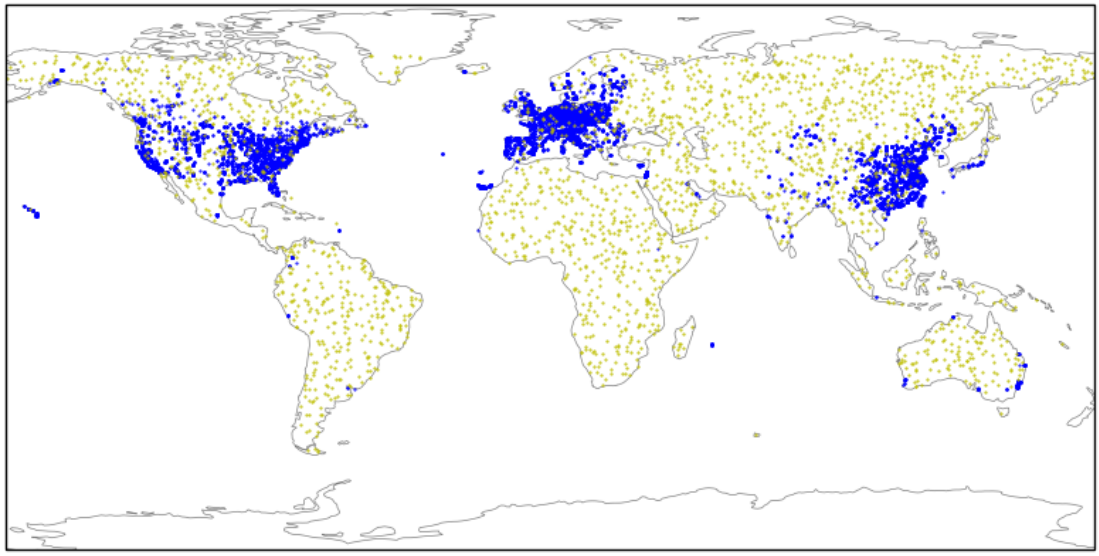

Figure 4.1: Locations of WHO 2018 monitors, in blue, and randomly-selected satellite-derived locations, light green.

network I used, I arbitrarily chose two hidden layers. I started with a small number of nodes and increased this number until the cross-validation R^2 stopped increasing.

4.3.4 Training Data

We trained our model on the recently updated World Health Organization Pollution in Cities dataset (WHO2018), which is extensive in time and space, although coverage is far from complete. Rather than using the city or country averages, we used individual monitoring locations. We filtered the data to exclude annual average measurements that covered less than 75% of the year, leaving 17,247 annual measurements taken at 5,869 locations from the years 2003 to 2017, shown in Figure 4.1. For each monitor value, the model was trained with the covariate data from that monitor location and year.

4.3.5 Training the Model with Uncertainty

For each available monitor for training, we computed a loss function which was the negative log probability that the $PM_{2.5}$ value was drawn from the mixture of Gaussians

produced by the model. That is,

$$\mathcal{L} = \sum_k \phi_k \frac{\left(\mathrm{PM}_{2.5,\mathrm{obs}} - \mu_k\right)^2}{2\pi\sigma_k^2} \tag{4.1}$$

where $\mathcal{L}$ is the loss function, and $\mathrm{PM}_{2.5,\mathrm{obs}}$ is the randomly perturbed monitor value (described in the next paragraph). The monitors were grouped into minibatches of 100 and the network parameters were tuned based on the gradient of the average loss function over the entire minibatch.

In order to represent the uncertainty in the observation data, we randomly drew our monitor data from a normal distribution about the reported annual value with a standard deviation of 30% for $\mathrm{PM}_{2.5}$ monitor data. These uncertainty values were arbitrarily chosen but were intended to capture two sources of error: the error in the individual measurements, and the representativeness error of the measurements, that is, how much the measurements would vary if they were taken at other positions in the $0.01^\circ \times 0.01^\circ$ they are intended to represent. Individual uncertainties associated with these kinds annual of measurements might be expected to be in the few percent range (e.g., Dutton et al. (2009) reported 22% uncertainty on individual gravimetric filter measurements, while Weagle et al. (2018) reported up to 5.2% uncertainty on seasonal average measurements). Representativeness error is more uncertain but a recent land-use regression study reported observed $\mathrm{PM}_{2.5}$ values with a 30% difference between the highest monitor and the lowest monitor in within a roughly 5 km$\times$5 km area in Shanghai (Liu et al., 2016). The system is designed to allow for specific uncertainties to be chosen for each individual measurement, and the shape of the distribution from which the random observations is drawn is easy to change, if such information is available.

By minimizing the loss function as described, we are able to create a model which produces not only the expected value but also the distribution with uncertainty for each location. The training procedure is described in the flow chart in Figure 4.2. In summary, the model is trained by tuning the internal parameters so the output from running the model on the training covariate data most closely reproduces the training $\mathrm{PM}_{2.5}$ surface monitor data. Once this training procedure is complete, the model is run on covariate data for which we have no monitor data to predict the distribution of $\mathrm{PM}_{2.5}$ concentrations.

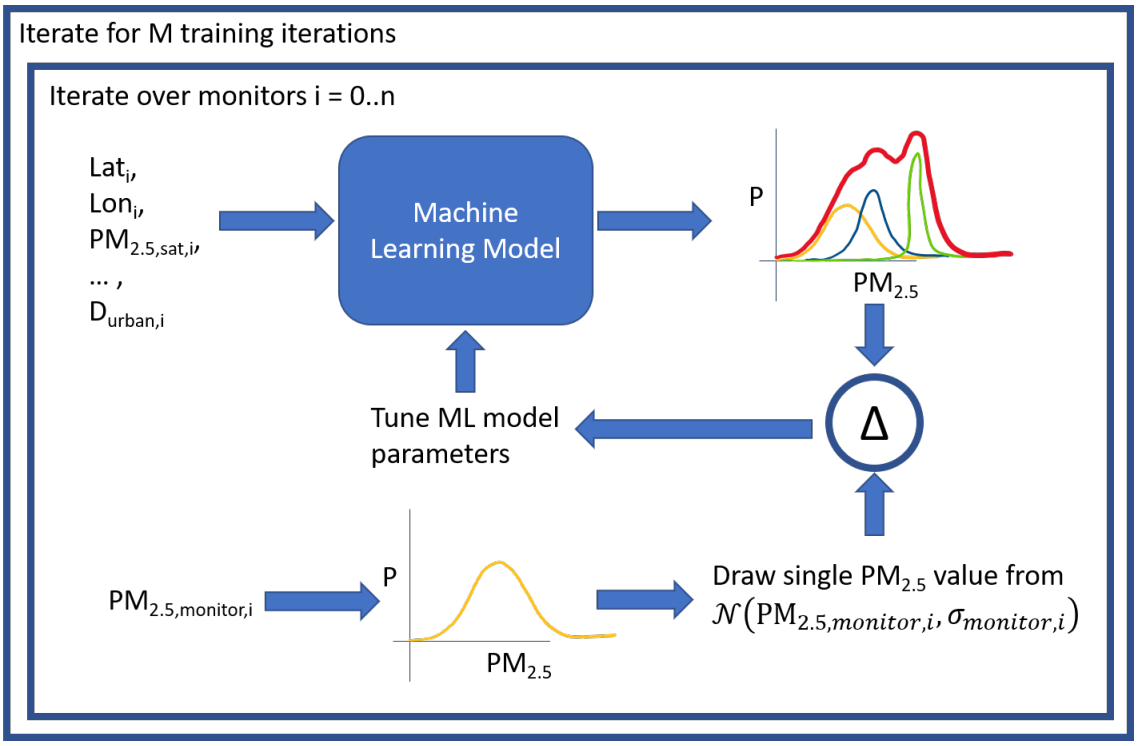

Figure 4.2: Method flow chart for training machine learning model for predicting $PM_{2.5}$ distributions as a mixture of gaussians.

4.3.6 Dealing with Model Blind Spots

One of the main benefits to these kinds of geostatistical methods is the ability to fill in values where there is little or no surface monitoring data. Similarly, the satellite-derived dataset we use as one of our covariates is also useful for filling in spatial gaps in the dataset. Because of the nature of our model, areas with little monitoring data are not well constrained and are also overconfident. To that end, instead of simply training on the surface monitoring data sets we describe below, we included approximately 2000 randomly selected locations where we took values from the satellite-derived data as our target, and gave them a 90% uncertainty. In essence, we trained the network to pass through the satellite-derived values with very high uncertainty in the absence of better information.

In order to examine the contribution of the extra satellite training data, we also trained our system using only the surface monitoring data (the naïve dataset) for comparison with the main results.

4.3.7 Performance Evaluation

To evaluate the performance of the model on unseen data, we performed 10-fold cross validation. That is we split the dataset in to 10ths and trained a model for each possible subset of 90% of the data and compared that model's results with the 10% that was not used in training. We ensured that each split retained the same fraction of monitors from each of the following concentration ranges, 0-25, 25-50, 50-75, 75-100 and > 100 µg m^{-3}

After training the models on only the training data, we compared the mean value produced at the monitoring locations by each model with the monitor value reserved for testing.

4.3.8 High-Resolution Output

Finally, we produce maps of the mean and standard deviation of the final model trained using 100% of the data from the surface monitoring dataset at $0.01^\circ \times 0.01^\circ$. Because of grid-registration issues between the high-resolution output and the available population data, we also generated global $PM_{2.5}$ concentrations on a $0.1^\circ \times 0.1^\circ$ grid to produce population-weighted statistics using the Gridded Population of the World v 4.11 for the year 2015 (Center for International Earth Science Information Network, 2018).

4.4 Results

Figure 4.3 shows an example scatter plot, including the model predictions on both the 90% of data seen in training (blue) and the 10% of data reserved for validation (red). Our full ten-fold cross validation test using the WHO2018 data set produced an average correlation $R^2 = 0.93$ (min=0.86, max=0.95) and an average RMSD = 5.00 µg m^{-3} (min=4.30, max=7.47 µg m^{-3}) against the held-back 10% of monitors. Average R^2 against the training data was 0.95 (min=0.92, max=0.96). In general, the model does very well but tends to underestimate in locations where measured values were above 75 µg m^{-3} This was true for monitors with high concentrations regardless of whether the monitors were included in the training data or not.

Figure 4.4 shows the high-resolution ($0.01^\circ \times 0.01^\circ$) map of the 2014 mean of the

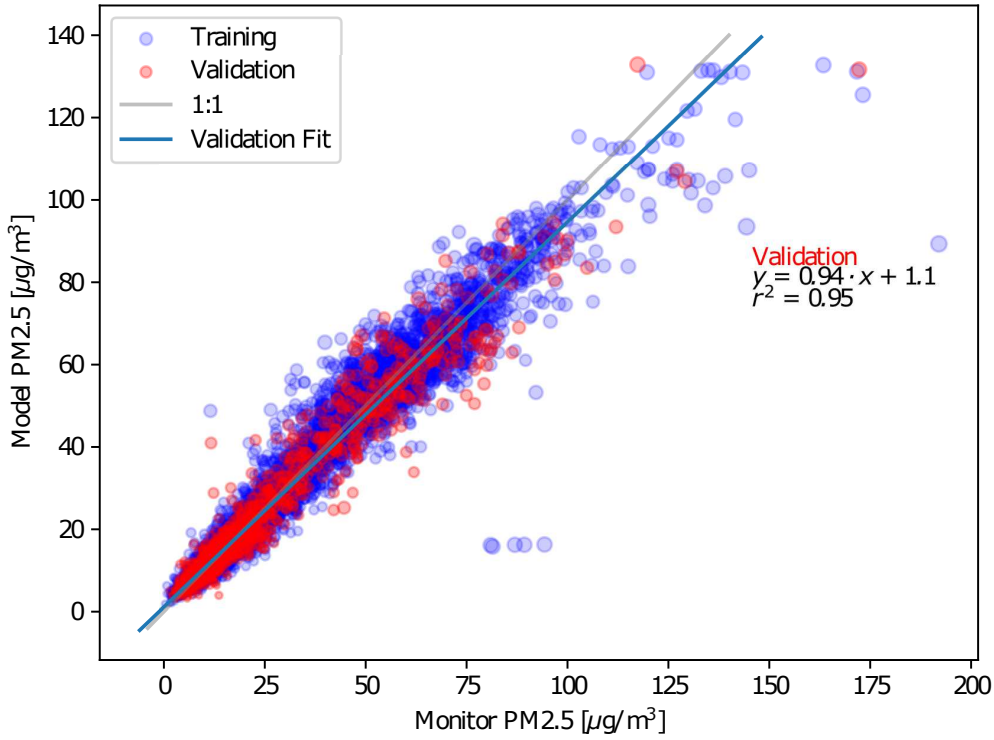

Figure 4.3: Scatterplot of the mixture model vs monitor data for WHO2018 dataset with 90% of annual monitor values used for training and 10% reserved for validation. The relative size of circles indicates standard deviation of mixture model. The monitor data used for training model is shown in blue, while the values shown in red were not used in training the model, i.e., they are validation data. Although randomly selected satellite-derived data were included in the training data, they are not shown on this plot.

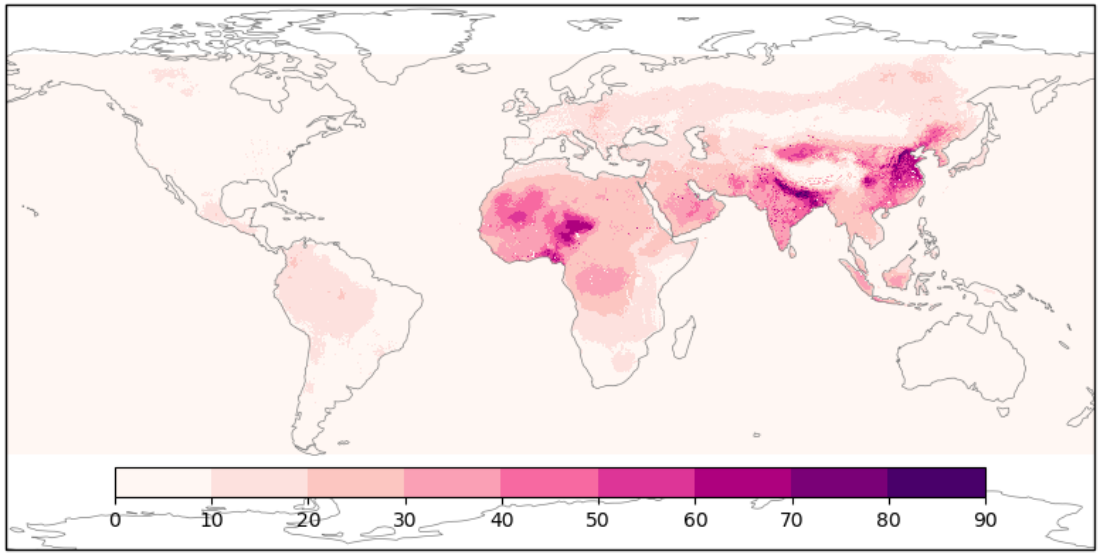

Figure 4.4: Mean $PM_{2.5}$ calculated by our model trained on WHO2018 monitor values and satellite-derived $PM_{2.5}$.

$PM_{2.5}$ distribution produced at each grid location on the globe when the model is trained on the augmented WHO2018 dataset. The highest concentrations are seen on the Indo-Gangetic Plain, in the Sahara and in eastern China.

Figure 4.5 shows the standard deviation of the distribution produced by our model at each location (as a fraction of the mean), which we treat as a measure of the uncertainty in the reported mean. The lowest relative uncertainties are in Europe, eastern North America, and north-eastern China, areas with high densities of $PM_{2.5}$ monitoring data. The highest relative uncertainties are seen in Eastern India and Bangladesh, and the Malay Archipelago, areas with comparatively little monitoring data available. Although the uncertainties are comparable to or even larger than the means in some areas, this does not necessarily imply a high probability of negative values since the output distribution can be any shape.

Since each grid location produces a probability distribution, we can combine these in a population-weighted sense, to achieve a global population-weighted probability density function (PDF) truncated at 0, since negative concentrations are non-physical (Figure 4.6). Although the distributions do not directly contain information about variability in exposure, it seems fair to combine them in this way since most of the variance in our distributions comes from the representativeness error. The global

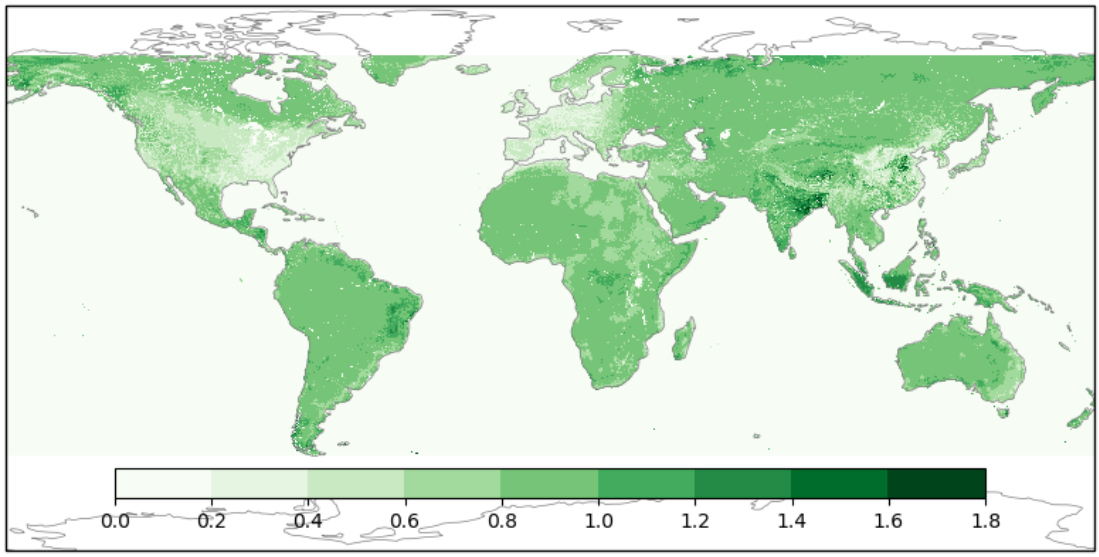

Figure 4.5: Standard deviation as a fraction of mean of ML model $PM_{2.5}$ based on WHO2018 monitor values and satellite-derived $PM_{2.5}$

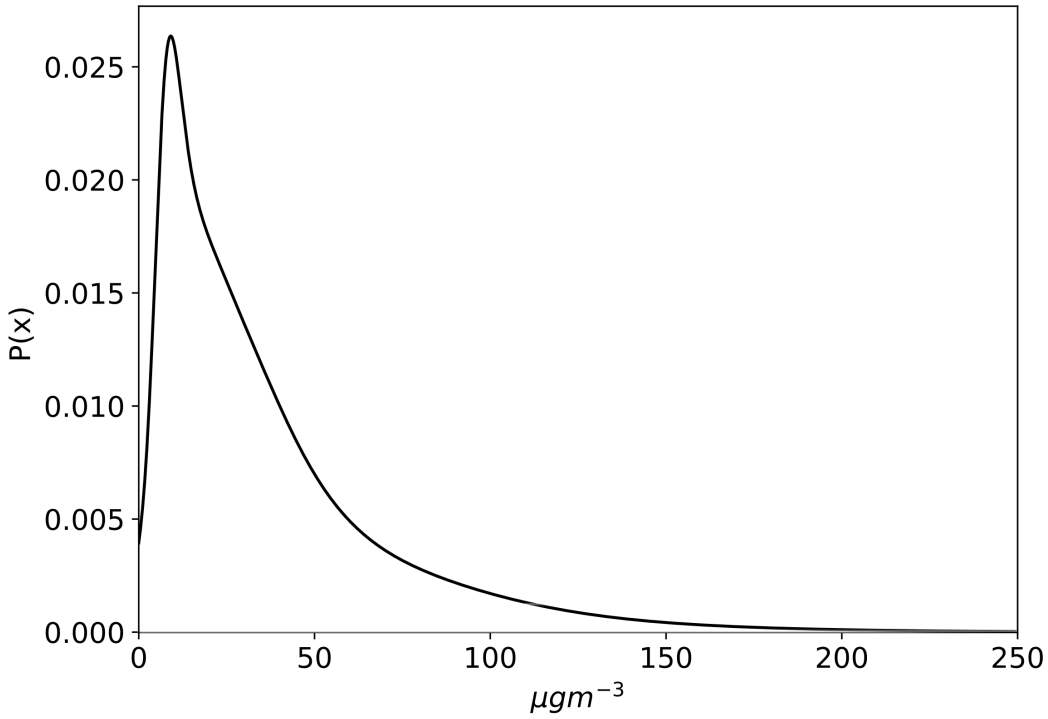

Figure 4.6: Global population-weighted $PM_{2.5}$ exposure probability density function produced by the model.

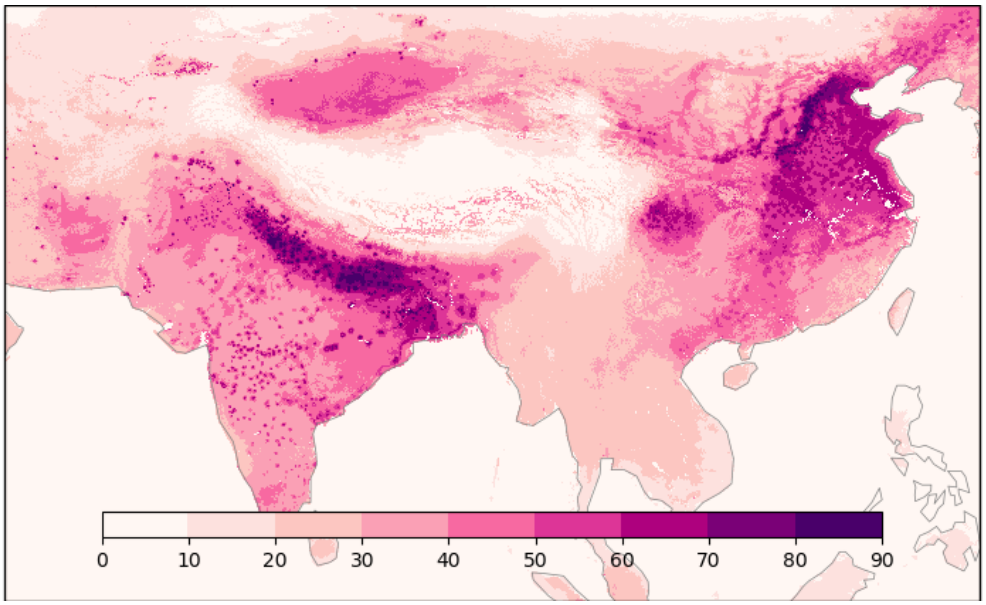

Figure 4.7: Mean $PM_{2.5}$ values predicted by ML model, zoomed in on Eastern Asia to show spatial heterogeneity.

mean $PM_{2.5}$ exposure from our model was 36.1 µg m^{-3}, which is somewhat higher than the 32.0-32.6 µg m^{-3} found in recent works (Li et al., 2017; Weagle et al., 2018). The global population-weighted distribution has a standard deviation of 35.9 µg m^{-3}, but this high standard deviation is at least partially caused by the skew of the distribution, which has a sharp peak at low values but maintains a significant value well above 100 µg m^{-3} while tailing off above 200 µg m^{-3}. Integrating from the WHO guideline concentration of 10 µg m^{-3} to 1000 µg m^{-3} gives 83%, which equates to 5.9 billion people living with exposures in excess of 10 µg m^{-3}.

In previous geostatistical models, the contribution of the horizontal location to the output must be smooth and its shape specified a priori, which can limit the level of detail available in the output. Because the ML model is not constrained in its choice of the shape of the function of the geographical location covariates, the model produces a more heterogeneous estimate, while nevertheless maintaining good correlation with the training data. Figure 4.7 shows a zoomed in section of China with visible features as small as the grid-cell size although the standard deviation values for the same map section appear smooth over large areas but decrease in the highest concentration grid cells (appendix figures), lending confidence that the spatial heterogeneity is not an artefact.

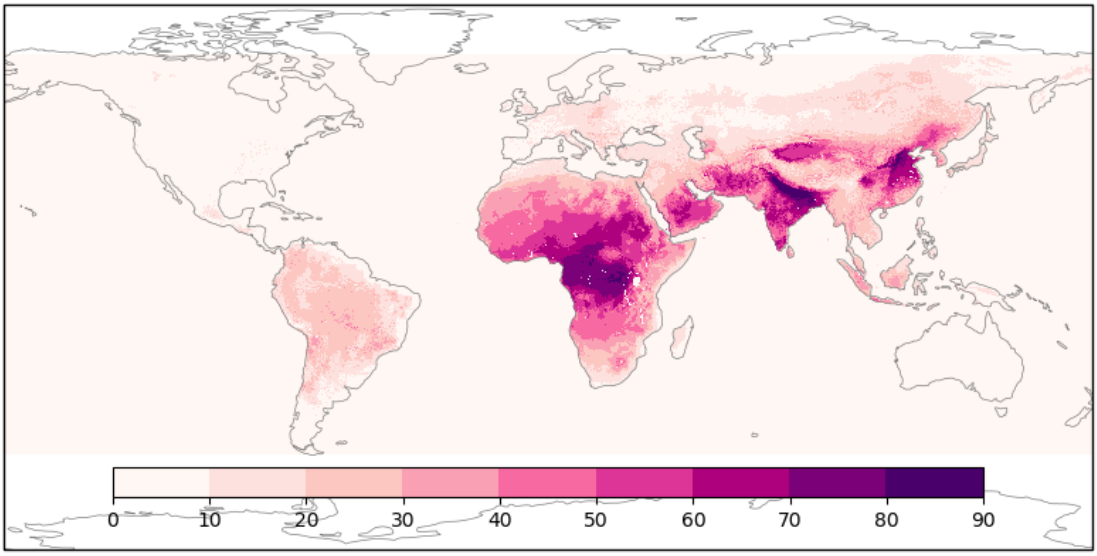

Figure 4.8: Mean $PM_{2.5}$ values predicted by ML model trained with only surface monitoring data. This dataset provided equally good correlation with the training and test data as the model trained with surface monitoring and some satellite-derived data, but provides a drastically different global distribution.

In order to examine the effects of adding satellite-derived data to the training set, we also trained a model on only the monitor data or comparison. When trained on the naïve data set (with only the monitoring data), the model performs as well as the model trained on the augmented dataset (the monitoring data plus satellite-derived values) at predicting the values at monitor locations (Figure 4.9). The correlation R^2 for held-back validation monitors had a mean value of 0.93 (0.91 to 0.94), and RMSD was 5.18 µg m^{-3} (min=4.64 µg m^{-3}, max=5.91 µg m^{-3}) which is very close to the correlation seen in our full model. However, because of the sparsity of monitoring data in certain geographical areas and for certain land types, the naively-trained model produces values which are not inline with our current understanding of global $PM_{2.5}$ distributions (Figure 4.8). Large differences appear over the Sahara, where the naively-trained model shows very little $PM_{2.5}$, and Central / Easter Africa and the Middle East where the naively-trained model shows much higher $PM_{2.5}$ than the full model. In both regions the full model more closely matches other available estimates. The uncertainties in these areas are also quite small (appendix figures), indicating the model is quite confident in its values, even though they are inconsistent with our

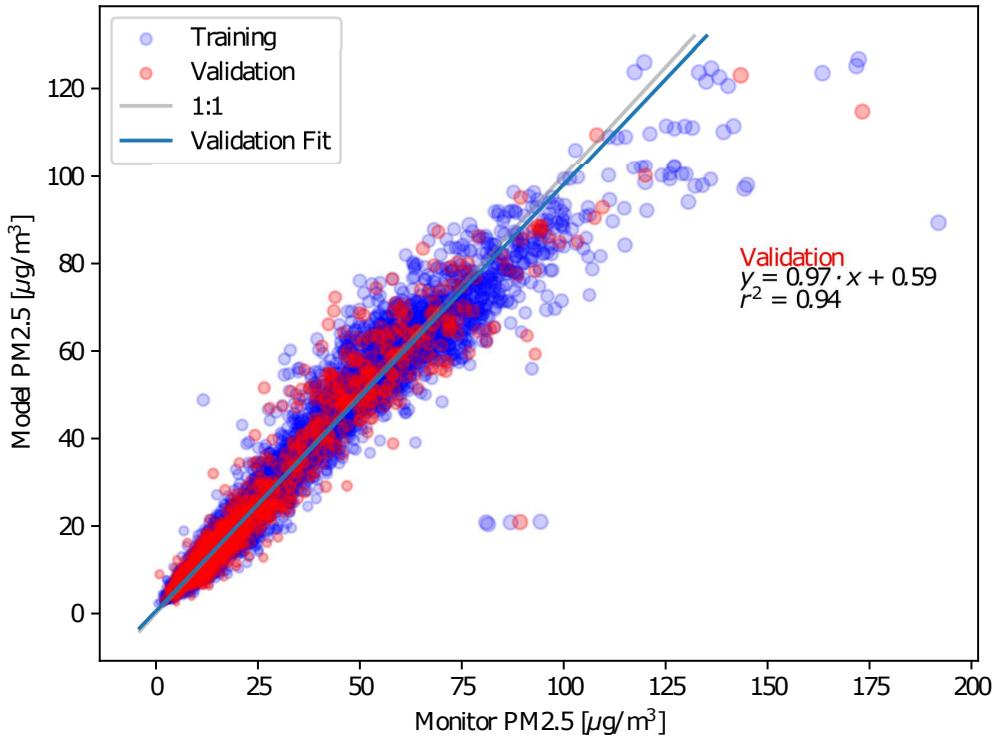

Figure 4.9: Scatterplot of mixture model trained using only monitor data vs monitor data for WHO2018 dataset. Relative size of circles indicates standard deviation of mixture model. Data used for training model shown in blue, while values shown in red were not used in training the model.

current understanding.

Much of the power of deep learning models comes from essentially being able to define different coefficients on the input covariates at each location based on the other covariates at that location; even though there is no monitoring data for a given location, the similarity of the underlying covariates to areas with monitoring data allows the model to make an accurate prediction at the unmonitored location. The complexity of these relationships can lead to some difficulty in interpreting the results, whereas less complex techniques such as regression model present specific coefficients indicating how strongly each input variable affects the output. We ran a sensitivity analysis and produced a map for each covariate, indicating how strongly the final $PM_{2.5}$ mean at that location was impacted by that covariate (appendix figures), if all other input covariates remain at their local values.

Globally, the largest contributors to the global distribution are the satellite-derived $PM_{2.5}$ (Figure S1-1), Dust Fraction (Figure S1-2) and sulphate-nitrate-ammonium-OC (SNAOC) fraction (Figure S1-3), although the magnitude and direction of the relationships vary widely. In particular, there are strong positive relationships between satellite-derived $PM_{2.5}$ and predicted $PM_{2.5}$ in Central Africa and much of Asia, i.e., when all other variables are equal in this region, increasing satellite-derived $PM_{2.5}$ increases predicted $PM_{2.5}$. Conversely, there are strong negative relationships in northwestern Africa and Eastern Europe, i.e., increasing satellite-derived $PM_{2.5}$ *decreases* predicted $PM_{2.5}$. There is a strong positive relationship between dust fraction and predicted $PM_{2.5}$ in many arid regions including the Sahara, the middle East, central Asia and Australia. Strong positive relationships appear between SNAOC fraction and predicted $PM_{2.5}$ (Figure S1-4) in the United States, South America, Northern and Eastern Europe , much of the Indo-Gangetic Plane and northern Australia, while strong negative relationships appear in eastern Europe, central and western Africa, and East Asia. The relationships with distance to urban land type (Figure S1-5) and elevation difference (Figures S1-6) are quite heterogeneous, reflecting the small-scale nature of these covariates.

It is also worth noting that, in principle, this analysis can and has been done using regression analysis, with similar performance (measured by correlation R^2 and RMSE) (Hammer et al., 2020), but because of the open development community and wide

popularity of Tensorflow, this model is more flexible and requires less computation time to train. It is also possible that relationships between the input covariates not available to the regression model (i.e., higher-order terms, products of different covariates) appear in my ML model, although this is difficult to prove.

4.5 Discussion

Overall, the model is able to accurately reproduce the monitoring data, achieving a correlation R^2 of 0.93 against the validation data. This compares very favourably with Shaddick et al. (2017), a similar study on an older version of the surface monitoring dataset, which achieved a correlation R^2 of 0.91 against the *training* data (where our model achieved 0.96; correlation against test data was not reported), and Hammer et al. (2020) which achieved a validation correlation R^2 of 0.92 on the WHO 2018 Cities database. Our model tends to underestimate the measurements at high concentrations. However, this a problem that most other models have suffered to a similar extent e.g. (Van Donkelaar et al., 2016; Shen et al., 2018). Some of the impact of this on exposure estimation can be ameliorated by the fact that the model produces probability distributions for each location and indeed, in Figure 4.3, it can be seen that the values furthest from the linear best fit have the largest circles, indicating a large variance in the model prediction.

The covariates used in this study were chosen largely to match previous similar work and because of their ready availability. This framework is easily adaptable to new covariates, although I did not test other variables. Future work could examine the impact of systematic approaches for variable selection, such as forward selection (Khan et al., 2017) or Markov Blankets(Tsamardinos et al., 2003). It is possible that the limited number of covariates applied in this study contributed to the model's difficulty in producing good estimates in areas with especially sparse monitoring data. However, we showed that using the best high-resolution geophysical model data as part of the training process we were able to restore predictions in sparsely monitored areas to be consistent with current understanding.

The satellite-derived $PM_{2.5}$ covariate is in essence a compound covariate consisting of satellite AOD and CTM output including vertical distribution. It would be interesting to see how including these variables separately rather than combined into

satellite-derived $PM_{2.5}$ would affect the results. I would expect the satellite AOD to be impacted by the fact that observations are only available in the day and under clear-sky conditions. It is therefore possible that the ML model would find areas where the AOD was more or less reliable than the satellite-derived $PM_{2.5}$ input, strengthening the model's predictions.

One strength of this study is the high level of spatial heterogeneity in the modeled means. Since the underlying spatially varying functional form is not specified a priori, the model can infer high spatial resolution. Also, the model does not assume a linear (or any other particular shape) response to the input variables. Because of the sparse nature of the monitoring data, it is difficult to tell whether the spatial structure is real or an artefact of the model. Additionally, the model output represents point measurements while the map colours represent area averages. Nevertheless, similar differences in the measurement data are seen over similar distance scales, so the spatial structure is not inconsistent with the measurement data.

Based on the global PDF, we found that only 83% of the world's population exceeds the WHO guideline of 10 µg m^{-3}. This value is less than the 87% reported in Brauer et al. (2016) or 92% reported in Shaddick et al. (2017). If instead the calculation is made based on grid squares whose medians exceed 10 µg m^{-3}, we get 88% of the world's population living in grid cells with medians exceeding 10 µg m^{-3} The difference in the two numbers is because the second method assumes all people in a given grid cell are exposed to the exact same concentration, while the first method applies a distribution to the population in each grid cell.

The choice of a mixture of Gaussian distributions was driven mainly by previous work and the mathematical elegance of the loss function. One consequence of this choice is the need to truncate the distribution at 0 to avoid non-physical negative $PM_{2.5}$ concentrations. It should in principle be possible to model the parameters of a mixture of lognormal, gamma or Poisson distributions instead, making it possible to achieve distributions with 0 probabilities for all $PM_{2.5}$ concentrations < 0, but care would have to be taken in defining the loss function to ensure the resulting distributions accurately reflect the observation data.

4.6 Conclusions

This work presents a new geostatistical machine learning framework that provides global high-resolution data $PM_{2.5}$ data including uncertainties at low computational cost. The model produces maps for the entire populated land area of the globe based on geophysical modeling, satellite observation, and land-use data. The model's resolution is only limited by the resolution of the available input covariate data. Because the model produces probability distributions for each grid location, giving detailed information about the spatial scale of uncertainty, this data is suitable for epidemiological input.

In future, additional covariates should be tested to see if they improve the model's fit with the surface monitor data. As additional surface monitoring becomes available, it would be interesting to test the model trained only on the older data to see if the relationships the model has learned continue forward in time, although better results would be expect if the model is retrained using new data. Because of the low computational cost of training the model, this should be easy. The parameters of the error distribution of the monitor data should also be revisited; it seems likely that a lognormal distribution would be more appropriate, and a more rigorous determination of an appropriate uncertainty should be performed.

Chapter 5

Conclusion

In this thesis I have attempted to take advantage of recent improvements in computational methods to understand the state of atmospheric aerosol and its impacts on human health. In particular, I relied heavily on the adjoint of the chemical transport model GEOS-Chem. Some of the benefits of using this powerful tool include global coverage and results which are easy to understand in the context of a global chemical transport model.

By extending the adjoint of GEOS-Chem I was able to take advantage of state-of-the-science epidemiological models to provide quantitative analysis of the sources of global mortality due to $PM_{2.5}$ exposure. My model extensions were added to the official codebase and have been used in other projects.

I was also able to use the model to assimilate CALIOP satellite lidar profiles to improve GEOS-Chem's 3D representation of aerosol. This analysis should provide some guidance in the updating of the mineral dust and sea-salt aerosol schemes in the model in future.

I also used recently available machine learning tools to provide the highest resolution global map of ambient $PM_{2.5}$ concentrations, complete with localized uncertainty information, which reproduces surface monitoring data at the highest fidelity yet seen. I hope this data will be helpful to the epidemiological research community. Just as with the future development of the adjoint, future developments in both machine learning, and the underlying data source will improve $PM_{2.5}$ concentration and exposure estimates even further in the future.

5.1 Future Work

The adjoint of GEOS-Chem is not a complete copy of the forward model code. As demonstrated by the requirement for me to write the sea-salt adjoint code 3.3.2, some important processes have not been implemented, such as secondary organic

aerosols, the HEMCO emissions system currently in use in the forward model, and the massive parallelization now available through GCHP. Fortunately, as the model is open-source and has a rich community of scientists working on it, it can be expected that the adjoint will continue to add more code as time goes by, and I have been working on developing the adjoint of GCHP as I finish this thesis.

Additionally, the adjoint of GEOS-Chem has fallen out of date with the forward model codebase. The adjoint of GEOS-Chem is based on version 8, while the forward model is approaching the release of version 13 at the time of writing. Since version 11, the forward model has provided support for high-performance computing, GCHP, which allows the model calculations to be spread over many networked computers. In version 8, global coverage is limited to $2^\circ \times 2.5^\circ$ resolution, which means the smallest grid boxes are 100s of km on a side. The recently developed GEOS-Chem High Performance model (GCHP) allows the GEOS-Chem chemistry to be run at resolutions as small as 15 km on a side (Eastham et al., 2018). Although no adjoint currently exists for GCHP, it is under development at the time of writing. This process will also be helped by the open-source nature of the model. The development of an adjoint model for GCHP will open up many new opportunities for global high-resolution sensitivities and data assimilations.

One limitation of my machine learning study is the arbitrary selection of a small number of input variables. I wrote the code in such a way that it is agnostic to the number or type of input variables, so with some data-preparation work, it is quite possible the ML model could be improved. Additionally, the neural network used was quite simple. A convolutional layer to incorporate data from surrounding pixels while taking advantage of recurring patterns at the global scale could be added.

With the continued refinement of the health impact function by the epidemiology community, eventually a reëvaluation of the response using these updated functions. I hope by that time it will be possible to run the adjoint at higher spatial resolution. Also, while $PM_{2.5}$ mass remains the most robust impactor of health impacts, it seems likely that the real function will be determined to be dependent on chemical composition or mircophysical properties other than total $PM_{2.5}$ mass. A high-resolution, full-chemistry adjoint model will be best positioned to study any new composition-dependent health impact function which arise.

In the CALIOP 4DVAR data assimilation study, I used L2 profiles, which is advantageous because the quality control and uncertainty information has already been performed by a robust and vetted algorithm. However, the use of L2 profiles introduces a number of uncertainties and unnecessary degrees of freedom into the process as well as possibly throwing out useful measurements. It would be interesting to develop an adjoint observational operator based on the L1 lidar returns. This would require radiative transfer equations for the lidar returns of the simulated concentrations and the adjoint forcing code for that radiative transfer model.

Bibliography

Stéphane C. Alfaro, Annie Gaudichet, Laurent Gomes, and Michel Maillé. Modeling the size distribution of a soil aerosol produced by sandblasting. *Journal of Geophysical Research: Atmospheres*, 102(D10):11239–11249, 1997. doi: 10.1029/97JD00403. URL `https://agupubs.onlinelibrary.wiley.com/doi/abs/10.1029/97JD00403`.

Viney P. Aneja, William H. Schlesinger, Qi Li, Alberth Nahas, and William H. Battye. Characterization of the global sources of atmospheric ammonia from agricultural soils. *Journal of Geophysical Research: Atmospheres*, 125(3):e2019JD031684, 2020. doi: 10.1029/2019JD031684. URL `https://agupubs.onlinelibrary.wiley.com/doi/abs/10.1029/2019JD031684`. e2019JD031684 2019JD031684.

Susan C. Anenberg, Larry W. Horowitz, Daniel Q. Tong, and J. Jason West. An estimate of the global burden of anthropogenic ozone and fine particulate matter on premature human mortality using atmospheric modeling. *Environmental Health Perspectives*, 118(9):1189–1195, 2010. ISSN 00916765. doi: 10.1289/ehp.0901220.

Susan Casper Anenberg, J. Jason West, Arlene M. Fiore, Daniel A. Jaffe, Michael J. Prather, Daniel Bergmann, Kees Cuvelier, Frank J. Dentener, Bryan N. Duncan, Michael Gauss, Peter Hess, Jan Eiof Jonson, Alexandru Lupu, Ian A. MacKenzie, Elina Marmer, Rokjin J. Park, Michael G. Sanderson, Martin Schultz, Drew T. Shindell, Sophie Szopa, Marta Garcia Vivanco, Oliver Wild, and Guang Zang. Intercontinental impacts of ozone pollution on human mortality. *Environmental Science and Technology*, 43(17):6482–6487, SEP 1 2009. doi: 10.1021/es900518z. Article.

E. Athanasopoulou, M. Tombrou, S. N. Pandis, and A. G. Russell. The role of sea-salt emissions and heterogeneous chemistry in the air quality of polluted coastal areas.

K. A. Balmes, Q. Fu, and T. J. Thorsen. Differences in ice cloud optical depth from calipso and ground-based raman lidar at the arm sgp and twp sites. *Journal of Geophysical Research: Atmospheres*, 124(3):1755–1778, 2019. doi: 10.1029/2018JD028321. URL `https://agupubs.onlinelibrary.wiley.com/doi/abs/10.1029/2018JD028321`.

Maxime Beauchamp, Bertrand Bessagnet, Cristina Guerreiro, Frank de Leeuw, Svetlana Tsyro, Paul Ruyssenaars, Ferd Sauter, Guus Velders, Frédérik Meleux, Augustin Colette, and Laurence Rouïl. Sensitivity analysis of ammonia emission reductions on exceedances of pm air quality standards. Technical report, 2013.

Michael J Behrenfeld, Yongxiang Hu, Chris A Hostetler, Giorgio Dall'Olmo, Sharon D Rodier, John W Hair, and Charles R Trepte. Space-based lidar measurements of

global ocean carbon stocks. *Geophysical Research Letters*, 40(16):4355–4360, aug 2013. ISSN 00948276. doi: 10.1002/grl.50816. URL http://doi.wiley.com/10.1002/grl.50816.

Michelle L. Bell, Richard D. Morgenstern, and Winston Harrington. Quantifying the human health benefits of air pollution policies: Review of recent studies and new directions in accountability research. *Environmental Science and Policy*, 14 (4):357–368, 2011. ISSN 14629011. doi: 10.1016/j.envsci.2011.02.006. URL http://dx.doi.org/10.1016/j.envsci.2011.02.006.

A.H.W. Beusen, A.F. Bouwman, P.S.C. Heuberger, G. Van Drecht, and K.W. Van Der Hoek. Bottom-up uncertainty estimates of global ammonia emissions from global agricultural production systems. *Atmospheric Environment*, 42(24):6067 – 6077, 2008. ISSN 1352-2310. doi: https://doi.org/10.1016/j.atmosenv.2008.03.044. URL http://www.sciencedirect.com/science/article/pii/S135223100800304X.

Isabelle Bey, Daniel J. Jacob, Robert M. Yantosca, Jennifer A. Logan, Brendan D. Field, Arlene M. Fiore, Qin-Bin Li, Hong-Yu Liu, Loretta J. Mickley, and Martin G. Schultz. Global Modeling of Tropospheric Chemistry with Assimilated Meteorology: Model Description and Evaluation. *Journal of Geophysical Research*, 106: 73–95, 2001. ISSN 0148-0227. doi: 10.1029/2001JD000807.

Francis S. Binkowski and Shawn J. Roselle. Models-3 community multiscale air quality (cmaq) model aerosol component 1. model description. *Journal of Geophysical Research: Atmospheres*, 108(D6), 2003. doi: 10.1029/2001JD001409. URL https://agupubs.onlinelibrary.wiley.com/doi/abs/10.1029/2001JD001409.

Christopher M. Bishop. Mixture density network. Technical report, Aston University, 1994.

JD Blando, RJ Porcja, TH Li, D Bowman, PJ Lioy, and BJ Turpin. Secondary formation and the Smoky Mountain organic aerosol: An examination of aerosol polarity and functional group composition during SEAVS. *Environmental Science & Technology*, 32(5):604–613, MAR 1 1998. ISSN 0013-936X. doi: 10.1021/es970405s.

O. Boucher, D. Randall, P. Artaxo, C. Bretherton, G. Feingold, P. Forster, V.-M. Kerminen, Y. Kondo, H. Liao, U. Lohmann, P. Rasch, S.K. Satheesh, S. Sherwood, B. Stevens, and X.Y. Zhan. *Climate Change 2013: The Physical Science Basis. Contribution of Working Group I to the Fifth Assessment Report o the Intergovernmental Panel on Climate Change*, chapter Clouds and Aerosols, pages 571–657. Cambridge University Press, Cambridge, United Kingdom and New York, NY, USA, 2013a.

Olivier Boucher, David Randall, Paulo Artaxo, Christopher Bretherton, Graham Feingold, Piers Forster, Kerminen Veli-Matti, Yutaka Kondo, Hong Liao, Ulrike Lohmann, Philip Rasch, S.K. Satheesh, Stephen Sherwood, Bjorn Stevens, and

Zhang Xiao-Ye. Clouds and aerosols. In Thomas F. Stocker, Dahe Qin, Gian-Kasper Plattner, Melinda M.B. Tignor, Simon K. Allen, Judith Boschung, Alexander Nauels, Yu Xia, Vincent Bex, and Pauline M. Midgley, editors, *Climate Change 2013: The Physical Science Basis. Contribution of Working Group I to the Fifth Assessment Report of the Intergovernmental Panel on Climate Change*. Cambridge University Press, 2013b.

B. L. Boys, R. V. Martin, A. van Donkelaar, R. MacDonell, N. C. Hsu, M. J. Cooper, R. M. Yantosca, Z. Lu, D. G. Streets, Q. Zhang, and S. Wang. Fifteen-year global time series of satellite-derived fine particulate matter. *Environ.sci.technol.*, 48(19): 11109–11118, 2014. doi: 10.1021/es502113p.

M Brauer, M Amann, R T Burnett, A Cohen, F Dentener, M Ezzati, S B Henderson, M Krzyzanowski, R V Martin, R Van Dingenen, A van Donkelaar, and G D Thurston. Exposure assessment for estimation of the global burden of disease attributable to outdoor air pollution. *Environ Sci Technol*, 46(2):652–660, 2012. ISSN 1520-5851. doi: 10.1021/es2025752. URL `http://www.ncbi.nlm.nih.gov/pubmed/22148428`.

Michael Brauer, Greg Freedman, Joseph Frostad, Aaron van Donkelaar, Randall V. Martin, Frank Dentener, Rita van Dingenen, Kara Estep, Heresh Amini, Joshua S. Apte, Kalpana Balakrishnan, Lars Barregard, David Broday, Valery Feigin, Santu Ghosh, Philip K. Hopke, Luke D. Knibbs, Yoshihiro Kokubo, Yang Liu, Stefan Ma, Lidia Morawska, José Luis Texcalac Sangrador, Gavin Shaddick, H. Ross Anderson, Theo Vos, Mohammad H. Forouzanfar, Richard T. Burnett, and Aaron Cohen. Ambient air pollution exposure estimation for the global burden of disease 2013. *Environmental Science & Technology*, 50(1):79–88, 2016. ISSN 0013-936X. doi: 10.1021/acs.est.5b03709. URL `http://pubs.acs.org/doi/10.1021/acs.est.5b03709`.

Patricia Brewer, Gail Tonnesen, Ralph Morris, Tom Moore, Uarporn Nopmongcol, and Debra Miller. Air pollutant source characterization using the revised regional haze tracking metric and a photochemical grid model and implications for regional haze planning. *Journal of the Air & Waste Management Association*, 69(3):373–390, 2019. doi: 10.1080/10962247.2018.1537985. URL `https://doi.org/10.1080/10962247.2018.1537985`. PMID: 30339494.

C. A. Brock, C. Williamson, A. Kupc, K. D. Froyd, F. Erdesz, N. Wagner, M. Richardson, J. P. Schwarz, R.-S. Gao, J. M. Katich, P. Campuzano-Jost, B. A. Nault, J. C. Schroder, J. L. Jimenez, B. Weinzierl, M. Dollner, T. Bui, and D. M. Murphy. Aerosol size distributions during the atmospheric tomography mission (atom): methods, uncertainties, and data products. *Atmospheric Measurement Techniques*, 12(6):3081–3099, 2019. doi: 10.5194/amt-12-3081-2019. URL `https://www.atmos-meas-tech.net/12/3081/2019/`.

R T Burnett, C A Pope III, M Ezzati, C Olives, S S Lim, S Mehta, H H Shin, G Singh, B Hubbell, M Brauer, H R Anderson, K R Smith, J R Balmes, N G

Bruce, H Kan, F Laden, A Pruess-Ustuen, M C Turner, S M Gapstur, W R Diver, and A Cohen. An Integrated Risk Function for Estimating the Global Burden of Disease Attributable to Ambient Fine Particulate Matter Exposure. *Environmental Health Perspectives*, 122(4):397–403, 2014. ISSN ISSN 0091-6765 EISSN 1552-9924. doi: 10.1289/ehp.1307049. URL http://dx.doi.org/10.1289/ehp.1307049.

Richard Burnett, Hong Chen, Mieczysław Szyszkowicz, Neal Fann, Bryan Hubbell, C. Arden Pope, Joshua S. Apte, Michael Brauer, Aaron Cohen, Scott Weichenthal, Jay Coggins, Qian Di, Bert Brunekreef, Joseph Frostad, Stephen S. Lim, Haidong Kan, Katherine D. Walker, George D. Thurston, Richard B. Hayes, Chris C. Lim, Michelle C. Turner, Michael Jerrett, Daniel Krewski, Susan M. Gapstur, W. Ryan Diver, Bart Ostro, Debbie Goldberg, Daniel L. Crouse, Randall V. Martin, Paul Peters, Lauren Pinault, Michael Tjepkema, Aaron van Donkelaar, Paul J. Villeneuve, Anthony B. Miller, Peng Yin, Maigeng Zhou, Lijun Wang, Nicole A. H. Janssen, Marten Marra, Richard W. Atkinson, Hilda Tsang, Thuan Quoc Thach, John B. Cannon, Ryan T. Allen, Jaime E. Hart, Francine Laden, Giulia Cesaroni, Francesco Forastiere, Gudrun Weinmayr, Andrea Jaensch, Gabriele Nagel, Hans Concin, and Joseph V. Spadaro. Global estimates of mortality associated with long-term exposure to outdoor fine particulate matter. *Proceedings of the National Academy of Sciences*, 115(38):9592–9597, 2018. ISSN 0027-8424. doi: 10.1073/pnas.1803222115. URL https://www.pnas.org/content/115/38/9592.

S P Burton, R A Ferrare, M A Vaughan, A H Omar, R R Rogers, C A Hostetler, and J W Hair. Aerosol classification from airborne HSRL and comparisons with the CALIPSO vertical feature mask. *Atmospheric Measurement Techniques*, 6(5): 1397–1412, 2013. ISSN 1867-1381. doi: 10.5194/amt-6-1397-2013.

Center for International Earth Science Information Network. Gridded population of the world, version 4 (gpwv4): Population density, revision 11, 2018.

Sreelekha Chaliyakunnel, Dylan B. Millet, and Xin Chen. Constraining emissions of volatile organic compounds over the indian subcontinent using space-based formaldehyde measurements. *Journal of Geophysical Research: Atmospheres*, 124 (19):10525–10545, 2019. doi: 10.1029/2019JD031262. URL https://agupubs.onlinelibrary.wiley.com/doi/abs/10.1029/2019JD031262.

Kenneth Chay, Carlos Dobkin, and Michael Greenstone. The clean air act of 1970 and adult mortality. *Journal of Risk and Uncertainty*, 27(3):279–300, 2003.

B Chen, J Huang, P Minnis, Y Hu, Y Yi, Z Liu, D Zhang, and X Wang. Detection of dust aerosol by combining CALIPSO active lidar and passive IIR measurements. *Atmospheric Chemistry and Physics*, 10(9):4241–4251, 2010. ISSN 1680-7316. doi: 10.5194/acp-10-4241-2010.

D. Chen, Y. Wang, M. B. McElroy, K. He, R. M. Yantosca, and P. Le Sager. Regional co pollution and export in china simulated by the high-resolution nested-grid geos-chem model. *Atmospheric Chemistry and Physics*, 9(11):3825–3839,

2009. doi: 10.5194/acp-9-3825-2009. URL https://www.atmos-chem-phys.net/9/3825/2009/.

H Chen, M S Goldberg, and P J Villeneuve. A systematic review of the relation between long-term exposure to ambient air pollution and chronic diseases. *Reviews on Environmental Health*, 23(4):243–297, 2008. ISSN 0048-7554; 0048-7554. doi: 10.1515/reveh.2008.23.4.24.

L Clarisse, P F. Coheur, N Theys, D Hurtmans, and C Clerbaux. The 2011 Nabro eruption, a SO2 plume height analysis using IASI measurements. *Atmospheric Chemistry and Physics*, 14(6):3095–3111, 2014. ISSN 1680-7316. doi: 10.5194/acp-14-3095-2014.

Daniel S. Cohan and Sergey L. Napelenok. Air quality response modeling for decision support. *Atmosphere*, 2(3):407–425, 2011. doi: 10.3390/atmos2030407. URL http://www.mdpi.com/2073-4433/2/3/407.

Aaron J Cohen, Michael Brauer, Richard Burnett, H Ross Anderson, Joseph Frostad, Kara Estep, Kalpana Balakrishnan, Bert Brunekreef, Lidia Morawska, C Arden Pope Iii, Hwashin Shin, Kurt Straif, Gavin Shaddick, Matthew Thomas, Rita Van Dingenen, Aaron Van Donkelaar, Theo Vos, Christopher J L Murray, and Mohammad H Forouzanfar. Estimates and 25-year trends of the global burden of disease attributable to ambient air pollution : an analysis of data from the Global Burden of Diseases Study 2015. *The Lancet*, 389(10082):1907–1918, 2015. ISSN 0140-6736. doi: 10.1016/S0140-6736(17)30505-6. URL http://dx.doi.org/10.1016/S0140-6736(17)30505-6.

A W Correia, C A Pope 3rd, D W Dockery, Y Wang, M Ezzati, and F Dominici. Effect of air pollution control on life expectancy in the United States: an analysis of 545 U.S. counties for the period from 2000 to 2007. *Epidemiology*, 24(1):23–31, 2013. ISSN 1044-3983. doi: 10.1097/EDE.0b013e3182770237. URL http://www.ncbi.nlm.nih.gov/pubmed/23211349.

Louis Anthony Tony Cox. Reassessing the Human Health Benefits from Cleaner Air. *Risk Analysis*, 32(5):816–829, 2012. ISSN 02724332. doi: 10.1111/j.1539-6924.2011.01698.x.

Louis Anthony (Tony) Cox. Effects of exposure estimation errors on estimated exposure-respose relations for pm2.5. *Environmental Research*, pages 636–646, 2018. doi: 10.1016/j.envres.2018.03.038.

M. Crippa, D. Guizzardi, M. Muntean, E. Schaaf, F. Dentener, J. A. van Aardenne, S. Monni, U. Doering, J. G. J. Olivier, V. Pagliari, and G. Janssens-Maenhout. Gridded emissions of air pollutants for the period 1970–2012 within edgar v4.3.2. *Earth System Science Data*, 10(4):1987–2013, 2018. doi: 10.5194/essd-10-1987-2018. URL https://www.earth-syst-sci-data.net/10/1987/2018/.

Dan L. Crouse, Paul A. Peters, Aaron van Donkelaar, Mark S. Goldberg, Paul J. Villeneuve, Orly Brion, Saeeda Khan, Dominic Odwa Atari, Michael Jerrett, III Pope C.Arden, Michael Brauer, Jeffrey R. Brook, Randall V. Martin, David Stieb, and Richard T. Burnett. Risk of non accidental and cardiovascular mortality in relation to long-term exposure to low concentrations of fine particulate matter: A canadian national-level cohort study. *Environ Health Persp*, 120(5):708–714, May 2012. doi: 10.1289/ehp.1104049.

Dan L. Crouse, Paul A. Peters, Perry Hystad, Jeffrey R. Brook, Aaron van Donkelaar, Randall V. Martin, Paul J. Villeneuve, Michael Jerrett, Mark S. Goldberg, C. Arden Pope, Michael Brauer, Robert D. Brook, Alain Robichaud, Richard Menard, and Richard T. Burnett. Ambient PM2.5, O3, and NO2 exposures and associations with mortality over 16 years of follow-up in the canadian census health and environment cohort (CanCHEC). *Environmental Health Perspectives*, 123(11):1180–1186, 2015. ISSN 15529924. doi: 10.1289/ehp.1409276.

Valeriu Damian, Adrian Sandu, Mirela Damian, Florian Potra, and Gregory R. Carmichael. The kinetic preprocessor KPP - A software environment for solving chemical kinetics. *Computers and Chemical Engineering*, 2002. ISSN 00981354. doi: 10.1016/S0098-1354(02)00128-X.

Qian Di, Itai Kloog, Petros Koutrakis, Alexei Lyapustin, Yujie Wang, and Joel Schwartz. Assessing PM2.5 Exposures with High Spatiotemporal Resolution across the Continental United States. *Environmental Science and Technology*, 50(9):4712–4721, 2016. ISSN 15205851. doi: 10.1021/acs.est.5b06121.

Douglas W. Dockery, C. Arden Pope, Xiping Xu, John D. Spengler, James H. Ware, Martha E. Fay, Benjamin G. Ferris, and Frank E. Speizer. An association between air pollution and mortality in six u.s. cities. *New England Journal of Medicine*, 329 (24):1753–1759, 1993. doi: 10.1056/NEJM199312093292401. URL `https://doi.org/10.1056/NEJM199312093292401`. PMID: 8179653.

John Duchi, Elad Hazan, and Yoram Singer. Adaptive subgradient methods for online learning and stochastic optimization. *J. Mach. Learn. Res.*, 12(null):2121–2159, July 2011. ISSN 1532-4435.

Steven J. Dutton, James J. Schauer, Sverre Vedal, and Michael P. Hannigan. Pm2.5 characterization for time series studies: Pointwise uncertainty estimation and bulk speciation methods applied in denver. *Atmospheric Environment*, 43(5):1136 – 1146, 2009. ISSN 1352-2310. doi: https://doi.org/10.1016/j.atmosenv.2008.10.003. URL `http://www.sciencedirect.com/science/article/pii/S1352231008009539`. Air Pollution Related to Transport.

S. D. Eastham, M. S. Long, C. A. Keller, E. Lundgren, R. M. Yantosca, J. Zhuang, C. Li, C. J. Lee, M. Yannetti, B. M. Auer, T. L. Clune, J. Kouatchou, W. M. Putman, M. A. Thompson, A. L. Trayanov, A. M. Molod, R. V. Martin, and D. J.

Jacob. Geos-chem high performance (gchp v11-02c): a next-generation implementation of the geos-chem chemical transport model for massively parallel applications. *Geoscientific Model Development*, 11(7):2941–2953, 2018. doi: 10.5194/gmd-11-2941-2018. URL https://www.geosci-model-dev.net/11/2941/2018/.

Dimitris Evangelopoulos, Klea Katsouyanni, Ruth H. Keogh, Evangelia Samoli, Joel Schwartz, Ben Barratt, Hanbin Zhang, and Heather Walton. PM2.5 and NO2 exposure errors using proxy measures, including derived personal exposure from outdoor sources: A systematic review and meta-analysis. *Environment International*, 137, APR 2020. ISSN 0160-4120. doi: {10.1016/j.envint.2020.105500}.

M J Evans. Impact of new laboratory studies of N 2 O 5 hydrolysis on global model budgets of tropospheric nitrogen oxides, ozone, and OH. *Geophysical Research Letters*, 32(9):L09813, 2005. ISSN 0094-8276. doi: 10.1029/2005GL022469. URL http://doi.wiley.com/10.1029/2005GL022469.

T Duncan. Fairlie, Daniel J Jacob, and Rokjin J Park. The impact of transpacific transport of mineral dust in the United States. *Atmospheric Environment*, 41(6): 1251–1266, feb 2007. ISSN 13522310. doi: 10.1016/j.atmosenv.2006.09.048. URL http://linkinghub.elsevier.com/retrieve/pii/S1352231006009915.

Neal Fann, Charles M. Fulcher, and Bryan J. Hubbell. The influence of location, source, and emission type in estimates of the human health benefits of reducing a ton of air pollution. *Air Quality, Atmosphere and Health*, 2(3):169–176, 2009. ISSN 18739318. doi: 10.1007/s11869-009-0044-0.

M. C. S. Ferreira, B. Furieri, A. Ould El Moctar, J.-L. Harion, A. Valance, P. Dupont, N. C. Reis, and J. M. Santos. A simple model to estimate emission of wind-blown particles from a granular bed in comparison to wind tunnel experiments. *Geomorphology*, 335:1–13, June 2019. ISSN 0169-555X. URL http://www.sciencedirect.com/science/article/pii/S0169555X1930090X.

Center for International Earth Science Information Network (CIESIN) and Centro Internacional de Agricultura Tropical (CIAT). Gridded population of the world, version 3 (gpwv3): Population count grid, future estimates. Technical report, CIESIN, Columbia University, 2005. URL http://sedac.ciesin.columbia.edu/data/set/gpw-v3-population-count-future-estimates.

B. Ford and C. L. Heald. Aerosol loading in the Southeastern United States: reconciling surface and satellite observations. *Atmospheric Chemistry and Physics*, 13 (18):9269–9283, sep 2013. ISSN 1680-7324. doi: 10.5194/acp-13-9269-2013. URL http://www.atmos-chem-phys.net/13/9269/2013/.

Bonne Ford and Colette L. Heald. An A-train and model perspective on the vertical distribution of aerosols and CO in the Northern Hemisphere. *Journal of Geophysical Research: Atmospheres*, 117(6):1–23, mar 2012. ISSN 2169-897X. doi: 10.1029/2011JD016977.

C. Fountoukis and A. Nenes. Isorropia ii: a computationally efficient thermodynamic equilibrium model for k^+–ca^{2+}–mg^{2+}–nh_4^+–na^+–so_4^{2-}–no_3^-–cl^-–h_2o aerosols. *Atmospheric Chemistry and Physics*, 7(17):4639–4659, 2007. doi: 10.5194/acp-7-4639-2007. URL https://www.atmos-chem-phys.net/7/4639/2007/.

Meredith Franklin, Olga Kalashnikova, Michael Garay, and Scott Fruin. Characterization of subgrid-scale variability in particulate matter with respect to satellite aerosol observations. *Remote Sensing*, 10:623, 04 2018. doi: 10.3390/rs10040623.

Mark A. Friedl, Damien Sulla-Menashe, Bin Tan, Annemarie Schneider, Navin Ramankutty, Adam Sibley, and Xiaoman Huang. Modis collection 5 global land cover: Algorithm refinements and characterization of new datasets. *Remote Sensing of Environment*, 114(1):168 – 182, 2010. ISSN 0034-4257. doi: https://doi.org/10.1016/j.rse.2009.08.016. URL http://www.sciencedirect.com/science/article/pii/S0034425709002673.

James N. Galloway, Alan R. Townsend, Jan Willem Erisman, Mateete Bekunda, Zucong Cai, John R. Freney, Luiz A. Martinelli, Sybil P. Seitzinger, and Mark A. Sutton. Transformation of the nitrogen cycle: Recent trends, questions, and potential solutions. *Science*, 320(5878):889–892, 2008. doi: 10.1126/science.1136674. URL http://www.sciencemag.org/content/320/5878/889.abstract. http://www.sciencemag.org/content/320/5878/889.full.pdf.

M. J. Garay, M. L. Witek, R. A. Kahn, F. C. Seidel, J. A. Limbacher, M. A. Bull, D. J. Diner, E. G. Hansen, O. V. Kalashnikova, H. Lee, A. M. Nastan, and Y. Yu. Introducing the 4.4 km spatial resolution multi-angle imaging spectroradiometer (misr) aerosol product. *Atmospheric Measurement Techniques*, 13(2):593–628, 2020. doi: 10.5194/amt-13-593-2020. URL https://www.atmos-meas-tech.net/13/593/2020/.

Ritesh Gautam, N Christina Hsu, Thomas F Eck, Brent N Holben, Serm Janjai, Treenuch Jantarach, Si-Chee Tsay, and William K Lau. Characterization of aerosols over the Indochina peninsula from satellite-surface observations during biomass burning pre-monsoon season. *Atmospheric Environment*, 78(SI):51–59, oct 2013. ISSN 1352-2310. doi: 10.1016/j.atmosenv.2012.05.038.

GBD 2017 Mortality Collaborators. Gloal, regional, and national age-sex-specific mortality and life expectancy, 1950-2017: a systematic analysis for the global burden of disease study 2017. *The Lancet*, 392:1684–1735, 2018. doi: 10.1016/S0140-6736(18)31891-9.

GBD 2017 Risk Factor Collaborators. Global, regional, and national comparative risk assessment of 84 behavioural, environmental and occupational, ad metabolic risks or clusters of risks for 195 countries and territories, 1990-2017: a systematic analysis for the global burden of disease stud. *The Lancet*, 392:1923–94, 2018. doi: 10.1016/S0140-6736(18)32225-6.

Guannan Geng, Qiang Zhang, Randall V Martin, Aaron van Donkelaar, Hong Huo, Huizheng Che, Jintai Lin, and Kebin He. Estimating long-term PM2.5 concentrations in China using satellite-based aerosol optical depth and a chemical transport model. *Remote Sensing of Environment*, 166:262–270, sep 2015. ISSN 00344257. doi: 10.1016/j.rse.2015.05.016. URL `http://linkinghub.elsevier.com/retrieve/pii/S0034425715300171`.

Brian J Getzewich, Jason L Tackett, Jay Kar, Anne Garnier, Mark A Vaughan, and Bill Hunt. CALIOP CALIBRATION: VERSION 4.0 ALGORITHM UPDATES. In B Gross, F Moshary, and M Arend, editors, *27TH INTERNATIONAL LASER RADAR CONFERENCE (ILRC 27)*, volume 119 of *EPJ Web of Conferences*, 17 AVE DU HOGGAR PARC D ACTIVITES COUTABOEUF BP 112, F-91944 CEDEX A, FRANCE, 2016. City Univ New York, City Coll, E D P SCIENCES. doi: 10.1051/epjconf/201611904013.

D. M. Giles, A. Sinyuk, M. G. Sorokin, J. S. Schafer, A. Smirnov, I. Slutsker, T. F. Eck, B. N. Holben, J. R. Lewis, J. R. Campbell, E. J. Welton, S. V. Korkin, and A. I. Lyapustin. Advancements in the aerosol robotic network (aeronet) version 3 database – automated near-real-time quality control algorithm with improved cloud screening for sun photometer aerosol optical depth (aod) measurements. *Atmospheric Measurement Techniques*, 12(1):169–209, 2019. doi: 10.5194/amt-12-169-2019. URL `https://www.atmos-meas-tech.net/12/169/2019/`.

Marianne Glasius and Allen H. Goldstein. Recent discoveries and future challenges in atmospheric organic chemistry. *Environmental Science & Technology*, 50(6):2754–2764, 2016. doi: 10.1021/acs.est.5b05105. URL `https://doi.org/10.1021/acs.est.5b05105`. PMID: 26862779.

S. L. Gong. A parameterization of sea-salt aerosol source function for sub- and super-micron particles. *Global Biogeochemical Cycles*, 17(4):n/a–n/a, dec 2003. ISSN 08866236. doi: 10.1029/2003GB002079. URL `http://doi.wiley.com/10.1029/2003GB002079`.

Nancy B. Grimm, Stanley H. Faeth, Nancy E. Golubiewski, Charles L. Redman, Jianguo Wu, Xuemei Bai, and John M. Briggs. Global change and the ecology of cities. *Science*, 319(5864):756–760, 2008. doi: 10.1126/science.1150195. URL `http://www.sciencemag.org/content/319/5864/756.abstract`. http://www.sciencemag.org/content/319/5864/756.full.pdf.

H. Grythe, J. Ström, R. Krejci, P. Quinn, and A. Stohl. A review of sea-spray aerosol source functions using a large global set of sea salt aerosol concentration measurements. *Atmospheric Chemistry and Physics*, 14(3):1277–1297, feb 2014. ISSN 1680-7324. doi: 10.5194/acp-14-1277-2014. URL `http://www.atmos-chem-phys.net/14/1277/2014/`.

Melanie S Hammer, Aaron van Donkelaar, Chi Li, Alexei Lyapustin, Andrew M Sayer, N Christina Hsu, Robert C Levy, Michael Garay, Olga Kalashnikova, Ralph A.

Kahn, Michael Brauer, Joshua Schulz Apte, Daven K. Henze, Li Zhang, Qiang Zhang, Bonne Ford, Jeffrey R. Pierce, and Randall V Martin. Global estimates and long-term trends of fine particulate matter concentrations (1998-2018). *Environmental Science & Technology*, 0(ja):null, 2020. doi: 10.1021/acs.est.0c01764. URL https://doi.org/10.1021/acs.est.0c01764. PMID: 32491847.

Mathew R Heal, Prashant Kumar, and Roy M Harrison. Particles, air quality, policy and health. *Chemical Society Reviews*, 41(19):6606–6630, 2012. ISSN 0306-0012. doi: 10.1039/c2cs35076a. URL http://dx.doi.org/10.1039/c2cs35076a.

D. K. Henze, A. Hakami, and J. H. Seinfeld. Development of the adjoint of geos-chem. *Atmospheric Chemistry and Physics*, 7:2413–2433, 2007.

D. K. Henze, J. H. Seinfeld, and D. T. Shindell. Inverse modeling and mapping us air quality influences of inorganic pm2.5 precursor emissions using the adjoint of geos-chem. *Atmospheric Chemistry and Physics*, 9(16):5877–5903, 2009. Review.

B.N. Holben, T.F. Eck, I. Slutsker, D. Tanré, J.P. Buis, A. Setzer, E. Vermote, J.A. Reagan, Y.J. Kaufman, T. Nakajima, F. Lavenu, I. Jankowiak, and A. Smirnov. AERONET—A Federated Instrument Network and Data Archive for Aerosol Characterization. *Remote Sensing of Environment*, 66(1):1–16, oct 1998. ISSN 00344257. doi: 10.1016/S0034-4257(98)00031-5. URL http://linkinghub.elsevier.com/retrieve/pii/S0034425798000315.

Hannah M. Horowitz, Christopher Holmes, Alicia Wright, Tomás Sherwen, Xuan Wang, Mat Evans, Jiayue Huang, Lyatt Jaeglé, Qianjie Chen, Shuting Zhai, and Becky Alexander. Effects of sea salt aerosol emissions for marine cloud brightening on atmospheric chemistry: Implications for radiative forcing. *Geophysical Research Letters*, 47(4):e2019GL085838, 2020. doi: 10.1029/2019GL085838. URL https://agupubs.onlinelibrary.wiley.com/doi/abs/10.1029/2019GL085838. e2019GL085838 2019GL085838.

Q. Hou, X. Q. An, Y. Wang, and J. P. Guo. An evaluation of resident exposure to respirable particulate matter and health economic loss in beijing during beijing 2008 olympic games. *Science of the Total Environment*, 408(19):4026–4032, SEP 1 2010. doi: 10.1016/j.scitotenv.2009.12.030. Article.

N. C. Hsu, M.-J. Jeong, C. Bettenhausen, A. M. Sayer, R. Hansell, C. S. Seftor, J. Huang, and S.-C. Tsay. Enhanced deep blue aerosol retrieval algorithm: The second generation. *Journal of Geophysical Research: Atmospheres*, 118(16):9296–9315, 2013. doi: 10.1002/jgrd.50712. URL https://agupubs.onlinelibrary.wiley.com/doi/abs/10.1002/jgrd.50712.

D Jacob. Heterogeneous chemistry and tropospheric ozone. *Atmospheric Environment*, 34(12-14):2131–2159, 2000. ISSN 13522310. doi: 10.1016/S1352-2310(99)00462-8. URL http://linkinghub.elsevier.com/retrieve/pii/S1352231099004628.

L. Jaeglé, P. K. Quinn, T. S. Bates, B. Alexander, and J. T. Lin. Global distribution of sea salt aerosols: New constraints from in situ and remote sensing observations. *Atmospheric Chemistry and Physics*, 11(7):3137–3157, apr 2011. ISSN 16807316. doi: 10.5194/acp-11-3137-2011. URL `http://www.atmos-chem-phys.net/11/3137/2011/`.

M Jerrett, R T Burnett, R J Ma, C A Pope, D Krewski, K B Newbold, G Thurston, Y L Shi, N Finkelstein, E E Calle, and M J Thun. Spatial analysis of air pollution and mortality in Los Angeles. *Epidemiology*, 16(6):727–736, nov 2005. ISSN 1044-3983. doi: 10.1097/01.ede.0000181630.15826.7d.

Z Jiang, D B A Jones, J Worden, H M Worden, D K Henze, and Y X Wang. Regional data assimilation of multi-spectral MOPITT observations of CO over North America. *Atmospheric Chemistry and Physics*, 15(12):6801–6814, 2015. ISSN 1680-7316. doi: 10.5194/acp-15-6801-2015.

Tingting Ju, Xiaolan Li, Hongsheng Zhang, Xuhui Cai, and Yu Song. Comparison of two different dust emission mechanisms over the horqin sandy land area: Aerosols contribution and size distributions. *Atmospheric Environment*, 176:82 – 90, 2018. ISSN 1352-2310. doi: https://doi.org/10.1016/j.atmosenv.2017.12.017. URL `http://www.sciencedirect.com/science/article/pii/S1352231017308580`.

M. Kacenelenbogen, M. A. Vaughan, J. Redemann, R. M. Hoff, R. R. Rogers, R. A. Ferrare, P. B. Russell, C. A. Hostetler, J. W. Hair, and B. N. Holben. An accuracy assessment of the CALIOP/CALIPSO version 2/version 3 daytime aerosol extinction product based on a detailed multi-sensor, multi-platform case study. *Atmospheric Chemistry and Physics*, 11(8):3981–4000, 2011. ISSN 1680-7316. doi: 10.5194/acp-11-3981-2011.

M Kacenelenbogen, J Redemann, M A Vaughan, A H Omar, P B Russell, S Burton, R R Rogers, R A Ferrare, and C A Hostetler. An evaluation of CALIOP/CALIPSO's aerosol-above-cloud detection and retrieval capability over North America. *Journal of Geophysical Research: Atmospheres*, 119(1):230–244, jan 2014. ISSN 2169-897X. doi: 10.1002/2013JD020178.

O. V. Kalashnikova, M. J. Garay, J. V. Martonchik, and D. J. Diner. Misr dark water aerosol retrievals: operational algorithm sensitivity to particle nonsphericity. *Atmospheric Measurement Techniques*, 6(8):2131–2154, 2013. doi: 10.5194/amt-6-2131-2013. URL `https://www.atmos-meas-tech.net/6/2131/2013/`.

Eugenia Kalnay. *Atmospheric Modeling, Data Assimilation and Predictability*. Cambridge University Press, New York, NY, 2003. ISBN 0 521 79629 6.

T. Kanitz, A. Ansmann, A. Foth, P. Seifert, U. Wandinger, R. Engelmann, H. Baars, D. Althausen, C. Casiccia, and F. Zamorano. Surface matters: limitations of

CALIPSO V3 aerosol typing in coastal regions. *Atmospheric Measurement Techniques*, 7(7):2061–2072, 2014. ISSN 1867-1381. doi: 10.5194/amt-7-2061-2014.

Frank J. Kelly and Julia C. Fussell. Size, source and chemical composition as determinants of toxicity attributable to ambient particulate matter. *Atmospheric Environment*, 60:504–526, DEC 2012. doi: 10.1016/j.atmosenv.2012.06.039. Review.

Jafar A. Khan, Stefan Van Aelst, and Ruben H. Zamar. Building a robust linear model with forward selection and stepwise procedures. *Computational Statistics & Data Analysis*, 52:239–248, 2017. doi: 10.1016/j.csda.2007.01.007.

Man-Hae Kim, Ali H Omar, Mark A Vaughan, David M Winker, Charles R Trepte, Yongxiang Hu, Zhaoyan Liu, and Sang-Woo Kim. Quantifying the low bias of CALIPSO's column aerosol optical depth due to undetected aerosol layers. *Journal of Geophysical Research: Atmospheres*, 122(2):1098–1113, jan 2017. ISSN 2169-897X. doi: 10.1002/2016JD025797.

P. S. Kim, D. J. Jacob, J. A. Fisher, K. Travis, K. Yu, L. Zhu, R. M. Yantosca, M. P. Sulprizio, J. L. Jimenez, P. Campuzano-Jost, K. D. Froyd, J. Liao, J. W. Hair, M. A. Fenn, C. F. Butler, N. L. Wagner, T. D. Gordon, A. Welti, P. O. Wennberg, J. D. Crounse, J. M. St. Clair, A. P. Teng, D. B. Millet, J. P. Schwarz, M. Z. Markovic, and A. E. Perring. Sources, seasonality, and trends of southeast US aerosol: An integrated analysis of surface, aircraft, and satellite observations with the GEOS-Chem chemical transport model. *Atmospheric Chemistry and Physics*, 15(18):10411–10433, 2015. ISSN 16807324. doi: 10.5194/acp-15-10411-2015.

S W Kim, S Berthier, J C. Raut, P Chazette, F Dulac, and S C. Yoon. Validation of aerosol and cloud layer structures from the space-borne lidar CALIOP using a ground-based lidar in Seoul, Korea. *Atmospheric Chemistry and Physics*, 8(13): 3705–3720, 2008. ISSN 1680-7316.

C Kittaka, D M Winker, M A Vaughan, A Omar, and L A Remer. Intercomparison of column aerosol optical depths from CALIPSO and MODIS-Aqua. *Atmospheric Measurement Techniques*, 4(2):131–141, 2011. ISSN 1867-1381. doi: 10.5194/amt-4-131-2011.

Z. Klimont, S. J. Smith, and J. Cofala. The last decade of global anthropogenic sulfur dioxide: 2000-2011 emissions. *Environmental Research Letters*, 8(1):014003, 2013. doi: 10.1088/1748-9326/8/1/014003. URL `http://stacks.iop.org/1748-9326/8/i=1/a=014003`.

J. K. Kodros, E. Carter, M. Brauer, J. Volckens, K. R. Bilsback, C. L'Orange, M. Johnson, and J. R. Pierce. Quantifying the Contribution to Uncertainty in Mortality Attributed to Household, Ambient, and Joint Exposure to PM2.5 From Residential Solid Fuel Use. *Geohealth*, 2(1):25–39, 2018. ISSN 2471-1403. doi: 10.1002/2017GH000115. URL `https://doi.org/10.1002/2017GH000115`.

Brigitte Koffi, Michael Schulz, Francois-Marie Breon, Jan Griesfeller, David Winker, Yves Balkanski, Susanne Bauer, Terje Berntsen, Mian Chin, William D Collins, Frank Dentener, Thomas Diehl, Richard Easter, Steven Ghan, Paul Ginoux, Sunling Gong, Larry W Horowitz, Trond Iversen, Alf Kirkevag, Dorothy Koch, Maarten Krol, Gunnar Myhre, Philip Stier, and Toshihiko Takemura. Application of the CALIOP layer product to evaluate the vertical distribution of aerosols estimated by global models: AeroCom phase I results. *Journal of Geophysical Research: Atmospheres*, 117, may 2012. ISSN 2169-897X. doi: 10.1029/2011JD016858.

Brigitte Koffi, Michael Schulz, Francois-Marie Breon, Frank Dentener, Birthe Marie Steensen, Jan Griesfeller, David Winker, Yves Balkanski, Susanne E Bauer, Nicolas Bellouin, Terje Berntsen, Huisheng Bian, Mian Chin, Thomas Diehl, Richard Easter, Steven Ghan, Didier A Hauglustaine, Trond Iversen, Alf Kirkevag, Xiaohong Liu, Ulrike Lohmann, Gunnar Myhre, Phil Rasch, Oyvind Seland, Ragnhild B Skeie, Stephen D Steenrod, Philip Stier, Jason Tackett, Toshihiko Takemura, Kostas Tsigaridis, Maria Raffaella Vuolo, Jinho Yoon, and Kai Zhang. Evaluation of the aerosol vertical distribution in global aerosol models through comparison against CALIOP measurements: AeroCom phase II results. *Journal of Geophysical Research: Atmospheres*, 121(12):7254–7283, jun 2016. ISSN 2169-897X. doi: 10.1002/2015JD024639.

Jamin Koo, Qiqi Wang, Daven K. Henze, Ian A. Waitz, and Steven R H Barrett. Spatial sensitivities of human health risk to intercontinental and high-altitude pollution. *Atmospheric Environment*, 71(x):140–147, 2013. ISSN 13522310. doi: 10.1016/j.atmosenv.2013.01.025. URL `http://dx.doi.org/10.1016/j.atmosenv.2013.01.025`.

Daniel Krewski, Michael Jerrett, Richard T Burnett, Renjun Ma, Edward Hughes, Yuanli Shi, Michelle C Turner, C Arden Pope, George Thurston, Eugenia E Calle, Michael J Thun, Bernie Beckerman, Pat DeLuca, Norm Finkelstein, Kaz Ito, D K Moore, K Bruce Newbold, Tim Ramsay, Zev Ross, Hwashin Shin, and Barbara Tempalski. Extended follow-up and spatial analysis of the American Cancer Society study linking particulate air pollution and mortality. *Research Report (Health Effects Institute)*, (140):5–114; discussion 115–136, 2009. ISSN 1041-5505.

A. Krupnick and R. Morgenstern. The future of benefit-cost analyses of the clean air act. *Annual Review of Public Health*, 23:427–448, 2002. doi: 10.1146/annurev.publhealth.23.100901.140516. Review.

J. Kurokawa, T. Ohara, T. Morikawa, S. Hanayama, G. Janssens-Maenhout, T. Fukui, K. Kawashima, and H. Akimoto. Emissions of air pollutants and greenhouse gases over Asian regions during 2000-2008: Regional Emission inventory in ASia (REAS) version 2. *Atmospheric Chemistry and Physics*, 13(21):11019–11058, 2013. ISSN 16807316. doi: 10.5194/acp-13-11019-2013.

Forrest G Lacey, Daven K Henze, Colin J Lee, Aaron van Donkelaar, and Randall V Martin. Transient climate and ambient health impacts due to national solid fuel

cookstove emissions. *Proceedings of the National Academy of Sciences*, 2017. ISSN 0027-8424. doi: 10.1073/pnas.1612430114. URL http://www.pnas.org/content/early/2017/01/17/1612430114.abstract.

John Latham, Keith Bower, Tom Choularton, Hugh Coe, Paul Connolly, Gary Cooper, Tim Craft, Jack Foster, Alan Gadian, Lee Galbraith, Hector Iacovides, David Johnston, Brian Launder, Brian Leslie, John Meyer, Armand Neukermans, Bob Ormond, Ben Parkes, Phillip Rasch, John Rush, Stephen Salter, Tom Stevenson, Hailong Wang, Qin Wang, and Rob Wood. Marine cloud brightening. *Philosophical Transactions of the Royal Society A: Mathematical, Physical and Engineering Sciences*, 370(1974):4217–4262, 2012. doi: 10.1098/rsta.2012.0086. URL https://royalsocietypublishing.org/doi/abs/10.1098/rsta.2012.0086.

C.J. Lee, R.V. Martin, D.K. Henze, M. Brauer, A. Cohen, and A.V. Donkelaar. Response of global particulate-matter-related mortality to changes in local precursor emissions. *Environmental Science and Technology*, 49(7), 2015. ISSN 15205851. doi: 10.1021/acs.est.5b00873.

R. C. Levy, S. Mattoo, L. A. Munchak, L. A. Remer, A. M. Sayer, F. Patadia, and N. C. Hsu. The collection 6 modis aerosol products over land and ocean. *Atmospheric Measurement Techniques*, 6(11):2989–3034, 2013. doi: 10.5194/amt-6-2989-2013. URL https://www.atmos-meas-tech.net/6/2989/2013/.

Ernie R. Lewis and Stephen E. Scwartz. *Sea Salt Aerosol Production: Mechanisms, Methods, Measurements and Models*. The American Geophysical Union, 2004. ISBN 087590-417-3. doi: 10.1029/GM152.

Chi Li, Randall V. Martin, Aaron van Donkelaar, Brian Boys, Melanie Hammer, Jun-Wei Xu, Eloise Marais, Adam Reff, Madeleine Strum, David A. Ridley, Monica Crippa, Michael Brauer, and Qiang Zhang. Trends in chemical composition of global and regional population-weighted fine particulate matter estimated for 25 years. *Environmental Science and Technology*, 51:11185–11195, 2017. doi: 10.1021/acs.est.7b02530.

Yi Li, Wen Wang, Haidong Kan, Xiaohui Xu, and Bingheng Chen. Air quality and outpatient visits for asthma in adults during the 2008 summer olympic games in beijing. *Science of the Total Environment*, 408(5):1226–1227, FEB 1 2010. doi: 10.1016/j.scitotenv.2009.11.035. Article.

Stephen S. Lim, Theo Vos, Abraham D. Flaxman, Goodarz Danaei, Kenji Shibuya, Heather Adair-Rohani, Markus Amann, H. Ross Anderson, Kathryn G. Andrews, Martin Aryee, Charles Atkinson, Loraine J. Bacchus, Adil N. Bahalim, Kalpana Balakrishnan, John Balmes, Suzanne Barker-Collo, Amanda Baxter, Michelle L. Bell, Jed D. Blore, Fiona Blyth, Carissa Bonner, Guilherme Borges, Rupert Bourne, Michel Boussinesq, Michael Brauer, Peter Brooks, Nigel G. Bruce, Bert Brunekreef, Claire Bryan-Hancock, Chiara Bucello, Rachelle Buchbinder, Fiona

Bull, Richard T. Burnett, Tim E. Byers, Bianca Calabria, Jonathan Carapetis, Emily Carnahan, Zoe Chafe, Fiona Charlson, Honglei Chen, Jian Shen Chen, Andrew Tai Ann Cheng, Jennifer Christine Child, Aaron Cohen, K. Ellicott Colson, Benjamin C. Cowie, Sarah Darby, Susan Darling, Adrian Davis, Louisa Degenhardt, Frank Dentener, Don C. Des Jarlais, Karen Devries, Mukesh Dherani, Eric L. Ding, E. Ray Dorsey, Tim Driscoll, Karen Edmond, Suad Eltahir Ali, Rebecca E. Engell, Patricia J. Erwin, Saman Fahimi, Gail Falder, Farshad Farzadfar, Alize Ferrari, Mariel M. Finucane, Seth Flaxman, Francis Gerry R Fowkes, Greg Freedman, Michael K. Freeman, Emmanuela Gakidou, Santu Ghosh, Edward Giovannucci, Gerhard Gmel, Kathryn Graham, Rebecca Grainger, Bridget Grant, David Gunnell, Hialy R. Gutierrez, Wayne Hall, Hans W. Hoek, Anthony Hogan, H. Dean Hosgood, Damian Hoy, Howard Hu, Bryan J. Hubbell, Sally J. Hutchings, Sydney E. Ibeanusi, Gemma L. Jacklyn, Rashmi Jasrasaria, Jost B. Jonas, Haidong Kan, John A. Kanis, Nicholas Kassebaum, Norito Kawakami, Young Ho Khang, Shahab Khatibzadeh, Jon Paul Khoo, Cindy Kok, Francine Laden, Ratilal Lalloo, Qing Lan, Tim Lathlean, Janet L. Leasher, James Leigh, Yang Li, John Kent Lin, Steven E. Lipshultz, Stephanie London, Rafael Lozano, Yuan Lu, Joelle Mak, Reza Malekzadeh, Leslie Mallinger, Wagner Marcenes, Lyn March, Robin Marks, Randall Martin, Paul McGale, John McGrath, Sumi Mehta, George A. Mensah, Tony R. Merriman, Renata Micha, Catherine Michaud, Vinod Mishra, Khayriyyah Mohd Hanafiah, Ali A. Mokdad, Lidia Morawska, Dariush Mozaffarian, Tasha Murphy, Mohsen Naghavi, Bruce Neal, Paul K. Nelson, Joan Miquel Nolla, Rosana Norman, Casey Olives, Saad B. Omer, Jessica Orchard, Richard Osborne, Bart Ostro, Andrew Page, Kiran D. Pandey, Charles D H Parry, Erin Passmore, Jayadeep Patra, Neil Pearce, Pamela M. Pelizzari, Max Petzold, Michael R. Phillips, Dan Pope, C. Arden Pope, John Powles, Mayuree Rao, Homie Razavi, Eva A. Rehfuess, Jürgen T. Rehm, Beate Ritz, Frederick P. Rivara, Thomas Roberts, Carolyn Robinson, Jose A. Rodriguez-Portales, Isabelle Romieu, Robin Room, Lisa C. Rosenfeld, Ananya Roy, Lesley Rushton, Joshua A. Salomon, Uchechukwu Sampson, Lidia Sanchez-Riera, Ella Sanman, Amir Sapkota, Soraya Seedat, Peilin Shi, Kevin Shield, Rupak Shivakoti, Gitanjali M. Singh, David A. Sleet, Emma Smith, Kirk R. Smith, Nicolas J C Stapelberg, Kyle Steenland, Heidi Stöckl, Lars Jacob Stovner, Kurt Straif, Lahn Straney, George D. Thurston, Jimmy H. Tran, Rita Van Dingenen, Aaron Van Donkelaar, J. Lennert Veerman, Lakshmi Vijayakumar, Robert Weintraub, Myrna M. Weissman, Richard A. White, Harvey Whiteford, Steven T. Wiersma, James D. Wilkinson, Hywel C. Williams, Warwick Williams, Nicholas Wilson, Anthony D. Woolf, Paul Yip, Jan M. Zielinski, Alan D. Lopez, Christopher J L Murray, and Majid Ezzati. A comparative risk assessment of burden of disease and injury attributable to 67 risk factors and risk factor clusters in 21 regions, 1990-2010: A systematic analysis for the Global Burden of Disease Study 2010. *The Lancet*, 380(9859):2224–2260, 2012. ISSN 01406736. doi: 10.1016/S0140-6736(12)61766-8.

Shian-Jiann Lin and Richard B. Rood. Multidimensional Flux-Form Semi-Lagrangian Transport Schemes. *Monthly Weather Review*, 124(9):2046–2070, sep 1996. ISSN 0027-0644. doi: 10.1175/1520-0493(1996)124⟨2046:MFFSLT⟩2.0.CO;2. URL http://journals.ametsoc.org/doi/abs/10.1175/1520-0493{%}281996{%}29124{%}3C2046{%}3AMFFSLT{%}3E2.0.CO{%}3B2.

Chao Liu, Barron H. Henderson, Dongfang Wang, Xinyuan Yang, and Zhong ren Peng. A land use regression application into assessing spatial variation of intra-urban fine particulate matter (pm2.5) and nitrogen dioxide (no2) concentrations in city of shanghai, china. *Science of the Total Environment*, 565:607 – 615, 2016. ISSN 0048-9697. doi: https://doi.org/10.1016/j.scitotenv.2016.03.189. URL http://www.sciencedirect.com/science/article/pii/S004896971630609X.

Zhaoyan Liu, Mark Vaughan, David Winker, Chieko Kittaka, Brian Getzewich, Ralph Kuehn, Ali Omar, Kathleen Powell, Charles Trepte, and Chris Hostetler. The CALIPSO Lidar Cloud and Aerosol Discrimination: Version 2 Algorithm and Initial Assessment of Performance. *Journal of Atmospheric and Oceanic Technology*, 26 (7):1198–1213, jul 2009. ISSN 0739-0572. doi: 10.1175/2009JTECHA1229.1.

Zhiquan Liu, Quanhua Liu, Hui-Chuan Lin, Craig S Schwartz, Yen-Huei Lee, and Tijian Wang. Three-dimensional variational assimilation of MODIS aerosol optical depth: Implementation and application to a dust storm over East Asia. *Journal of Geophysical Research: Atmospheres*, 116(D23):n/a–n/a, dec 2011. ISSN 01480227. doi: 10.1029/2011JD016159. URL http://doi.wiley.com/10.1029/2011JD016159.

Dana Loomis, Yann Grosse, Béatrice Lauby-Secretan, Fatiha El Ghissassi, Véronique Bouvard, Lamia Benbrahim-Tallaa, Neela Guha, Robert Baan, Heidi Mattock, and Kurt Straif. The carcinogenicity of outdoor air pollution. *The Lancet Oncology*, 14(13):1262–1263, 12 2013. doi: http://dx.doi.org.ezproxy.library.dal.ca/10.1016/S1470-2045(13)70487-X.

Rafael Lozano, Mohsen Naghavi, Kyle Foreman, Stephen Lim, Kenji Shibuya, Victor Aboyans, Jerry Abraham, Timothy Adair, Rakesh Aggarwal, Stephanie Y. Ahn, Miriam Alvarado, H. Ross Anderson, Laurie M. Anderson, Kathryn G. Andrews, Charles Atkinson, Larry M. Baddour, Suzanne Barker-Collo, David H. Bartels, Michelle L. Bell, Emelia J. Benjamin, Derrick Bennett, Kavi Bhalla, Boris Bikbov, Aref Bin Abdulhak, Gretchen Birbeck, Fiona Blyth, Ian Bolliger, Soufi Ane Boufous, Chiara Bucello, Michael Burch, Peter Burney, Jonathan Carapetis, Honglei Chen, David Chou, Sumeet S. Chugh, Luc E. Coffeng, Steven D. Colan, Samantha Colquhoun, K. Ellicott Colson, John Condon, Myles D. Connor, Leslie T. Cooper, Matthew Corriere, Monica Cortinovis, Karen Courville de Vaccaro, William Couser, Benjamin C. Cowie, Michael H. Criqui, Marita Cross, Kaustubh C. Dabhadkar, Nabila Dahodwala, Diego De Leo, Louisa Degenhardt, Allyne Delossantos, Julie Denenberg, Don C. Des Jarlais, Samath D. Dharmaratne, E. Ray

Dorsey, Tim Driscoll, Herbert Duber, Beth Ebel, Patricia J. Erwin, Patricia Espindola, Majid Ezzati, Valery Feigin, Abraham D. Flaxman, Mohammad H. Forouzanfar, Francis Gerry R. Fowkes, Richard Franklin, Marlene Fransen, Michael K. Freeman, Sherine E. Gabriel, Emmanuela Gakidou, Flavio Gaspari, Richard F. Gillum, Diego Gonzalez-Medina, Yara A. Halasa, Diana Haring, James E. Harrison, Rasmus Havmoeller, Roderick J. Hay, Bruno Hoen, Peter J. Hotez, Damian Hoy, Kathryn H. Jacobsen, Spencer L. James, Rashmi Jasrasaria, Sudha Jayaraman, Nicole Johns, Ganesan Karthikeyan, Nicholas Kassebaum, Andre Keren, Jon-Paul Khoo, Lisa Marie Knowlton, Olive Kobusingye, Adofo Koranteng, Rita Krishnamurthi, Michael Lipnick, Steven E. Lipshultz, Summer Lockett Ohno, Jacqueline Mabweijano, Michael F. MacIntyre, Leslie Mallinger, Lyn March, Guy B. Marks, Robin Marks, Akira Matsumori, Richard Matzopoulos, Bongani M. Mayosi, John H. McAnulty, Mary M. McDermott, John McGrath, George A. Mensah, Tony R. Merriman, Catherine Michaud, Matthew Miller, Ted R. Miller, Charles Mock, Ana Olga Mocumbi, Ali A. Mokdad, Andrew Moran, Kim Mulholland, M. Nathan Nair, Luigi Naldi, K. M. Venkat Narayan, Kiumarss Nasseri, Paul Norman, Martin O'Donnell, Saad B. Omer, Katrina Ortblad, Richard Osborne, Doruk Ozgediz, Bishnu Pahari, Jeyaraj Durai Pandian, Andrea Panozo Rivero, Rogelio Perez Padilla, Fernando Perez-Ruiz, Norberto Perico, David Phillips, Kelsey Pierce, III Pope C.Arden, Esteban Porrini, Farshad Pourmalek, Murugesan Raju, Dharani Ranganathan, Juergen T. Rehm, David B. Rein, Guiseppe Remuzzi, Frederick P. Rivara, Thomas Roberts, Felipe Rodriguez De Leon, Lisa C. Rosenfeld, Lesley Rushton, Ralph L. Sacco, Joshua A. Salomon, Uchechukwu Sampson, Ella Sanman, David C. Schwebel, Maria Segui-Gomez, Donald S. Shepard, David Singh, Jessica Singleton, Karen Sliwa, Emma Smith, Andrew Steer, Jennifer A. Taylor, Bernadette Thomas, Imad M. Tleyjeh, Jeffrey A. Towbin, Thomas Truelsen, Eduardo A. Undurraga, N. Venketasubramanian, Lakshmi Vijayakumar, Theo Vos, Gregory R. Wagner, Mengru Wang, Wenzhi Wang, Kerrianne Watt, Martin A. Weinstock, Robert Weintraub, James D. Wilkinson, Anthony D. Woolf, Sarah Wulf, Pon-Hsiu Yeh, Paul Yip, Azadeh Zabetian, Zhi-Jie Zheng, Alan D. Lopez, and Christopher J. L. Murray. Global and regional mortality from 235 causes of death for 20 age groups in 1990 and 2010: a systematic analysis for the global burden of disease study 2010. *The Lancet*, 380(9859):2095–2128, DEC 15 2012. Article.

Peng Lynch, Jeffrey S. Reid, Douglas L. Westphal, Jianglong Zhang, Timothy F. Hogan, Edward J. Hyer, Cynthia A. Curtis, Dean A. Hegg, Yingxi Shi, James R. Campbell, Juli I. Rubin, Walter R. Sessions, F. Joseph Turk, and Annette L. Walker. An 11-year global gridded aerosol optical thickness reanalysis (v1.0) for atmospheric and climate sciences. *Geoscientific Model Development*, 9(4):1489–1522, apr 2016. ISSN 1991-9603. doi: 10.5194/gmd-9-1489-2016. URL `http://www.geosci-model-dev.net/9/1489/2016/`.

Christopher S. Malley, Mike R. Ashmore, Johan C. Kuylenstierna, I, James A. McGrath, Miriam A. Byrne, Chrysanthi Dimitroulopoulou, and Daniel Benefoh. Microenvironmental modelling of personal fine particulate matter exposure in Accra,

Ghana. *Atmospheric Environment*, 225, MAR 15 2020. ISSN 1352-2310. doi: {10.1016/j.atmosenv.2020.117376}.

R. E. Mamouri, V. Amiridis, a. Papayannis, E. Giannakaki, G. Tsaknakis, and D. S. Balis. Validation of CALIPSO space-borne-derived attenuated backscatter coefficient profiles using a ground-based lidar in Athens, Greece. *Atmospheric Measurement Techniques*, 2(2):513–522, 2009. ISSN 1867-1381. doi: 10.5194/amt-2-513-2009.

J. Mao, S. Fan, D. J. Jacob, and K. R. Travis. Radical loss in the atmosphere from Cu-Fe redox coupling in aerosols. *Atmospheric Chemistry and Physics*, 13(2): 509–519, jan 2013. ISSN 1680-7324. doi: 10.5194/acp-13-509-2013. URL `http://www.atmos-chem-phys.net/13/509/2013/`.

Raleigh L. Martin, Jasper F. Kok, Chris H. Hugenholtz, Thomas E. Barchyn, Marcelo Chamecki, and Jean T. Ellis. High-frequency measurements of aeolian saltation flux: Field-based methodology and applications. *Aeolian Research*, 30:97 – 114, 2018. ISSN 1875-9637. doi: https://doi.org/10.1016/j.aeolia.2017.12.003. URL `http://www.sciencedirect.com/science/article/pii/S1875963717301246`.

Randall Martin, V, Michael Brauer, Aaron van Donkelaar, Gavin Shaddick, Urvashi Narain, and Sagnik Dey. No one knows which city has the highest concentration of fine particulate matter. *Atmospheric Environment: X*, 3, JUL 2019. doi: {10.1016/j.aeaoa.2019.100040}.

Randall V Martin, Daniel J Jacob, Robert M. Yantosca, Mian Chin, and Paul Ginoux. Global and regional decreases in tropospheric oxidants from photochemical effects of aerosols. *Journal of Geophysical Research: Atmospheres*, 108(D3):n/a–n/a, feb 2003. ISSN 01480227. doi: 10.1029/2002JD002622. URL `http://doi.wiley.com/10.1029/2002JD002622`.

Thiago G. Martins, Daniel Simpson, Finn Lindgren, and Håvard Rue. Bayesian computing with inla: New features. *Computational Statistics & Data Analysis*, 67:68 – 83, 2013. ISSN 0167-9473. doi: https://doi.org/10.1016/j.csda.2013.04.014. URL `http://www.sciencedirect.com/science/article/pii/S0167947313001552`.

John Martonchik, Ralph Kahn, and David Diner. *Retrieval of aerosol properties over land using MISR observations*, pages 267–293. 08 2009. ISBN 978-3-540-69396. doi: 10.1007/978-3-540-69397-0_9.

Colin D. Mathers and Dejan Loncar. Projections of global mortality and burden of disease from 2002 to 2030. *PLoS Medicine*, 3(11):2011–2030, 2006. ISSN 15491277. doi: 10.1371/journal.pmed.0030442.

T Mielonen, A Arola, M Komppula, J Kukkonen, J Koskinen, G de Leeuw, and K E J Lehtinen. Comparison of CALIOP level 2 aerosol subtypes to aerosol types derived from AERONET inversion data. *Geophysical Research Letters*, 36, sep 2009. ISSN 0094-8276. doi: 10.1029/2009GL039609.

G. E. Moore. Cramming more components onto integrated circuits. *Proceedings of the IEEE*, 86(1):82–85, Jan 1998. ISSN 1558-2256. doi: 10.1109/JPROC.1998.658762.

José Luis Morales and Jorge Nocedal. Remark on "algorithm 778: L-BFGS-B: Fortran subroutines for large-scale bound constrained optimization". *ACM Transactions on Mathematical Software*, 38(1):1–4, 2011. ISSN 00983500. doi: 10.1145/2049662.2049669. URL http://dl.acm.org/citation.cfm?doid=2049662.2049669.

Christopher JL Murray, M. Ezzati, AD Lopez, A. Rodgers, and S. Vander Hoorn. *Comparative Quantification of Health Risk: conceptual framework and methodological issues*. Comparative Quantification of Health Risks, Volume 1. World Health Organization, Geneva, Switzerland, 2004.

Masoud M. Nasari, Mieczysław Szyszkowicz, Hong Chen, Daniel Crouse, Michelle C. Turner, Michael Jerrett, C. Arden Pope, Bryan Hubbell, Neal Fann, Aaron Cohen, Susan M. Gapstur, W. Ryan Diver, David Stieb, Mohammad H. Forouzanfar, Sun-Young Kim, Casey Olives, Daniel Krewski, and Richard T. Burnett. A class of non-linear exposure-response models suitable for health impact assessment applicable to large cohort studies of ambient air pollution. *Air Quality, Atmosphere & Health*, 9(8):961–972, dec 2016. ISSN 1873-9318. doi: 10.1007/s11869-016-0398-z. URL http://link.springer.com/10.1007/s11869-016-0398-z.

A. H. Omar, D. M. Winker, J. L. Tackett, D. M. Giles, J. Kar, Z. Liu, M. A. Vaughan, K. A. Powell, and C. R. Trepte. CALIOP and AERONET aerosol optical depth comparisons: One size fits none. *Journal of Geophysical Research: Atmospheres*, 118(10):4748–4766, may 2013. ISSN 2169-897X. doi: 10.1002/jgrd.50330.

Task Force on Hemispheric Transport of Air Pollution. Hemispheric transport of air pollution 2010: Part a: Ozone and particulate matter. Technical Report 17, United Nations Publications, 2010.

X. Pan, M. Chin, R. Gautam, H. Bian, D. Kim, P. R. Colarco, T. L. Diehl, T. Takemura, L. Pozzoli, K. Tsigaridis, S. Bauer, and N. Bellouin. A multi-model evaluation of aerosols over South Asia: common problems and possible causes. *Atmospheric Chemistry and Physics*, 15(10):5903–5928, may 2015. ISSN 1680-7324. doi: 10.5194/acp-15-5903-2015. URL http://www.atmos-chem-phys.net/15/5903/2015/.

Amanda J. Pappin, Tanya Christidis, Lauren L. Pinault, Dan L. Crouse, Jeffrey R. Brook, Anders Erickson, Perry Hystad, Chi Li, Randall V. Martin, Jun Meng, Scott Weichenthal, Aaron van Donkelaar, Michael Tjepkema, Michael Brauer, and Richard T. Burnett. Examining the shape of the association between low levels of fine particulate matter and mortality across three cycles of the canadian census health and environment cohort. *Environmental Health Perspectives*, 127(10):107008, 2019. doi: 10.1289/EHP5204. URL https://ehp.niehs.nih.gov/doi/abs/10.1289/EHP5204.

Amanda Joy Pappin and Amir Hakami. Source attribution of health benefits from air pollution abatement in canada and the united states: An adjoint sensitivity analysis. *Environmental Health Perspectives*, 121(5):572–579, MAY 2013. doi: 10.1289/ehp.1205561. Article.

Rokjin J. Park, Daniel J. Jacob, Mian Chin, and Randall V. Martin. Sources of carbonaceous aerosols over the United States and implications for natural visibility. *Journal of Geophysical Research*, 108(D12):4355, 2003. ISSN 0148-0227. doi: 10.1029/2002JD003190. URL http://doi.wiley.com/10.1029/2002JD003190.

Rokjin J. Park, D J Jacob, B D Field, R M Yantosca, and M Chin. Natural and transboundary pollution influences on sulfate-nitrate-ammonium aerosols in the United States: implications for policy. *Journal of Geophysical Research*, 109 (D15204):D15204, 2004. ISSN 0148-0227. doi: 10.1029/2003JD004473. URL http://doi.wiley.com/10.1029/2003JD004473.

Antti-Ilari Partanen, Harri Kokkola, Sami Romakkaniemi, Veli-Matti Kerminen, Kari E. J. Lehtinen, Tommi Bergman, Antti Arola, and Hannele Korhonen. Direct and indirect effects of sea spray geoengineering and the role of injected particle size. *Journal of Geophysical Research: Atmospheres*, 117(D2), 2012. doi: 10.1029/2011JD016428. URL https://agupubs.onlinelibrary.wiley.com/doi/abs/10.1029/2011JD016428.

Antti-Ilari Partanen, David P. Keller, Hannele Korhonen, and H. Damon Matthews. Impacts of sea spray geoengineering on ocean biogeochemistry. *Geophysical Research Letters*, 43(14):7600–7608, 2016. doi: 10.1002/2016GL070111. URL https://agupubs.onlinelibrary.wiley.com/doi/abs/10.1002/2016GL070111.

Markus D. Petters, Matteo Rinaldi, Stefano Decesari, Emanuela Finessi, Lara Giulianelli, Claudio Carbone, Sandro Fuzzi, Colin D. O'Dowd, Darius Ceburnis, and Maria Cristina Facchini. Primary and secondary organic marine aerosol and oceanic biological activity: Recent results and new perspectives for future studies. *Advances in Meteorology*, 2010. doi: 10.1155/2010/310682.

Sajeev Philip, Randall V Martin, Graydon Snider, Crystal L Weagle, Aaron van Donkelaar, Michael Brauer, Daven K Henze, Zbigniew Klimont, Chandra Venkataraman, Sarath K Guttikunda, and Qiang Zhang. Anthropogenic fugitive, combustion and industrial dust is a significant, underrepresented fine particulate matter source in global atmospheric models. *Environmental Research Letters*, 12(4):044018, apr 2017. doi: 10.1088/1748-9326/aa65a4. URL https://doi.org/10.1088%2F1748-9326%2Faa65a4.

C. Arden Pope, Jacob S. Lefler, Majid Ezzati, Joshua D. Higbee, Julian D. Marshall, Sun-Young Kim, Matthew Bechle, Kurtis S. Gilliat, Spencer E. Vernon, Allen L. Robinson, and Richard T. Burnett. Mortality risk and fine particulate air pollution in a large, representative cohort of u.s. adults. *Environmental Health Perspectives*,

127(7):077007, 2019. doi: 10.1289/EHP4438. URL https://ehp.niehs.nih.gov/doi/abs/10.1289/EHP4438.

Miquel Porta. *A Dictionary of Epidemiology*. Oxford University Press, 2016. ISBN 9780199976720. URL https://www.oxfordreference.com/view/10.1093/acref/9780199976720.001.0001/acref-9780199976720.

George Pouliot, Heather Simon, Prakash Bhave, Daniel Tong, David Mobley, Tom Pace, and Thomas Pierce. Assessing the anthropogenic fugitive dust emission inventory and temporal allocation using an updated speciation of particulate matter. In Douw G. Steyn and Silvia Trini Castelli, editors, *Air Pollution Modeling and its Application XXI*, pages 585–589, Dordrecht, 2012. Springer Netherlands. ISBN 978-94-007-1359-8.

Anna P. Protonotariou, Maria Tombrou, Christos Giannakopoulos, Effie Kostopoulou, and Philippe Le Sager. Study of co surface pollution in europe based on observations and nested-grid applications of geos-chem global chemical transport model. *Tellus B*, 62(4):209–227, 2010. doi: 10.1111/j.1600-0889.2010.00462.x. URL https://onlinelibrary.wiley.com/doi/abs/10.1111/j.1600-0889.2010.00462.x.

Annette Prüss-üstün, Diarmid Campbell-lendrum, Carlos Corvalán, and Alistair Woodward. Introduction and methods: Assessing the environmental burden of disease at national and local levels. *World Health Organization*, (1), 2003.

Elizabeth M. Punger and J. Jason West. The effect of grid resolution on estimates of the burden of ozone and fine particulate matter on premature mortality in the USA. *Air Quality, Atmosphere and Health*, 6(3):563–573, 2013. ISSN 18739318. doi: 10.1007/s11869-013-0197-8.

William M. Putman and Shian-Jiann Lin. Finite-volume transport on various cubed-sphere grids. *Journal of Computational Physics*, 227(1):55 – 78, 2007. ISSN 0021-9991. doi: https://doi.org/10.1016/j.jcp.2007.07.022. URL http://www.sciencedirect.com/science/article/pii/S0021999107003105.

H. O. T. Pye, H. Liao, S. Wu, L. J. Mickley, D. J. Jacob, D. K. Henze, and J. H. Seinfeld. Effect of changes in climate and emissions on future sulfate-nitrate-ammonium aerosol levels in the united states. *Journal of Geophysical Research: Atmospheres*, 114(D1), 2009. doi: 10.1029/2008JD010701. URL https://agupubs.onlinelibrary.wiley.com/doi/abs/10.1029/2008JD010701.

C. A. Randles, A. M. da Silva, V. Buchard, P. R. Colarco, A. Darmenov, R. Govindaraju, A. Smirnov, B. Holben, R. Ferrare, J. Hair, Y. Shinozuka, and C. J. Flynn. The merra-2 aerosol reanalysis, 1980 onward. part i: System description and data assimilation evaluation. *Journal of Climate*, 30(17):6823–6850, 2017. doi: 10.1175/JCLI-D-16-0609.1. URL https://doi.org/10.1175/JCLI-D-16-0609.1.

Jennifer Richmond-Bryant and Thomas C. Long. Influence of exposure measurement errors on results from epidemiologic studies of different designs. *Journal of Exposure Science and Environmental Epidemiology*, 30(3):420–429, MAY 2020. ISSN 1559-0631. doi: {10.1038/s41370-019-0164-z}.

D. A. Ridley, C. L. Heald, and B. Ford. North African dust export and deposition: A satellite and model perspective. *Journal of Geophysical Research: Atmospheres*, 117(D2), jan 2012. ISSN 01480227. doi: 10.1029/2011JD016794. URL `http://doi.wiley.com/10.1029/2011JD016794`.

Michele M Rienecker, MJ Suarez, R Todling, J Bacmeister, L Takacs, HC Liu, W Gu, M Sienkiewicz, RD Koster, R Gelaro, I. Stajner, and J.E. Nielse. The geos-5 data assimilation system: Documentation of versions 5.0.1, 5.1.0, and 5.2.0. Technical report, NASA, 2008.

Michele M. Rienecker, Max J. Suarez, Ronald Gelaro, Ricardo Todling, Julio Bacmeister, Emily Liu, Michael G. Bosilovich, Siegfried D. Schubert, Lawrence Takacs, Gi-Kong Kim, Stephen Bloom, Junye Chen, Douglas Collins, Austin Conaty, Arlindo da Silva, Wei Gu, Joanna Joiner, Randal D. Koster, Robert Lucchesi, Andrea Molod, Tommy Owens, Steven Pawson, Philip Pegion, Christopher R. Redder, Rolf Reichle, Franklin R. Robertson, Albert G. Ruddick, Meta Sienkiewicz, and Jack Woollen. Merra: Nasa's modern-era retrospective analysis for research and applications. *Journal of Climate*, 24(14):3624–3648, 2011. doi: 10.1175/JCLI-D-11-00015.1. URL `https://doi.org/10.1175/JCLI-D-11-00015.1`.

R R Rogers, C A Hostetler, J W Hair, R A Ferrare, Z Liu, M D Obland, D B Harper, A L Cook, K A Powell, M A Vaughan, and D M Winker. Assessment of the CALIPSO Lidar 532 nm attenuated backscatter calibration using the NASA LaRC airborne High Spectral Resolution Lidar. *Atmospheric Chemistry and Physics*, 11 (3):1295–1311, 2011. ISSN 1680-7316. doi: 10.5194/acp-11-1295-2011.

R. R. Rogers, M. A. Vaughan, C. A. Hostetler, S. P. Burton, R. A. Ferrare, S. A. Young, J. W. Hair, M. D. Obland, D. B. Harper, A. L. Cook, and D. M. Winker. Looking through the haze: evaluating the CALIPSO level 2 aerosol optical depth using airborne high spectral resolution lidar data. *Atmospheric Measurement Techniques*, 7(12):4317–4340, 2014. ISSN 1867-1381. doi: 10.5194/amt-7-4317-2014.

Håvard Rue, Sara Martino, and Nicolas Chopin. Approximate bayesian inference for latent gaussian models by using integrated nested laplace approximations. *Journal of the Royal Statistical Society: Series B (Statistical Methodology)*, 71(2):319–392, 2009. doi: 10.1111/j.1467-9868.2008.00700.x. URL `https://rss.onlinelibrary.wiley.com/doi/abs/10.1111/j.1467-9868.2008.00700.x`.

D. E. Rumelhart, G. E. Hinton, and R. J. Williams. *Learning Internal Representations by Error Propagation*, page 318–362. MIT Press, Cambridge, MA, USA, 1986. ISBN 026268053X.

Yves Rybarczyk and Rasa Zalakeviciute. Machine learning approaches for outdoor air quality modelling: A systematic review. *Applied Sciences*, 8(12), 2018. ISSN 2076-3417. doi: 10.3390/app8122570. URL `https://www.mdpi.com/2076-3417/8/12/2570`.

E. Saikawa, J. Kurokawa, M. Takigawa, J. Borken-Kleefeld, D. L. Mauzerall, L. W. Horowitz, and T. Ohara. The impact of China's vehicle emissions on regional air quality in 2000 and 2020: A scenario analysis. *Atmospheric Chemistry and Physics*, 11(18):9465–9484, 2011. ISSN 16807316. doi: 10.5194/acp-11-9465-2011.

VV SALOMONSON, WL BARNES, PW MAYMON, HE MONTGOMERY, and H OSTROW. MODIS - ADVANCED FACILITY INSTRUMENT FOR STUDIES OF THE EARTH AS A SYSTEM. *Ieee Transactions on Geoscience and Remote Sensing*, 27(2):145–153, MAR 1989. ISSN 0196-2892. doi: {10.1109/36.20292}.

A. M. Sayer, L. A. Munchak, N. C. Hsu, R. C. Levy, C. Bettenhausen, and M.-J. Jeong. Modis collection 6 aerosol products: Comparison between aqua's e-deep blue, dark target, and "merged" data sets, and usage recommendations. *Journal of Geophysical Research: Atmospheres*, 119(24):13,965–13,989, 2014. doi: 10.1002/2014JD022453. URL `https://agupubs.onlinelibrary.wiley.com/doi/abs/10.1002/2014JD022453`.

John H. Seinfeld and Spyros N. Pandis. *Atmospheric Chemistry and Physics: From Air Pollution to Climate Change*. John Wiley and Sons, Inc., 3 edition, 2016. ISBN 978-1-118-94740-1.

T. T. Sekiyama, T. Y. Tanaka, a. Shimizu, and T. Miyoshi. Data assimilation of CALIPSO aerosol observations. *Atmospheric Chemistry and Physics Discussions*, 9(2):5785–5808, 2009. ISSN 1680-7316. doi: 10.5194/acpd-9-5785-2009.

Tsuyoshi Thomas Sekiyama, Taichu Y. Tanaka, Takashi Maki, and Masao Mikami. The Effects of Snow Cover and Soil Moisture on Asian Dust: II. Emission Estimation by Lidar Data Assimilation. *Scientific Online Letters on the Atmosphere*, 7A (Special_Edition):40–43, 2011. ISSN 1349-6476. doi: 10.2151/sola.7A-011.

Gavin Shaddick, Matthew L. Thomas, Amelia Green, Michael Brauer, Aaron van Donkelaar, Rick Burnett, Howard H. Chang, Aaron Cohen, Rita Van Dingenen, Carlos Dora, Sophie Gumy, Yang Liu, Randall Martin, Lance A. Waller, Jason West, James V. Zidek, and Annette Prüss-Ustün. Data integration model for air quality: A hierarchical approach to the global estimation of exposures to ambient air pollution. *Journal of the Royal Statistical Society. Series C: Applied Statistics*, pages 231–253, 2017. ISSN 14679876. doi: 10.1111/rssc.12227.

Huanfeng Shen, Tongwen Li, Qiangqiang Yuan, and Liangpei Zhang. Estimating regional ground-level pm2.5 directly from satellite top-of-atmosphere relectance using deep beliefe networks. *Journal of Geophysical Research: Atmospheres*, pages 13,875–13,886, 2018. doi: 10.1029/2018JD028759.

K. Sindelarova, C. Granier, I. Bouarar, A. Guenther, S. Tilmes, T. Stavrakou, J. F. Muller, U. Kuhn, P. Stefani, and W. Knorr. Global data set of biogenic VOC emissions calculated by the MEGAN model over the last 30 years. *Atmospheric Chemistry and Physics*, 14(17):9317–9341, 2014. ISSN 1680-7316. doi: {10.5194/acp-14-9317-2014}.

A. Smirnov, B.N. Holben, T.F. Eck, O. Dubovik, and I. Slutsker. Cloud-screening and quality control algorithms for the aeronet database. *Remote Sensing of Environment*, 73(3):337 – 349, 2000. ISSN 0034-4257. doi: https://doi.org/10.1016/S0034-4257(00)00109-7. URL `http://www.sciencedirect.com/science/article/pii/S0034425700001097`.

O Talagrand. Assimilation of observations, an introduction. *Journal of the Meteorological Society of Japan*, 75(1B):191–209, MAR 1997. ISSN 0026-1165. doi: {10.2151/jmsj1965.75.1B_191}. 2nd WMO International Symposium on Assimilation of Observations in Meteorology and Oceanography, TOKYO, JAPAN, MAR 13-17, 1995.

The International GEOS-Chem User Community. geoschem/geos-chem: Geos-chem 12.8.2, May 2020. URL `https://doi.org/10.5281/zenodo.3860693`. Please see the LICENSE.txt and AUTHORS.txt files in the root folder for the GEOS-Chem license description (based on the MIT license) and a complete list of authors. For more information about GEOS-Chem in general, please see www.geos- chem.org and wiki.geos-chem.org.

T. D. Toth, J. R. Campbell, J. S. Reid, J. L. Tackett, M. A. Vaughan, J. Zhang, and J. W. Marquis. Minimum aerosol layer detection sensitivities and their subsequent impacts on aerosol optical thickness retrievals in calipso level 2 data products. *Atmospheric Measurement Techniques*, 11(1):499–514, 2018. doi: 10.5194/amt-11-499-2018. URL `https://www.atmos-meas-tech.net/11/499/2018/`.

Travis D Toth, Jianglong Zhang, James R Campbell, Jeffrey S Reid, Yingxi Shi, Randall S Johnson, Alexander Smirnov, Mark A Vaughan, and David M Winker. Investigating enhanced Aqua MODIS aerosol optical depth retrievals over the mid-to-high latitude Southern Oceans through intercomparison with co-located CALIOP, MAN, and AERONET data sets. *Journal of Geophysical Research: Atmospheres*, 118(10):4700–4714, may 2013. ISSN 2169897X. doi: 10.1002/jgrd.50311. URL `http://doi.wiley.com/10.1002/jgrd.50311`.

Ioannis Tsamardinos, Constantin F. Aliferis, Alexander R. Statnikov, and Er Statnikov. Algorithms for large scale markov blanket discovery. In *In The 16th International FLAIRS Conference, St*, volume 2, pages 376–380. FLAIRS, 2003.

United States Environmental Protection Agency. Benefits and costs of the clean air act: 1970 to 1990. Technical report, EPA, 1997.

United States Environmental Protection Agency. The benefits and costs of the clean air act 1990 to 2010. Technical report, U.S. Environmental Protection Agency, 1999.

A. van Donkelaar, R. V. Martin, M. Brauer, and B. L. Boys. Use of satellite observations for long-term exposure assessment of global concentrations of fine particulate matter. *Environ.health Perspect.*, 123:135–143, 2015. doi: 10.1289/ehp.1408646.

Aaron van Donkelaar, Randall V. Martin, Michael Brauer, Ralph Kahn, Robert Levy, Carolyn Verduzco, and Paul J. Villeneuve. Global estimates of ambient fine particulate matter concentrations from satellite-based aerosol optical depth: Development and application. *Environmental Health Perspectives*, 118(6):847–855, 2010. ISSN 00916765. doi: 10.1289/ehp.0901623.

Aaron van Donkelaar, Randall V. Martin, Robert J D Spurr, Easan Drury, Lorraine A. Remer, Robert C. Levy, and Jun Wang. Optimal estimation for global ground-level fine particulate matter concentrations. *Journal of Geophysical Research Atmospheres*, 118(11):5621–5636, jun 2013. ISSN 21698996. doi: 10.1002/jgrd.50479.

Aaron Van Donkelaar, Randall V. Martin, Michael Brauer, N. Christina Hsu, Ralph A. Kahn, Robert C. Levy, Alexei Lyapustin, Andrew M. Sayer, and David M. Winker. Global Estimates of Fine Particulate Matter using a Combined Geophysical-Statistical Method with Information from Satellites, Models, and Monitors. *Environmental Science and Technology*, 50(7):3762–3772, 2016. ISSN 15205851. doi: 10.1021/acs.est.5b05833.

Alina Vodonos, Yara Abu Awad, and Joel Schwartz. The concentration-response between long-term pm2.5 exposure and mortality; a meta-regression approach. *Environmental Research*, 166:677 – 689, 2018. ISSN 0013-9351. doi: https://doi.org/10.1016/j.envres.2018.06.021. URL `http://www.sciencedirect.com/science/article/pii/S0013935118303256`.

Ulla Wandinger. *Introduction to Lidar*, pages 1–18. Springer New York, New York, NY, 2005. ISBN 978-0-387-25101-1. doi: 10.1007/0-387-25101-4_1. URL `https://doi.org/10.1007/0-387-25101-4_1`.

Chenxi Wang, Ping Yang, Bryan A Baum, Steven Platnick, Andrew K Heidinger, Yongxiang Hu, and Robert E Holz. Retrieval of Ice Cloud Optical Thickness and Effective Particle Size Using a Fast Infrared Radiative Transfer Model. *Journal of Applied Meteorology and Climatology*, 50(11):2283–2297, nov 2011. ISSN 1558-8424. doi: 10.1175/JAMC-D-11-067.1.

Haidong Wang, Laura Dwyer-Lindgren, Katherine T. Lofgren, Julie Knoll Rajaratnam, Jacob R. Marcus, Alison Levin-Rector, Carly E. Levitz, Alan D. Lopez, and Christopher J L Murray. Age-specific and sex-specific mortality in 187 countries, 1970-2010: A systematic analysis for the Global Burden of Disease

Study 2010. *The Lancet*, 380(9859):2071–2094, 2012. ISSN 01406736. doi: 10.1016/S0140-6736(12)61719-X.

K.-Y. Wang, D. J Lary, D. E. Shallcross, S. M. Hall, and J. A. Pyle. A review on the use of the adjoint method in four-dimensional atmospheric-chemistry data assimilation. *Quarterly Journal of the Royal Meteorological Society*, 127(576):2181–2204, jul 2001. ISSN 00359009. doi: 10.1002/qj.49712757616. URL `http://doi.wiley.com/10.1002/qj.49712757616`.

Yuxuan X. Wang, Michael B. McElroy, Daniel J. Jacob, and Robert M. Yantosca. A nested grid formulation for chemical transport over asia: Applications to co. *Journal of Geophysical Research: Atmospheres*, 109(D22), 2004. doi: 10.1029/2004JD005237. URL `https://agupubs.onlinelibrary.wiley.com/doi/abs/10.1029/2004JD005237`.

Crystal L. Weagle, Graydon Snider, Chi Li, Aaron van Donkelaar, Sajeev Philip, Paul Bissonnette, Jacqueline Burke, John Jackson, Robyn Latimer, Emily Stone, Ihab Abboud, Clement Akoshile, Nguyen Xuan Anh, Jeffrey Robert Brook, Aaron Cohen, Jinlu Dong, Mark D. Gibson, Derek Griffith, Kevin B. He, Brent N. Holben, Ralph Kahn, Christoph A. Keller, Jong Sung Kim, Nofel Lagrosas, Puji Lestari, Yeo Lik Khian, Yang Liu, Eloise A. Marais, J. Vanderlei Martins, Amit Misra, Ulfi Muliane, Rizki Pratiwi, Euardo J. Quel, Abdus Salam, Lior Segev, Sachchida N. Tripathi, Chien Wang, Qiang Zhang, Michael Brauer, Yinon Rudich, and Randall V. Martin. Global sources of fine particulat matter: interpretation of pm2.5 chemical composition observed by spartan using a gloabl chemical transport model. *Environmental Science and Technology*, 52:11670–11681, 2018. doi: 10.1021/acs.est.8b01658.

Kevin J Wecht, Daniel J Jacob, Christian Frankenberg, Zhe Jiang, and Donald R Blake. Mapping of North American methane emissions with high spatial resolution by inversion of SCIAMACHY satellite data. *Journal of Geophysical Research: Atmospheres*, 119(12):7741–7756, 2014. doi: 10.1002/2014JD021551. URL `https://agupubs.onlinelibrary.wiley.com/doi/abs/10.1002/2014JD021551`.

J. J. West, V. Naik, L. W. Horowitz, and a. M. Fiore. Effect of regional precursor emission controls on long-range ozone transport – Part 2: Steady-state changes in ozone air quality and impacts on human mortality. *Atmospheric Chemistry and Physics*, 9(16):6095–6107, aug 2009. ISSN 1680-7324. doi: 10.5194/acp-9-6095-2009. URL `http://www.atmos-chem-phys.net/9/6095/2009/`.

Bruce R. White. soil transport by winds on mars. *Journal of Geophysical Research: Solid Earth*, 84(B9):4643–4651, 1979. doi: 10.1029/JB084iB09p04643. URL `https://agupubs.onlinelibrary.wiley.com/doi/abs/10.1029/JB084iB09p04643`.

D M Winker, J L Tackett, B J Getzewich, Z Liu, M A Vaughan, and R R Rogers. The global 3-D distribution of tropospheric aerosols as characterized by CALIOP. *Atmospheric Chemistry and Physics*, 13(6):3345–3361, mar 2013. ISSN 1680-7324. doi:

10.5194/acp-13-3345-2013. URL http://www.atmos-chem-phys.net/13/3345/2013/.

David M. Winker, Mark A. Vaughan, Ali Omar, Yongxiang Hu, Kathleen A. Powell, Zhaoyan Liu, William H. Hunt, and Stuart A. Young. Overview of the CALIPSO mission and CALIOP data processing algorithms. *Journal of Atmospheric and Oceanic Technology*, 26(11):2310–2323, nov 2009. ISSN 07390572. doi: 10.1175/2009JTECHA1281.1.

Marcin L. Witek, Piotr J. Flatau, Patricia K. Quinn, and Douglas L. Westphal. Global sea-salt modeling: Results and validation against multicampaign shipboard measurements. *Journal of Geophysical Research*, 112(D8):D08215, apr 2007. ISSN 0148-0227. doi: 10.1029/2006JD007779. URL http://doi.wiley.com/10.1029/2006JD007779.

Shaowei Wu, Furong Deng, Jie Niu, Qinsheng Huang, Youcheng Liu, and Xinbiao Gu. Association of heart rate variability in taxi drivers with marked changes in particulate air pollution in beijing in 2008. *Environmental Health Perspectives*, 118 (1):87–91, JAN 2010. doi: 10.1289/ehp.0900818. Article.

J.-W. Xu, R.V. Martin, A. Morrow, S. Sharma, L. Huang, W. Richard Leaitch, J. Burkart, H. Schulz, M. Zanatta, M.D. Willis, D.K. Henze, C.J. Lee, A.B. Herber, and J.P.D. Abbatt. Source attribution of Arctic black carbon constrained by aircraft and surface measurements. *Atmospheric Chemistry and Physics*, 17(19), 2017. ISSN 16807324. doi: 10.5194/acp-17-11971-2017.

Xiaoguang Xu, Jun Wang, Daven K. Henze, Wenjun Qu, and Monika Kopacz. Constraints on aerosol sources using GEOS-Chem adjoint and MODIS radiances, and evaluation with multisensor (OMI, MISR) data. *Journal of Geophysical Research Atmospheres*, 118(12):6396–6413, 2013. ISSN 21698996. doi: 10.1002/jgrd.50515.

Jiayun Yao, Michael Brauer, Sean Raffuse, and Sarah B. Henderson. A machine learning approach to estimate hourly exposure to fine particulate matter for urban, rural, and remote populations during wildfire seasons. *Environmental Science and Technology*, 52:13239–13249, 2018. doi: 10.1021/acs.est.8b01921.

Peng Yin, Michael Brauer, Aaron Cohen, Richard T. Burnett, Jiangmei Liu, Yunning Liu, Ruiming Liang, Weihua Wang, Jinlei Qi, Lijun Wang, and Maigeng Zhou. Long-term fine particulate matter exposure and nonaccidental and cause-specific mortality in a large national cohort of chinese men. *Environmental Health Perspectives*, 125(11):117002, 2017. doi: 10.1289/EHP1673. URL https://ehp.niehs.nih.gov/doi/abs/10.1289/EHP1673.

Stuart A. Young and Mark A. Vaughan. The Retrieval of Profiles of Particulate Extinction from Cloud-Aerosol Lidar Infrared Pathfinder Satellite Observations (CALIPSO) Data: Algorithm Description. *Journal of Atmospheric and Oceanic Technology*, 26(6):1105–1119, 2009. ISSN 0739-0572. doi: 10.1175/

2008JTECHA1221.1. URL http://journals.ametsoc.org/doi/abs/10.1175/2008JTECHA1221.1.

K. Yumimoto, I. Uno, N. Sugimoto, a. Shimizu, Z. Liu, and D. M. Winker. Numerical modeling of Asian dust emission and transport with adjoint inversion using LIDAR network observations. *Atmospheric Chemistry and Physics Discussions*, 7 (6):15955–15987, 2007. doi: 10.5194/acpd-7-15955-2007.

K Yumimoto, K Eguchi, I Uno, T Takemura, Z Liu, A Shimizu, and N Sugimoto. An elevated large-scale dust veil from the Taklimakan Desert: Intercontinental transport and three-dimensional structure as captured by CALIPSO and regional and global models. *Atmospheric Chemistry and Physics*, 9(21):8545–8558, 2009. ISSN 1680-7316.

Charles S. Zender, Huisheng Bian, and David Newman. Mineral dust entrainment and deposition (dead) model: Description and 1990s dust climatology. *Journal of Geophysical Research: Atmospheres*, 108(D14), 2003. doi: 10.1029/2002JD002775. URL https://agupubs.onlinelibrary.wiley.com/doi/abs/10.1029/2002JD002775.

Jianglong Zhang, James R. Campbell, Edward J Edwaed J. Hyer, Jeffrey S. Reid, Douglas L. Westphal, and Randall S Johnson. Evaluating the impact of multisensor data assimilation on a global aerosol particle transport model. *Journal of Geophysical Research: Atmospheres*, 119(8):4674–4689, apr 2014. ISSN 21698996. doi: 10.1002/2013JD020975.Received.

L. Zhang, D. K. Henze, G. A. Grell, G. R. Carmichael, N. Bousserez, Q. Zhang, O. Torres, C. Ahn, Z. Lu, J. Cao, and Y. Mao. Constraining black carbon aerosol over Asia using OMI aerosol absorption optical depth and the adjoint of GEOS-Chem. *Atmospheric Chemistry and Physics*, 2015a. ISSN 16807324. doi: 10.5194/acp-15-10281-2015.

Q. Q. Zhang, Y. Wang, Q. Ma, Y. Yao, Y. Xie, and K. He. Regional differences in chinese so_2 emission control efficiency and policy implications. *Atmospheric Chemistry and Physics*, 15(11):6521–6533, 2015b. doi: 10.5194/acp-15-6521-2015. URL https://www.atmos-chem-phys.net/15/6521/2015/.

Appendix A

Supporting Information for Response of global particulate-matter-related mortality to changes in local precursor emissions

Supporting Information for Response of global particulate-matter-related mortality to changes in local precursor emissions

Colin J Lee[1], Randall V Martin[1,2], Daven K Henze[3], Michael Brauer[4], Aaron Cohen[5], and Aaron van Donkelaar[1]

[1]Dalhousie University, Halifax, Nova Scotia, Canada

[2]Harvard-Smithsonian Center for Astrophysics, Cambridge, MA, USA

[3]University of Colorado, Boulder, CO, USA

[4]School of Population and Public Health, University of British Columbia, Vancouver, BC, Canada

[5]Health Effects Institute, Boston, MA, USA

S-1 Impacts of resolution

In this study, satellite remote sensing was used to calculate global exposure. These data were used at a 0.1ºx0.1º resolution, while the GEOS-Chem adjoint operates at 2ºx2.5º. Table S-1 quantifies how population-weighted $PM_{2.5}$ concentrations are affected by resolution.

Table S-1: Population-weighted concentration by resolution, by source of $PM_{2.5}$ concentration data, and by GBD region.

Region	Population Weighted $PM_{2.5}$ Concentration [µg/m3]			
	GEOS-Chem 2ºx2.5º	GEOS-Chem 0.1ºx0.1º	Satellite-derived 2ºx2.5º	Satellite-derived 0.1ºx0.1º
Asia Pacific, High Income	16	18	13	15
Asia				
Central	24	24	15	16
East	45	48	50	54
South	30	32	29	31
Southeast	13	14	13	14
Australasia	5.4	6.5	3.1	3.5
Caribbean	7.6	7.7	8.1	8.2
Europe				
Central	24	24	16	16
Eastern	17	18	9.9	10
Western	18	19	16	17
Latin America				
Andean	5.3	5.6	7.1	7.4
Central	7.1	7.1	11	11
Southern	8.5	10	5.7	6.6
Tropical	8	8.4	3.7	3.9
North Africa/ Middle East	46	46	24	24
North America, High Income	13	14	10	11
Oceania	1.5	1.5	4.7	4.8
Sub-Saharan Africa	22	22	12	12
Central				
Eastern	21	21	10	10
Southern	9.8	10	6	6.1
Western	95	95	23	23

S-2 GEOS-Chem and its adjoint

In this study, we calculated the sensitivity of global premature mortality to $PM_{2.5}$ precursor emissions using an open-source 3D chemical transport model, GEOS-Chem, and its adjoint. The

forward model takes calculated emissions, assimilated meteorology, and information about chemical and photochemical reactions in the atmosphere to compute hourly atmospheric concentrations of 72 chemical families. The adjoint model is an auxiliary set of equations which allow the calculation of the derivatives of a scalar function of the model output to model input conditions, i.e., initial state or emissions.

For the forward model, we used version 8-02-01 of GEOS-Chem driven by assimilated meteorology from the Goddard Earth Observation System (GEOS-5) of the NASA Global Modeling and Assimilation Office (GMAO), averaged to 2ºx2.5º and 47 vertical levels. The thickness of the lowest layer is approximately 60 m. The model timesteps are 15 minutes for transport and 60 minutes for chemistry and emissions.

The GEOS-Chem aerosol simulation includes the sulphate-nitrate-ammonium system*(1)*, primary carbonaceous aerosols *(2)*, mineral dust *(3)* and sea salt*(4)*. The adjoint model version that we used does not include secondary organic aerosol. Aerosol thermodynamics, including sulphate-nitrate-ammonia chemistry and partitioning, are performed by the RPMARES module*(5)* as implemented by*(6)*. We corrected errors in the nighttime boundary layer mixing and overproduction of HNO_3 following Heald et al. *(7)*. Aerosol dry deposition is based on a size-segregated parametrization described by Zhang et al. *(8)* and wet deposition is treated by an ensemble of wet scavenging processes described in Liu et al. *(9)*. We used a fixed organic matter to organic carbon ratio of 1.8.

Anthropogenic emissions are based on a combination of global and regional inventories. Global monthly emissions for anthropogenic NO_x and SO_2 are from the EDGAR 3.2 inventories for the year 2000*(10)* and scaled to 2005 based on economic data, following van Donkelaar et al. *(11)*. Anthropogenic NH_3 inventories are from the GEIA inventory *(12)* with seasonal variation

implemented by Fisher et al. *(13)*. These global inventories are overwritten by national inventories for the U.S. (NEI2005), Canada (CAC), Mexico (BRAVO), Europe (EMEP) and East Asia*(14, 15)*. Asian NH_3 emissions were scaled to 70% as recommended by Huang et al. *(16)*. Monthly biomass burning emissions are from the GFED2 inventory*(17)*. Biofuel inventories are from Yevich and Logan*(18)*. Black carbon and organic carbon inventories are based on Bond et al. *(19)*, scaled to 2005 as described by Leibensperger et al. *(20)*.

Particulate matter concentrations reported by GEOS-Chem have been extensively evaluated by comparison with surface monitors *(7, 21-24)*, in situ aircraft measurements*(11, 13, 25, 26)*, and satellite observations *(21, 27-30)*. We calculated particle water content at 35% relative humidity to match the U.S. EPA reference method (http://www.epa.gov/ttnamti1/pmfrm.html).

For this study, we used version 35 of the adjoint. The full adjoint of GEOS-Chem including gas-phase chemistry, heterogeneous chemistry, and aerosol thermodynamics is described by Henze et al. *(31)*. Further refinements to the adjoint are described by Henze et al. *(32)*. The adjoint has been applied to a variety of aerosol chemistry studies*(32-36)*.

S-3 Evaluation of speciated model concentrations

For the adjoint method to provide realistic sensitivities, it is important that the model presents accurate concentrations. The method combining the GEOS-Chem model concentrations with satellite AOD has recently been evaluated against a suite of speciated $PM_{2.5}$ concentrations from global surface monitors *(37)*. Since the model version used in this study is different from that used by Philip et al. *(37)*, in Figure S-1 we evaluate the annual $PM_{2.5}$ concentrations in this study versus the surface monitor values collected by Philip et al. *(37)*. Correlation coefficients range from 0.67 for NO_3^- to 0.91 for SO_4^{2-} and slopes range from 0.46 for organic matter to 1.4 for

NO_3^-, which are similar values to those found globally by Philip et al. *(37)*. This provides confidence that the results of this study are based on realistic surface concentrations.

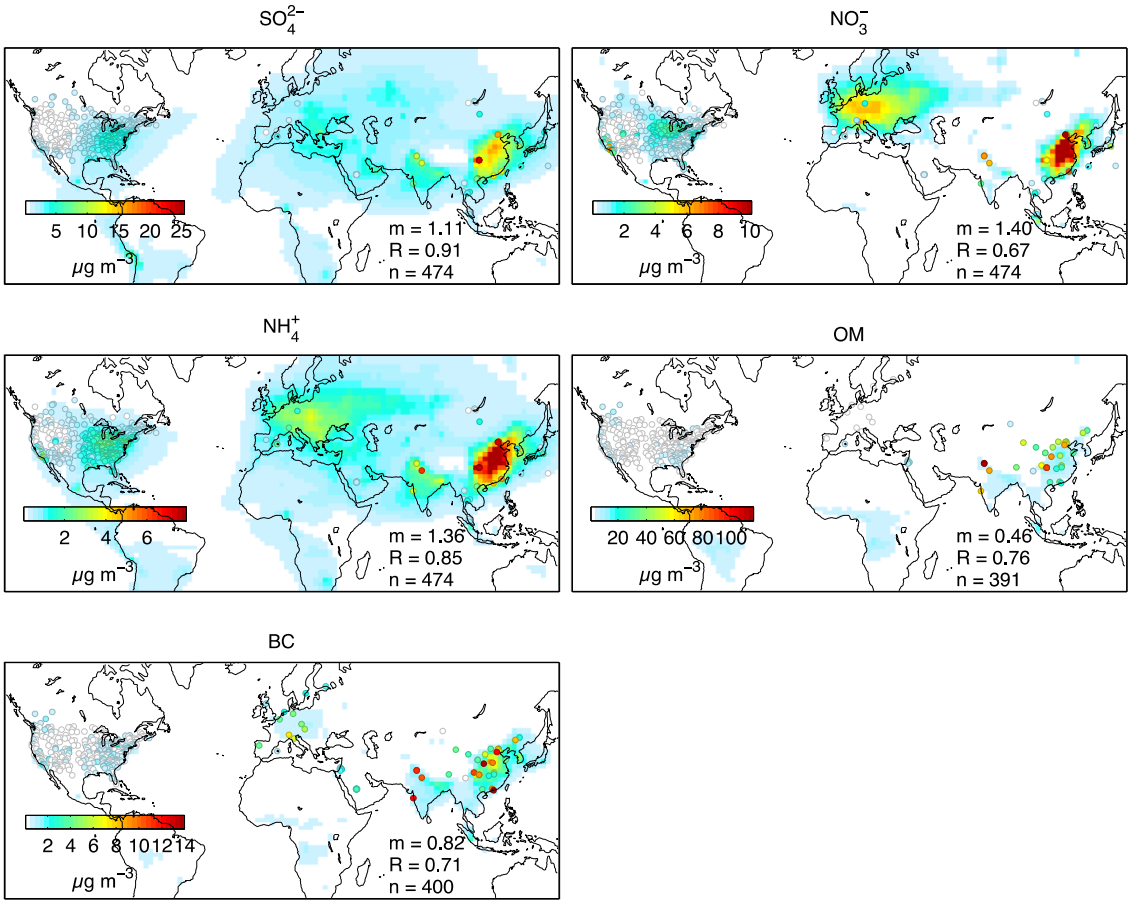

Figure S-1: Comparison of annual mean satellite-derived $PM_{2.5}$ concentrations (background colors) used in this study versus global surface $PM_{2.5}$ monitoring data (filled circles) with Pearson R and slope calculated by organic regression with a 0 y-intercept. These maps were generated using MATLAB and Mapping Toolbox Release 2013a, The MathWorks, Inc., Natick, Massachusetts, United States.

S-4 Model Emissions for 2005

Table S-2: Model emissions in each of 21 GBD regions for the year 2005. BC & OM represent primary carbonaceous aerosols from fossil fuel, biomass, and biofuel combustion.

Region	kg NH_3 / km^2	kg NO / km^2	kg SO_2 / km^2	kg BC / km^2	kg OM / km^2
Asia Pacific, High Income	410	3200	970	290	320
Asia					
Central	110	150	200	13	16
East	880	1100	1300	130	150
South	1100	680	670	100	130
Southeast	210	420	240	150	170
Australasia	66	130	110	10	19
Caribbean	110	92	120	18	23
Europe					
Central	790	1600	1600	100	120
Eastern	110	240	180	14	16
Western	460	970	260	47	51
Latin America					
Andean	120	140	400	34	37
Central	290	340	400	44	54
Southern	240	200	360	21	25
Tropical	250	140	84	75	80
North Africa/ Middle East	110	270	220	12	15
North America, High Income	130	700	200	37	44
Oceania	16	5	3	2	2
Sub-Saharan Africa					
Central	35	15	28	130	220
Eastern	210	17	54	74	140
Southern	110	350	300	34	39
Western	110	49	48	36	110

S-5 Cost function

In order to calculate sensitivity of global $PM_{2.5}$-related mortality to precursor emissions, a cost function which relates $PM_{2.5}$ concentrations to premature mortality is required. The main text presented simplified versions of the equations in the interest of readability. Here we provide the full set of equations for the cost function with subscripts retained. Global mortality, M, was summed by cause and country:

$$M = \sum_{l} \left(\sum_{k} \left(P_k \times M_{0,k,l} \times \mathrm{AF}_{k,l} \right) \right) \quad (1)$$

where l is the cause (IHD, stroke, COPD or LC), k is the country, P_k is the population of country k, $M_{0,k,l}$ is the baseline mortality rate in country k from cause l and $\mathrm{AF}_{k,l}$ is the attributable fraction of deaths from cause l in country k:

$$\mathrm{AF}_{k,l} = 1 - \frac{1}{\overline{\mathrm{RR}_{k,l}}} \quad (2)$$

where $\overline{\mathrm{RR}_{k,l}}$ is the population-weighted average relative risk for cause l in country k:

$$\overline{\mathrm{RR}_{k,l}} = \sum_{i,j \in k} \frac{P_{i,j}}{\sum_{i,j \in k} P_{i,j}} \times \mathrm{RR}_{i,j,l} \quad (3)$$

where i and j are 0.1ºx0.1º grid indices, $P_{i,j}$ is the population in grid cell i,j, and $RR_{i,j,l}$ is the relative risk based on the assumption of 100% exposure at the $PM_{2.5}$-concentration level of grid cell i,j:

$$RR_{i,j,l} = \begin{cases} 1 + a_l \left(1 - e^{-b_l \left(x_{i,j} - x_{0,l}\right)^{r_l}}\right) & \text{if } x_{i,j} > x_{0,l} \\ 1 & \text{otherwise} \end{cases} \quad (4)$$

where α_l, β_l, and ρ_l are the HIF parameters for cause l and $x_{0,l}$ is the counterfactual concentration for cause l.

$x_{i,j}$ is calculated by rescaling the 2ºx2.5º resolution values ($X_{I,J}$) to the satellite values ($sat_{i,j}$) at 0.1ºx0.1º resolution.

$$x_{i,j} = X_{I,J} \frac{sat_{i,j}}{SAT_{I,J}} \frac{SAT_{I,J}}{X_{I,J}} = sat_{i,j} \quad (5)$$

where $SAT_{I,J}$ are the satellite values averaged to 2ºx2.5º resolution. These rescaling factors are then treated as constants in calculating the adjoint forcing terms.

S-6 Integrated Exposure Response Parameters

This study built upon the work of the Global Burden of Disease Project by using the recently developed Integrated Exposure Response (IER) functions to relate $PM_{2.5}$ concentrations to health impacts over a wide range of concentrations *(38)*. Burnett et al. *(38)* used a statistical approach to evaluate these impacts. The adjoint model requires a differentiable equation as its cost function. To that end, we fit IER curves to the median of the suite of IER functions used in the GBD project. Each curve takes the form

$$RR = \begin{cases} 1 + \alpha\left(1 - e^{-\beta(x - x_0)^{\rho}}\right), & \text{if } x > x_0 \\ 1, & \text{otherwise} \end{cases} \quad (6)$$

Specific values are given in Table S-3 and the graphs of these curves are showed in Figure S-2.

Table S-3: Fit parameters based on median GBD IER data.

	IHD	**Stroke**	**COPD**	**LC**
α	0.843	1.01	18.3	159

β	0.0724	0.0164	0.000932	0.000119
ρ	0.544	1.14	0.682	0.735
x_0	6.96	8.38	7.17	7.24

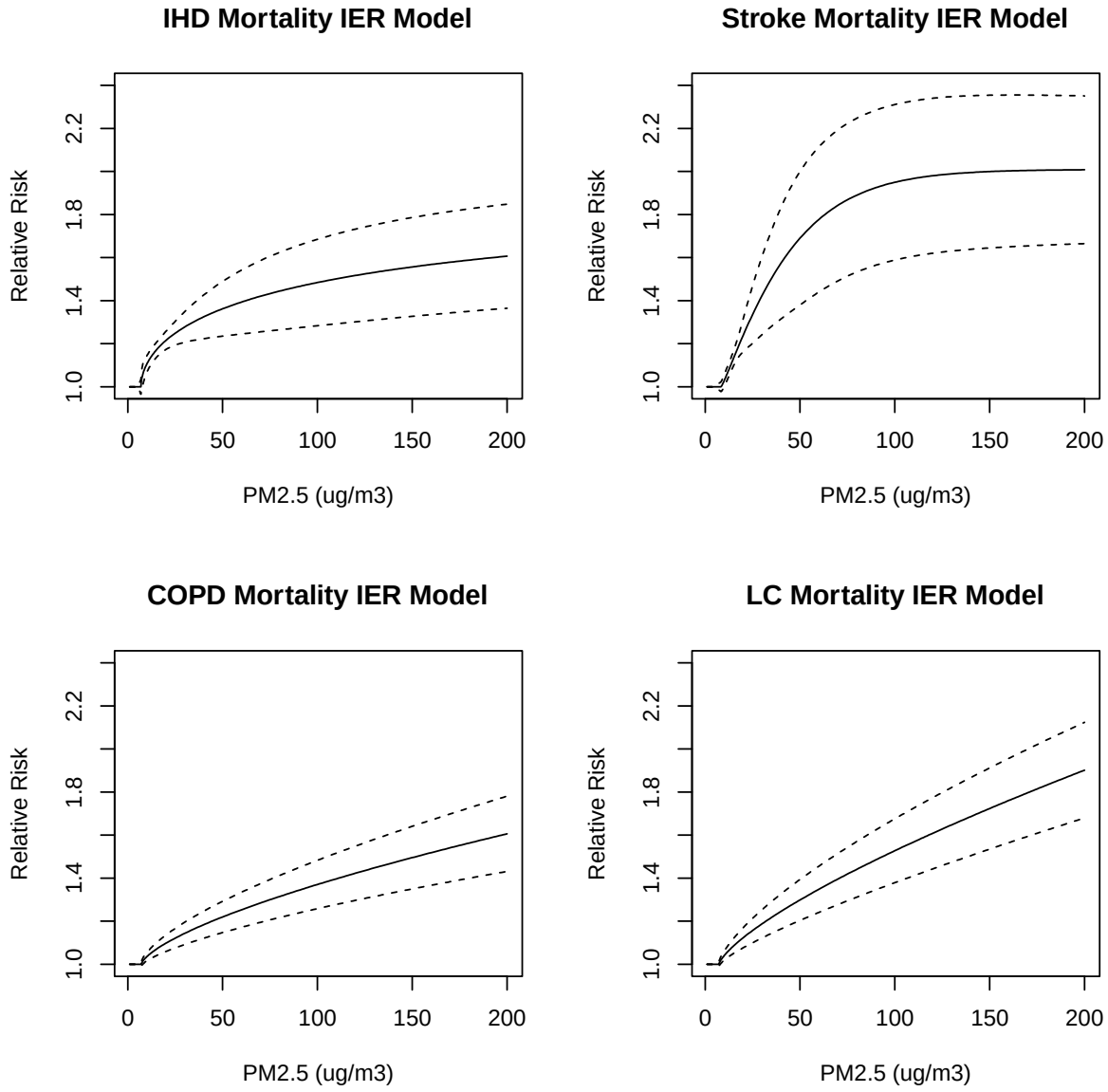

Figure S-2: The relative risk cuves used in this study versus ambient $PM_{2.5}$ concentration.

S-7 Evaluation of adjoint responses

We performed 1-week finite difference tests to evaluate how well the linearity assumption of the adjoint holds for the conditions of this study. Whereas the adjoint reports the instantaneous derivative of mortality to emissions, a finite difference test approximates this derivative as the slope over a finite range.

We ran the forward model in its default state and with perturbed emissions for one species (n) in one GEOS-Chem grid cell (I,J) (with a perturbation, δ, of 10%). The cost function (J) was calculated for each of these runs and the sensitivity was approximated as:

$$\frac{\partial \mathrm{J}}{\partial p_{I,J,n}} \approx \frac{\Delta \mathrm{J}}{\delta_{I,J,n}} \qquad \text{Eq 1}$$

where p is the scaling factor of emission n, making $\frac{\partial \mathrm{J}}{\partial p_{I,J,n}}$ the sensitivity of the cost function with respect to emissions scaling factor.

In the ideal case where the cost function is completely linear with respect to the emissions, the sensitivities estimated using the finite difference method will be exactly equal to the adjoint sensitivities. In this way, a finite difference test can act as an indicator of the non-linearity of the response of the cost function to changes in emissions. We performed this comparison in 10 locations for each of 5 emissions types.

Figure S-3 shows the results of finite difference tests performed at 10 locations compared with adjoint sensitivities from those locations. The finite difference tests yielded a linear fit between the adjoint and finite difference sensitivities and small spread between the positive and negative finite-difference tests.

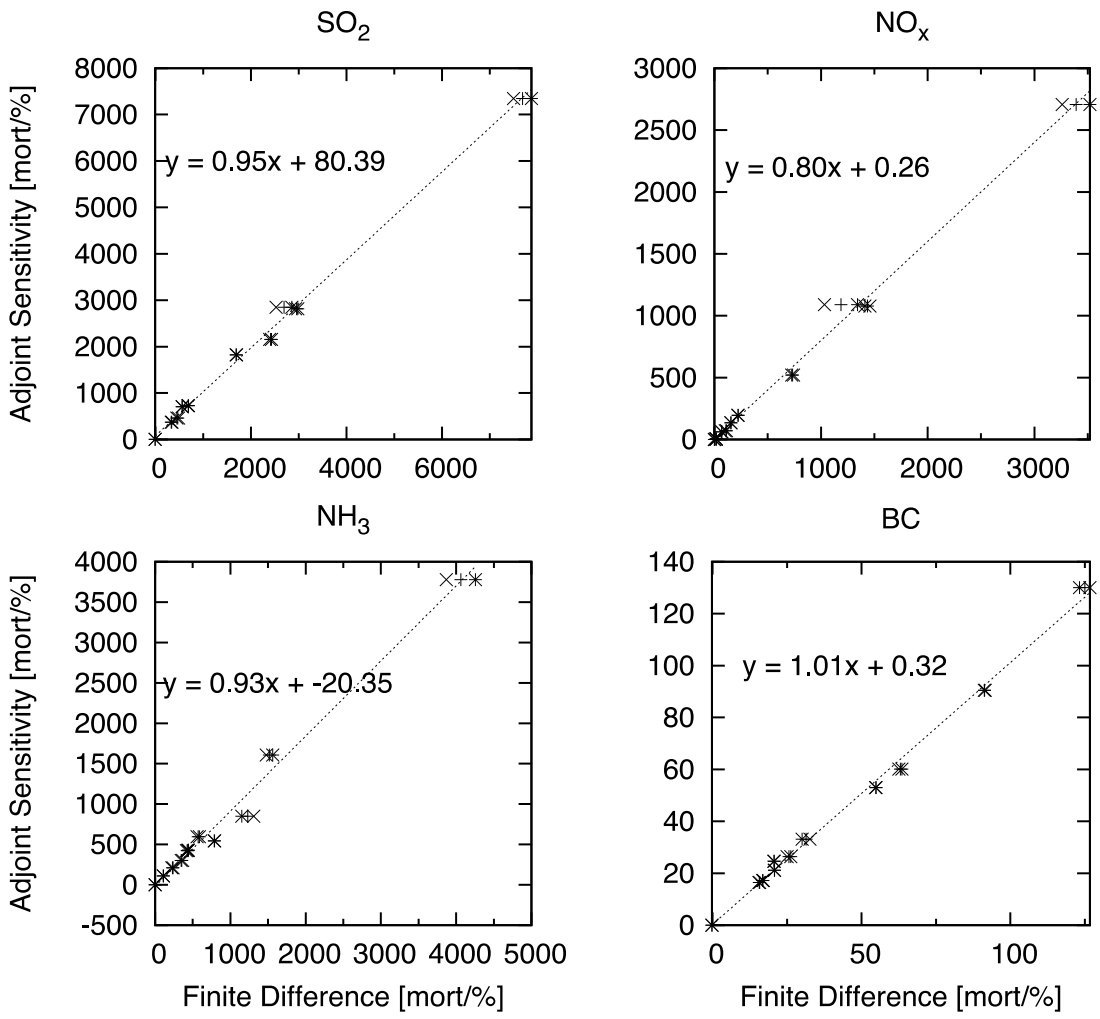

Figure S-3: Finite difference test for 4 species at selected locations; sensitivities reported by the adjoint vs. finite-difference sensitivities. X indicates positive finite difference (i.e., $\delta=+0.1$), * represents negative finite difference ($\delta=-0.1$) and + represents two-way finite difference test. Regression line is for adjoint vs. 2-way finite difference.

S-8 Uncertainty analysis

The major sources of uncertainty in calculating the responses of premature mortality to precursor emissions are the relative-risk calculated by the health-impact function, satellite-derived $PM_{2.5}$ concentrations, and the simulation of the source-receptor relationship. We used propagation of error to calculate uncertainties (σ_λ) in the responses (λ):

$$\sigma_\lambda^2 = \left|\frac{\partial \lambda}{\partial RR_{\mathrm{COPD}}}\right|^2 \sigma_{\mathrm{RR_{COPD}}}^2 + \left|\frac{\partial \lambda}{\partial RR_{\mathrm{IHD}}}\right|^2 \sigma_{\mathrm{RR_{IHD}}}^2 + \left|\frac{\partial \lambda}{\partial RR_{\mathrm{LC}}}\right|^2 \sigma_{\mathrm{RR_{LC}}}^2 + \left|\frac{\partial \lambda}{\partial RR_{\mathrm{stroke}}}\right|^2 \sigma_{\mathrm{RR_{stroke}}}^2 + \left|\frac{\partial \lambda}{\partial \mathrm{PM_{2.5}}}\right|^2 \sigma_{\mathrm{PM_{2.5}}}^2 + \left|\frac{\partial \lambda}{\partial G}\right|^2 \sigma_G^2 \quad (6)$$

where the partial derivatives, except in the case of the model parameters *G*, in Eq 6 were estimated by finite difference, using the magnitudes of the uncertainties as the finite differences. We calculated the partial derivatives by subtracting the responses of the base run of the model from the responses produced by running the model with each parameter perturbed by one standard deviation (σ).

To obtain σ_{RR}, we used the 1-standard-deviation of the GBD *RR* data from the Monte-Carlo output of Burnett et al. (2014). We took $\sigma_{PM_{2.5}}$ to be 30%, informed by the comparison of satellite-derived $PM_{2.5}$ versus individual ground-based monitors and propagation of error in *(21)*. Since there are many uncertain parameters within the model, finding the contribution of the source-receptor relationship to the uncertainties is not straightforward *(39)*. We chose a sensitivity $\left|\frac{\partial \lambda}{\partial G}\right|$ = 1and parameter uncertainty $\sigma_G = 40\%$ to represent these uncertainties. We assumed that population and mortality data were more accurately known and that uncertainties in these two data sources would be outweighed by uncertainties in the exposure data and especially the exposure response.

The 1-standard-deviation of uncertainties in the individual responses displayed a similar spatial pattern to the modeled responses and was typically 40-120% of the sensitivities. The main contributor to uncertainty in the sensitivities was from $PM_{2.5}$ concentrations; considering uncertainties through propagation of errors in the $PM_{2.5}$ concentrations alone resulted in global population-weighted average uncertainties ranging from 42% for organic matter to 120% for NO_x. Uncertainties in the *RR* parameters also contributed significantly with global population-weighted average uncertainties from 21% to 59% for CEV and 13% to 38% for IHD.

S-9 Global responses by GBD region

Figure S-4 and Figure S-5 show the same results as in Table 1 and Table 2 form the main text as a column chart.

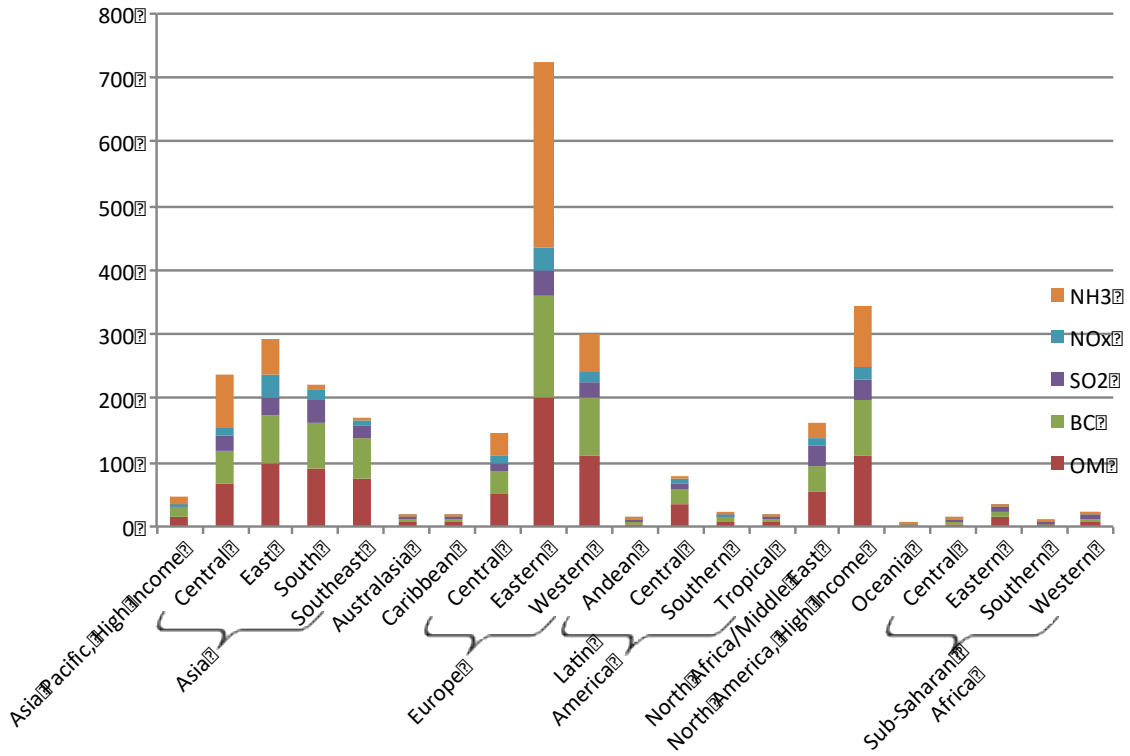

Figure S-4: Global responses to absolute changes in regional emissions. Annual global premature mortalities prevented by reducing emissions by 1 kg km^{-2} yr^{-1} in each of 21 GBD regions.

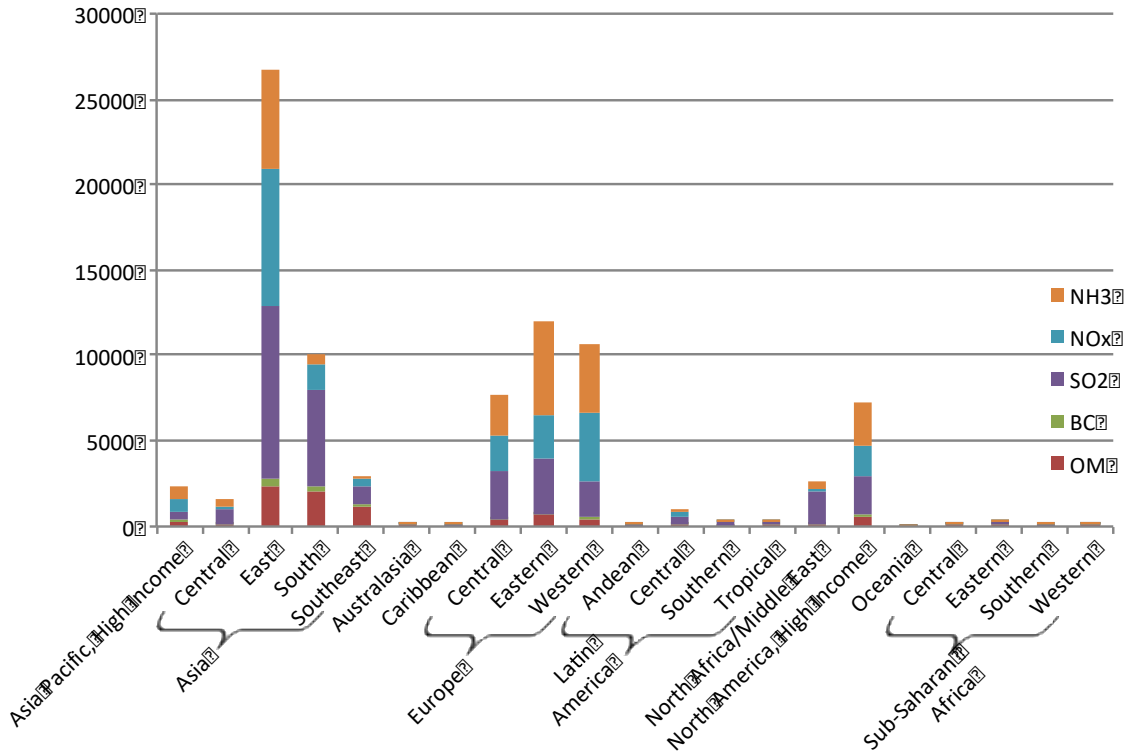

Figure S-5: Global responses to relative changes in regional emissions. Annual global premature mortalities prevented by reducing emissions by 10% in each of 21 GBD regions.

S-10 Ranking of top contributing regions to global mortality

Table S-4 shows the top 5 regions for responses of global mortality to changes in precursor emissions.

Table S-4: Rankings of top 5 regions by population, response to relative (10%) changes in emissions, and response to absolute (1 kg km^{-2} yr^{-1}) changes in emissions.

	Rank	1st	2nd	3rd	4th	5th
	Pop	South Asia	East Asia	Southeast Asia	Western Europe	North Africa/ Middle East
Relative (10%)	**NH_3**	East Asia	Eastern Europe	Western Europe	High-income North America	Central Europe
	NO_x	East Asia	Western Europe	Eastern Europe	Central Europe	High-income North America
	SO_2	East Asia	South Asia	Eastern Europe	Central Europe	Western Europe
	BC	East Asia	South Asia	Southeast Asia	High-income North America	Western Europe
	OM	East Asia	South Asia	Southeast Asia	Eastern Europe	High-income North America
Absolute (1 kg km^{-2} yr^{-1})	**NH_3**	Eastern Europe	High-income North America	Central Asia	Western Europe	East Asia
	NO_x	East Asia	Eastern Europe	High-income North America	South Asia	Western Europe
	SO_2	Eastern Europe	South Asia	High-income North America	North Africa/ Middle East	East Asia
	BC	Eastern Europe	Western Europe	High-income North America	East Asia	South Asia
	OM	Eastern Europe	Western Europe	High-income North America	East Asia	South Asia

References

1. Park, R. J.; Jacob, D. J.; Kumar, N.; Yantosca, R. M. Regional visibility statistics in the United States: Natural and transboundary pollution influences, and implications for the Regional Haze Rule. *Atmos. Environ.* **2006***, 40*, 5405-5423.

2. Park, R.; Jacob, D.; Chin, M.; Martin, R. Sources of carbonaceous aerosols over the United States and implications for natural visibility. *Journal of Geophysical Research: Atmospheres* **2003***, 108*.

3. Fairlie, T. D.; Jacob, D. J.; Park, R. J. The impact of transpacific transport of mineral dust in the United States. *Atmos. Environ.* **2007***, 41*, 1251-1266.

4. Alexander, B.; Park, R.; Jacob, D.; Li, Q.; Yantosca, R.; Savarino, J.; Lee, C.; Thiemens, M. Sulfate formation in sea-salt aerosols: Constraints from oxygen isotopes. *Journal of Geophysical Research: Atmospheres* **2005***, 110*.

5. Binkowski, F. S.; Roselle, S. J. Models-3 Community Multiscale Air Quality (CMAQ) model aerosol component 1. Model description. *Journal of Geophysical Research: Atmospheres* **2003***, 108*, n/a-n/a.

6. Park, R. J.; Jacob, D. J.; Field, B. D.; Yantosca, R. M.; Chin, M. Natural and transboundary pollution influences on sulfate-nitrate-ammonium aerosols in the United States: Implications for policy. *Journal of Geophysical Research: Atmospheres* **2004***, 109*, n/a-n/a.

7. Heald, C. L.; Collett, J.,J.L.; Lee, T.; Benedict, K. B.; Schwandner, F. M.; Li, Y.; Clarisse, L.; Hurtmans, D. R.; Van Damme, M.; Clerbaux, C.; Coheur, P. -.; Philip, S.; Martin, R. V.; Pye, H. O. T. Atmospheric ammonia and particulate inorganic nitrogen over the United States. *Atmospheric Chemistry and Physics* **2012***, 12*, 10295-10312.

8. Zhang, L.; Gong, S.; Padro, J.; Barrie, L. A size-segregated particle dry deposition scheme for an atmospheric aerosol module. *Atmos. Environ.* **2001***, 35*, 549-560.

9. Liu, H.; Jacob, D. J.; Bey, I.; Yantosca, R. M. Constraints from 210Pb and 7Be on wet deposition and transport in a global three-dimensional chemical tracer model driven by assimilated meteorological fields. *Journal of Geophysical Research: Atmospheres* **2001***, 106*, 12109-12128.

10. Olivier, J. G. J.; Van Aardenne, J. A.; Dentener, F. J.; Pagliari, V.; Ganzeveld, L. N.; Peters, J. A. H. W. Recent trends in global greenhouse gas emissions:regional trends 1970--2000 and spatial distributionof key sources in 2000. *Environmental Sciences* **2005***, 2*, 81-99.

11. van Donkelaar, A.; Martin, R. V.; Leaitch, W. R.; Macdonald, A. M.; Walker, T. W.; Streets, D. G.; Zhang, Q.; Dunlea, E. J.; Jimenez, J. L.; Dibb, J. E.; Huey, L. G.; Weber, R.; Andreae, M. O. Analysis of aircraft and satellite measurements from the Intercontinental Chemical Transport Experiment (INTEX-B) to quantify long-range transport of East Asian sulfur to Canada. *Atmospheric Chemistry and Physics* **2008***, 8*, 2999-3014.

12. Bouwman, A. F.; Lee, D. S.; Asman, W. A. H.; Dentener, F. J.; Van Der Hoek, K. W.; Olivier, J. G. J. A global high-resolution emission inventory for ammonia. *Global Biogeochem. Cycles* **1997***, 11*, 561-587.

13. Fisher, J. A.; Jacob, D. J.; Wang, Q.; Bahreini, R.; Carouge, C. C.; Cubison, M. J.; Dibb, J. E.; Diehl, T.; Jimenez, J. L.; Leibensperger, E. M.; Lu, Z.; Meinders, M. B. J.; Pye, H. O. T.; Quinn, P. K.; Sharma, S.; Streets, D. G.; Donkelaar, A. v.; Yantosca, R. M. Sources, distribution, and acidity of sulfate--ammonium aerosol in the Arctic in winter--spring. *Atmos. Environ.* **2011***, 45*, 7301.

14. Streets, D. G.; Bond, T. C.; Carmichael, G. R.; Fernandes, S. D.; Fu, Q.; He, D.; Klimont, Z.; Nelson, S. M.; Tsai, N. Y.; Wang, M. Q.; Woo, J. -.; Yarber, K. F. An inventory of gaseous and

primary aerosol emissions in Asia in the year 2000. *Journal of Geophysical Research: Atmospheres* **2003***, 108*, 8809.

15. Streets, D. G.; Q. Zhang; L. Wang; K. He; J. Hao; Y. Wu; Y. Tang; G.C. Carmichael Revisiting China's CO emissions after the Transport and Chemical Evolution over the Pacific (TRACE-P) mission: Synthesis of inventories, atmospheric modeling, and observations. *Journal of Geophysical Research: Atmospheres* **2006***, 111*.

16. Huang, X.; Song, Y.; Li, M.; Li, J.; Huo, Q.; Cai, X.; Zhu, T.; Hu, M.; Zhang, H. A high-resolution ammonia emission inventory in China. *Global Biogeochem. Cycles* **2012***, 26*.

17. van der Werf, G.; Morton, D.; DeFries, R.; Giglio, L.; Randerson, J.; Collatz, G.; Kasibhatla, P. Estimates of fire emissions from an active deforestation region in the southern Amazon based on satellite data and biogeochemical modelling. *Biogeosciences* **2009***, 6*, 235-249.

18. Yevich, R.; Logan, J. An assessment of biofuel use and burning of agricultural waste in the developing world. *Global Biogeochem. Cycles* **2003***, 17*.

19. Bond, T. C.; Bhardwaj, E.; Dong, R.; Jogani, R.; Jung, S.; Roden, C.; Streets, D. G.; Trautmann, N. M. Historical emissions of black and organic carbon aerosol from energy-related combustion, 1850--2000. *Global Biogeochem. Cycles* **2007***, 21*, n/a-n/a.

20. Leibensperger, E. M.; Mickley, L. J.; Jacob, D. J.; Chen, W. -.; Seinfeld, J. H.; Nenes, A.; Adams, P. J.; Streets, D. G.; Kumar, N.; Rind, D. Climatic effects of 1950--2050 changes in US anthropogenic aerosols -- Part 1: Aerosol trends and radiative forcing. *Atmospheric Chemistry and Physics* **2012***, 12*, 3333-3348.

21. van Donkelaar, A.; Martin, R. V.; Brauer, M.; Kahn, R.; Levy, R.; Verduzco, C.; Villeneuve, P. J. Global Estimates of Ambient Fine Particulate Matter Concentrations from Satellite-Based Aerosol Optical Depth: Development and Application. *Environ. Health Perspect.* **2010***, 118*, 847-855.

22. Fu, T. -.; Cao, J. J.; Zhang, X. Y.; Lee, S. C.; Zhang, Q.; Han, Y. M.; Qu, W. J.; Han, Z.; Zhang, R.; Wang, Y. X.; Chen, D.; Henze, D. K. Carbonaceous aerosols in China: top-down constraints on primary sources and estimation of secondary contribution. *Atmospheric Chemistry and Physics* **2012***, 12*, 2725-2746.

23. Walker, T. W.; Jones, D. B. A.; Parrington, M.; Henze, D. K.; Murray, L. T.; Bottenheim, J. W.; Anlauf, K.; Worden, J. R.; Bowman, K. W.; Shim, C.; Singh, K.; Kopacz, M.; Tarasick, D. W.; Davies, J.; von der Gathen, P.; Thompson, A. M.; Carouge, C. C. Impacts of midlatitude precursor emissions and local photochemistry on ozone abundances in the Arctic. *Journal of Geophysical Research: Atmospheres* **2012***, 117*.

24. Zhang, L.; Jacob, D. J.; Knipping, E. M.; Kumar, N.; Munger, J. W.; Carouge, C. C.; van Donkelaar, A.; Wang, Y. X.; Chen, D. Nitrogen deposition to the United States: distribution, sources, and processes. *Atmospheric Chemistry and Physics* **2012***, 12*, 4539-4554.

25. Dunlea, E. J.; DeCarlo, P. F.; Aiken, A. C.; Kimmel, J. R.; Peltier, R. E.; Weber, R. J.; Tomlinson, J.; Collins, D. R.; Shinozuka, Y.; McNaughton, C. S.; Howell, S. G.; Clarke, A. D.; Emmons, L. K.; Apel, E. C.; Pfister, G. G.; van Donkelaar, A.; Martin, R. V.; Millet, D. B.; Heald, C. L.;

Jimenez, J. L. Evolution of Asian aerosols during transpacific transport in INTEX-B. *Atmospheric Chemistry and Physics* **2009***, 9*, 7257-7287.

26. Heald, C. L.; Coe, H.; Jimenez, J. L.; Weber, R. J.; Bahreini, R.; Middlebrook, A. M.; Russell, L. M.; Jolleys, M.; Fu, T. -.; Allan, J. D.; Bower, K. N.; Capes, G.; Crosier, J.; Morgan, W. T.; Robinson, N. H.; Williams, P. I.; Cubison, M. J.; DeCarlo, P. F.; Dunlea, E. J. Exploring the vertical profile of atmospheric organic aerosol: comparing 17 aircraft field campaigns with a global model. *Atmospheric Chemistry and Physics* **2011***, 11*, 12673-12696.

27. Generoso, S.; Bey, I.; Labonne, M.; Breon, F. Aerosol vertical distribution in dust outflow over the Atlantic: Comparisons between GEOS-Chem and Cloud-Aerosol Lidar and Infrared Pathfinder Satellite Observation (CALIPSO). *Journal of Geophysical Research: Atmospheres* **2008***, 113*.

28. Heald, C. L.; Ridley, D. A.; Kreidenweis, S. M.; Drury, E. E. Satellite observations cap the atmospheric organic aerosol budget. *Geophys. Res. Lett.* **2010***, 37*.

29. Johnson, M. S.; Meskhidze, N.; Kiliyanpilakkil, V. P. A global comparison of GEOS-Chem-predicted and remotely-sensed mineral dust aerosol optical depth and extinction profiles. *Journal of Advances in Modeling Earth Systems* **2012***, 4*.

30. Luan, Y.; Jaegle, L. Composite study of aerosol export events from East Asia and North America. *Atmospheric Chemistry and Physics* **2013}***, 13}*, 1221-1242}.

31. Henze, D. K.; Hakami, A.; Seinfeld, J. H. Development of the adjoint of GEOS-Chem. *Atmospheric Chemistry and Physics* **2007***, 7*, 2413-2433.

32. Henze, D. K.; Seinfeld, J. H.; Shindell, D. T. Inverse modeling and mapping US air quality influences of inorganic PM2.5 precursor emissions using the adjoint of GEOS-Chem. *Atmospheric Chemistry and Physics* **2009***, 9*, 5877-5903.

33. Henze, D. K.; Shindell, D. T.; Akhtar, F.; Spurr, R. J. D.; Pinder, R. W.; Loughlin, D.; Kopacz, M.; Singh, K.; Shim, C. Spatially Refined Aerosol Direct Radiative Forcing Efficiencies. *Environmental Science and Technology* **2012***, 46*, 9511-9518.

34. Kharol, S. K.; Martin, R. V.; Philip, S.; Vogel, S.; Henze, D. K.; Chen, D.; Wang, Y.; Zhang, Q.; Heald, C. L. Persistent sensitivity of Asian aerosol to emissions of nitrogen oxides. *Geophys. Res. Lett.* **2013**.

35. Xu, X.; Wang, J.; Henze, D. K.; Qu, W.; Kopacz, M. Constraints on aerosol sources using GEOS-Chem adjoint and MODIS radiances, and evaluation with multisensor (OMI MISR) data. *Journal of Geophysical Research: Atmospheres* **2013***, 118*, 6396-6413.

36. Koo, J.; Wang, Q.; Henze, D. K.; Waitz, I. A.; Barrett, S. R. H. Spatial sensitivities of human health risk to intercontinental and high-altitude pollution. *Atmos. Environ.* **2013***, 71*, 140-147.

37. Philip, S.; Martin, R. V.; van Donkelaar, A.; Lo, J. W.; Wang, Y.; Chen, D.; Zhang, L.; Kasibhatla, P. S.; Wang, S.; Zhang, Q.; Lu, Z.; Streets, D. G.; Bittman, S.; Macdonald, D. J. Global Chemical Composition of Ambient Fine Particulate Matter for Exposure Assessment. *Environ. Sci. Technol.* **2014***, 48*, 13060-13068.

38. Burnett, R. T.; Pope, C. A. I.; Ezzati, M.; Olives, C.; Lim, S. S.; Mehta, S.; Shin, H. H.; Singh, G.; Hubbell, B.; Brauer, M.; Anderson, H. R.; Smith, K. R.; Kan, H.; Laden, F.; Pruess, A.; Turner, M. C.; Thun, M.; Cohen, A. An Integrated Risk Function for Estimating the Global Burden of Disease Attributable to Ambient Fine Particulate Matter Exposure. *Environ. Health Perspect.* **2014***, 122*, 397-403.

39. Cohan, D. S.; Koo, B.; Yarwood, G. Influence of uncertain reaction rates on ozone sensitivity to emissions. *Atmos. Environ.* **2010***, 44*, 3101-3109.

Appendix B

Supporting Information for insights into simulated global aerosol distribution and processes from assimilation of space-based lidar profiles

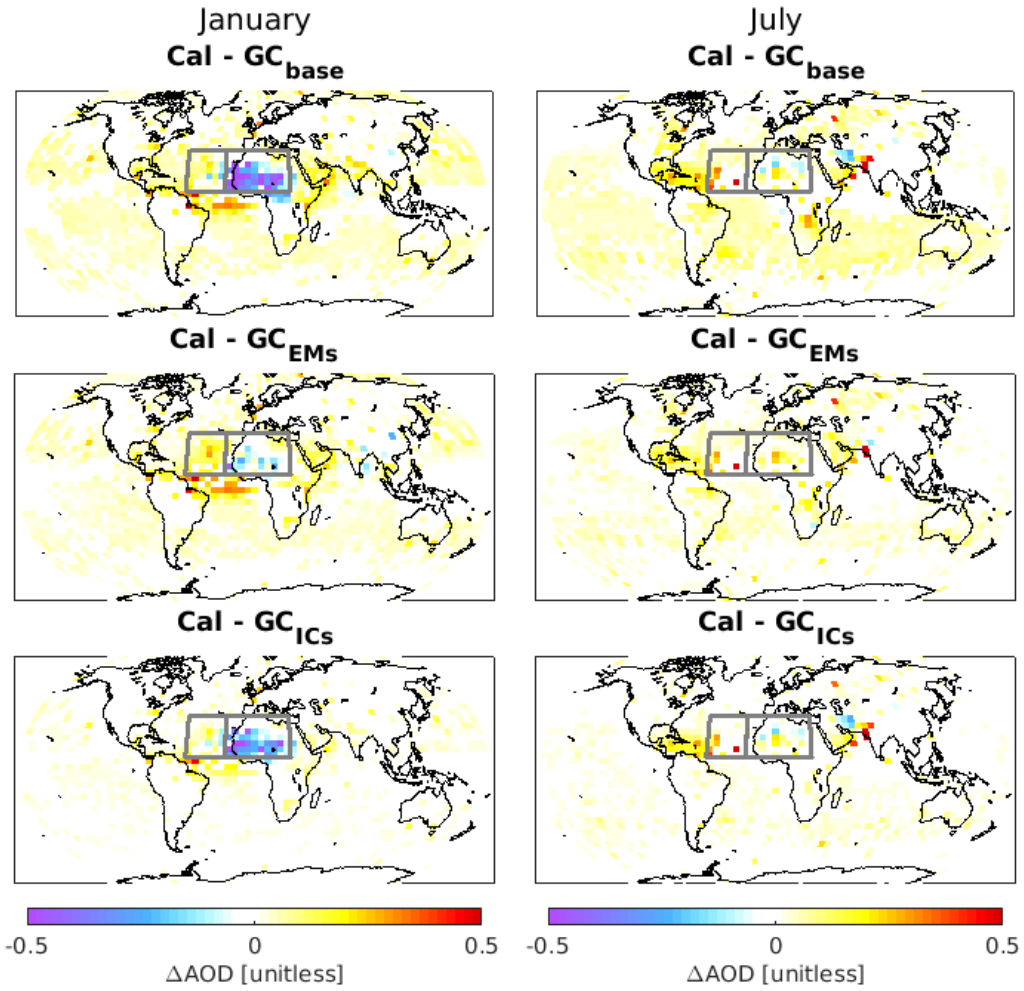

Figure B.1: Difference between CALIOP observed AOD below 2 km and simulated AOD below 2 km from: baseline simulation emissions (top row), 1-month runs with optimised emissions (middle row) and 1-day runs with optimised ICs, coincidently sampled with CALIOP superobservations, for January (left column) and July (right column) of 2007.

Appendix C

Supporting Information for Global Estimation of Ambient Particulate Air Pollution Concentration and Uncertainty Using Mixture Density Networks

Chapter S1 Normalized Relative Sensitivity Figures

Each figure shows the relative sensitivity of the mean PM2.5 predicted by the model to a single covariate, that is, the local relative difference in the mean predicted by the model when the model has been perturbed by plus and minus 10%, divided by the size of the total perturbation range. Latitude and longitude not shown because relative changes in spatial distance are meaningless.

Satellite-derived PM2.5:

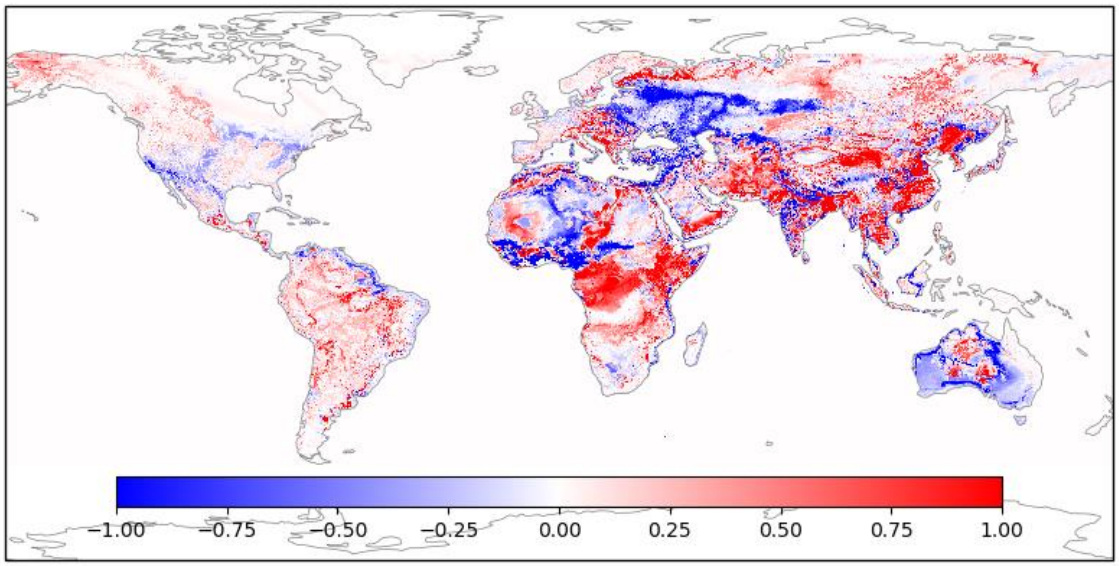

Figure S1-1 Satellite-derived $PM_{2.5}$

Dust fraction:

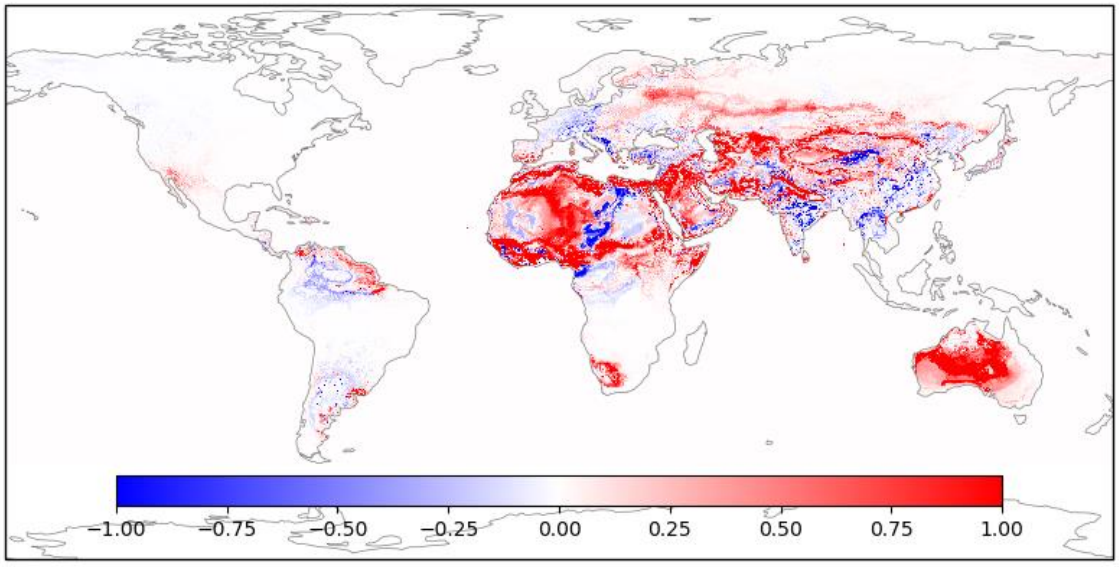

Figure S1-2 Modeled dust fraction

SNAOC fraction:

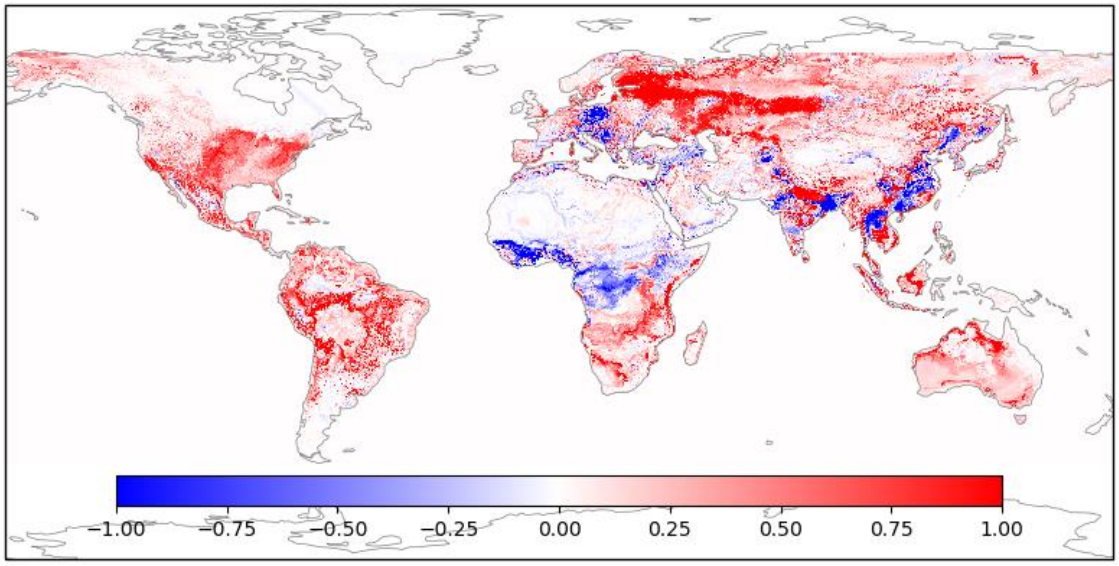

Figure S1-3 Modeled sulphate-nitrate-ammonia-organic carbon fraction

Distance to urban:

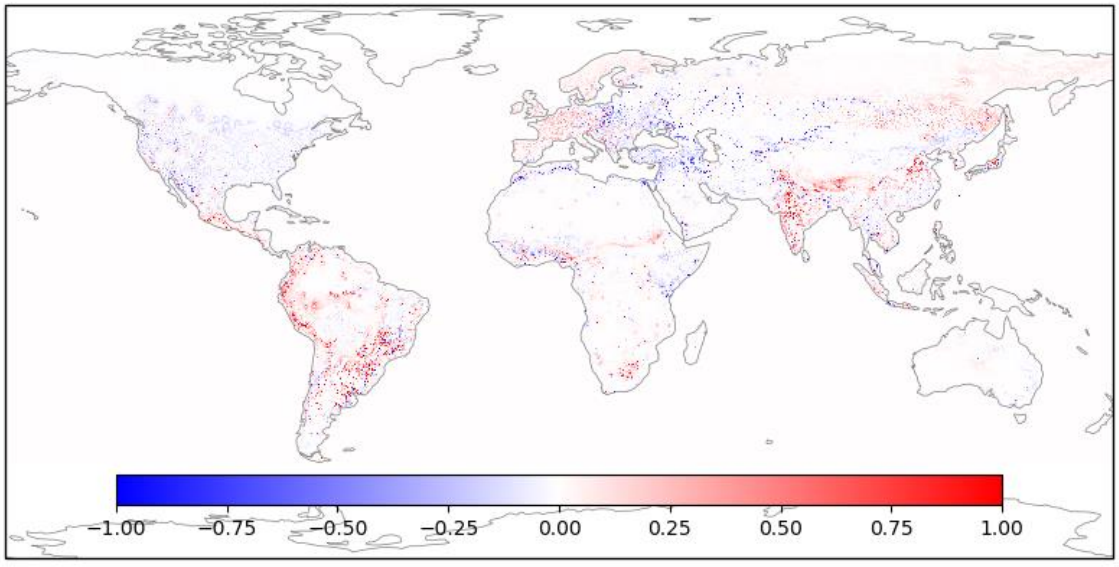

Figure S1-4 Distance to urban land type

Elevation difference w/2°x2.5° grid cell centre:

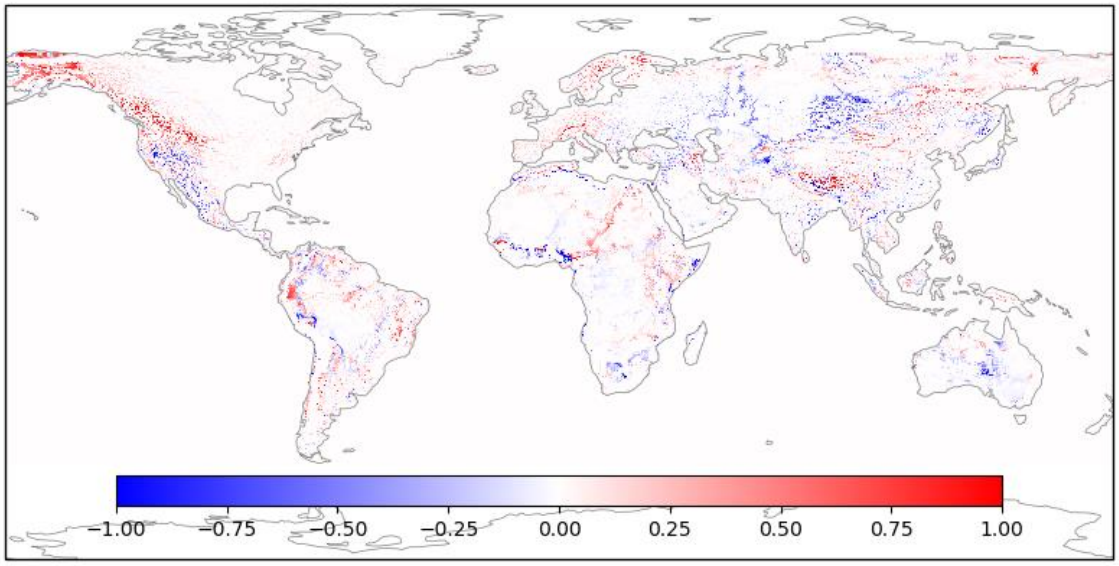

Figure S1-5 Elevation difference between local 0.1° and 2°x2.5° grid cell centre

Chapter S2 Unnormalized Marginal Sensitivity Figures

Each figure shows the sensitivity of the mean PM2.5 predicted by the model to a single covariate, that is, the difference in the mean predicted by the model when the model has been perturbed by plus and minus 10%, divided by the size of the total perturbation range. In the case of lat and long, the perturbation of ±0.05°.

Latitude:

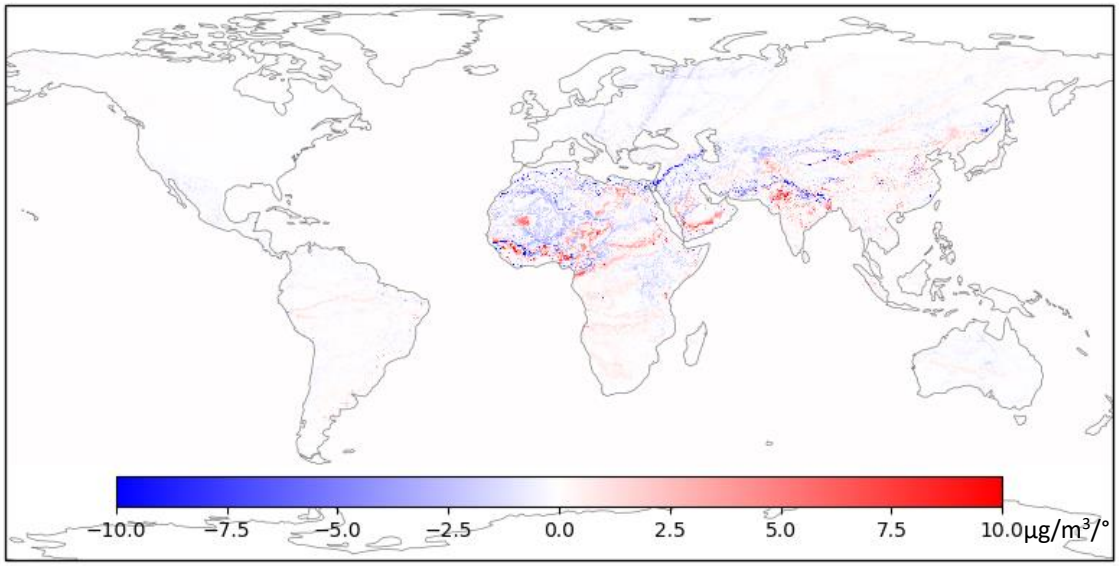

Figure S2-1 Sensitivity of PM with respect to Latitude

Longitude:

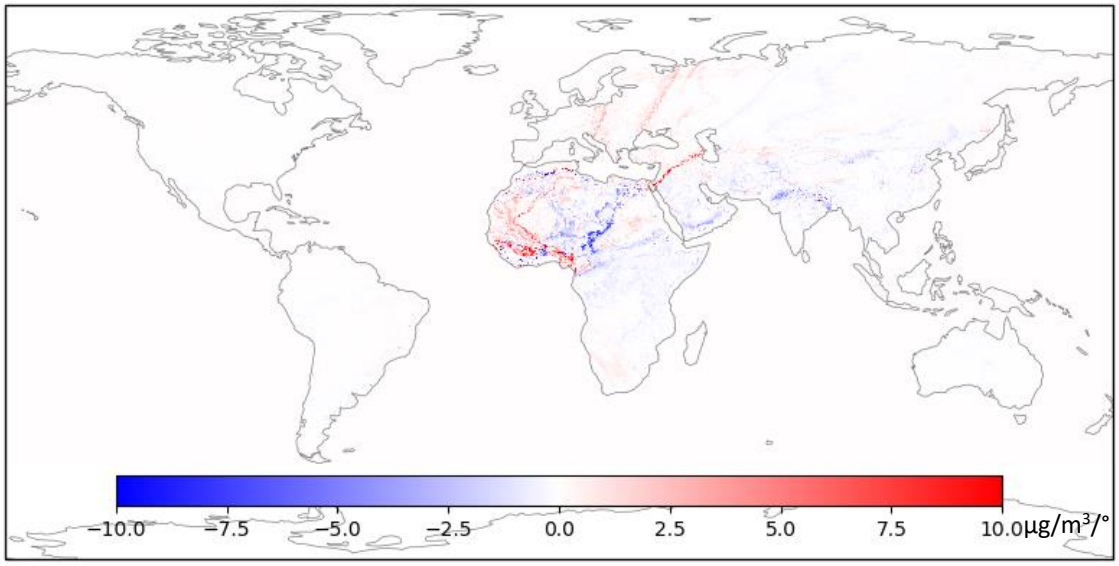

Figure S2-2 Longitude

Satellite-derived PM2.5:

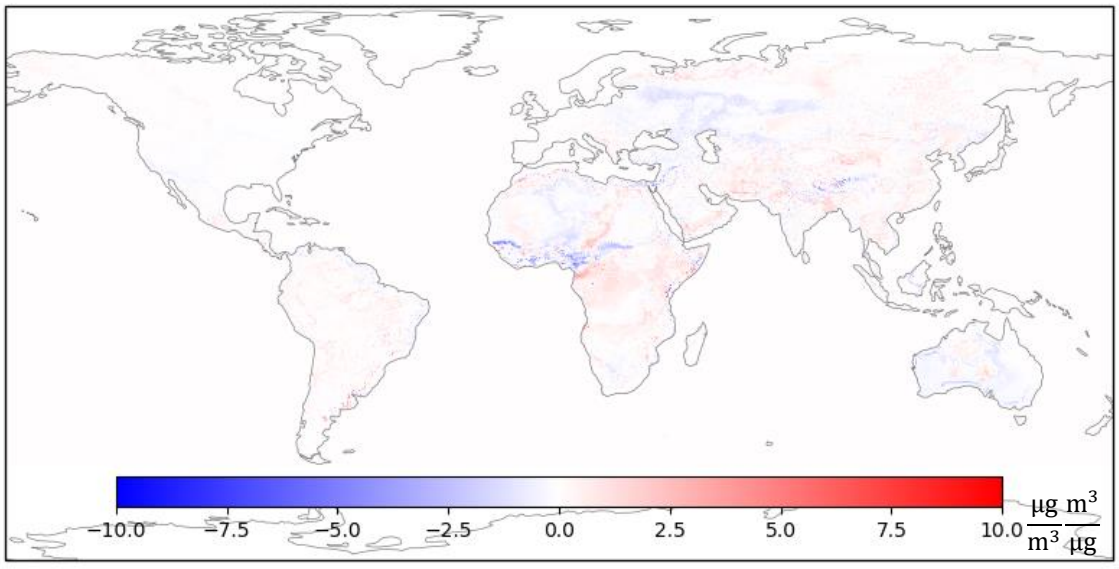

Figure S2-3 Satellite-derived $PM_{2.5}$

Dust fraction:

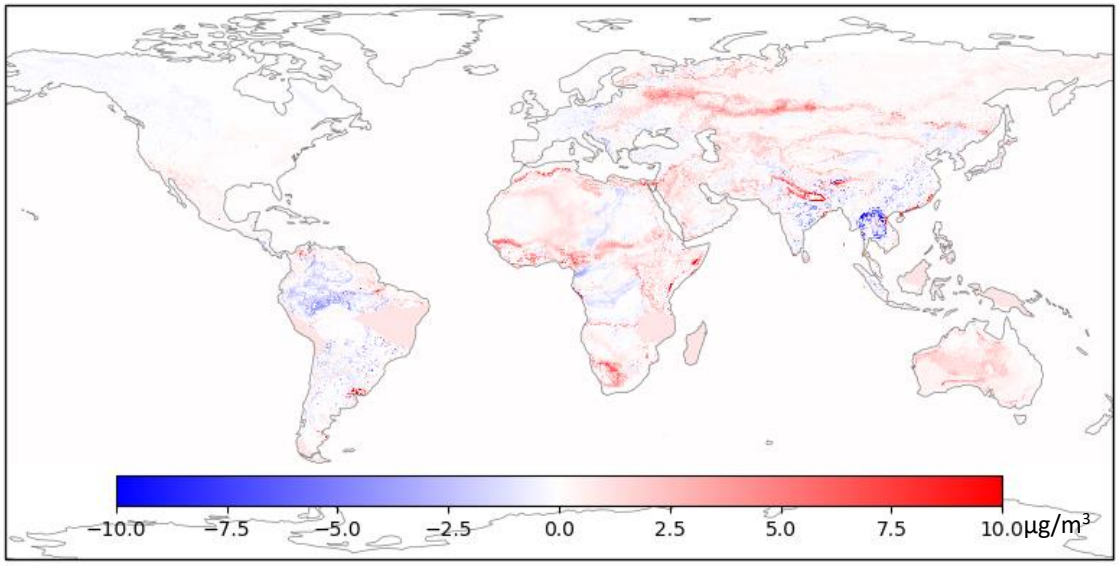

Figure S2-4 Modeled dust fraction

SNAOC fraction:

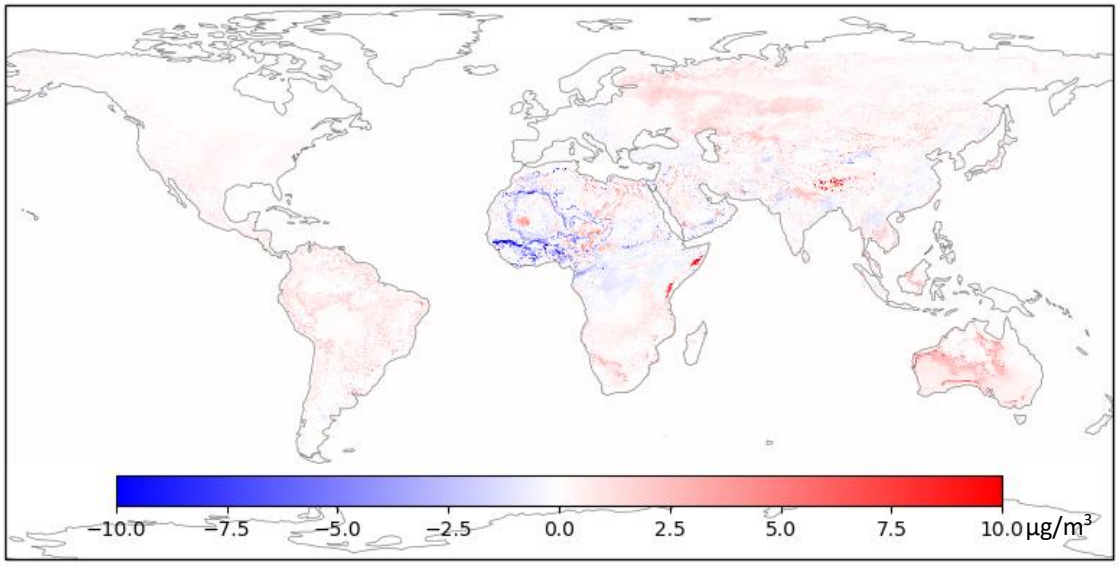

Figure S2-5 Modeled sulphate-nitrate-ammonia-organic carbon fraction

Distance to urban:

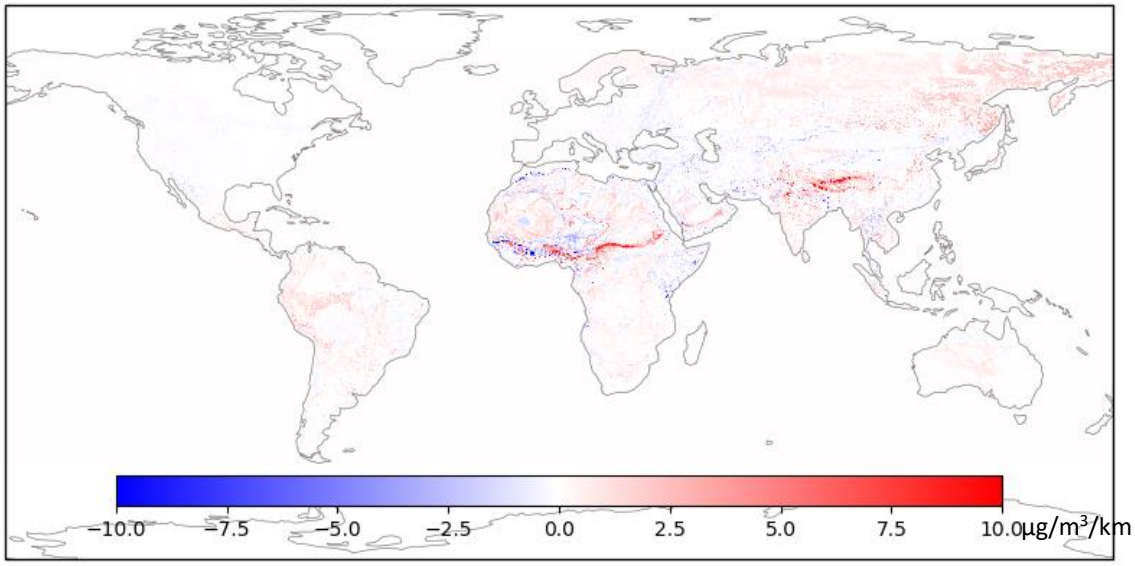

Figure S2-6 Distance to urban land type

Elevation difference w/2°x2.5° grid cell centre:

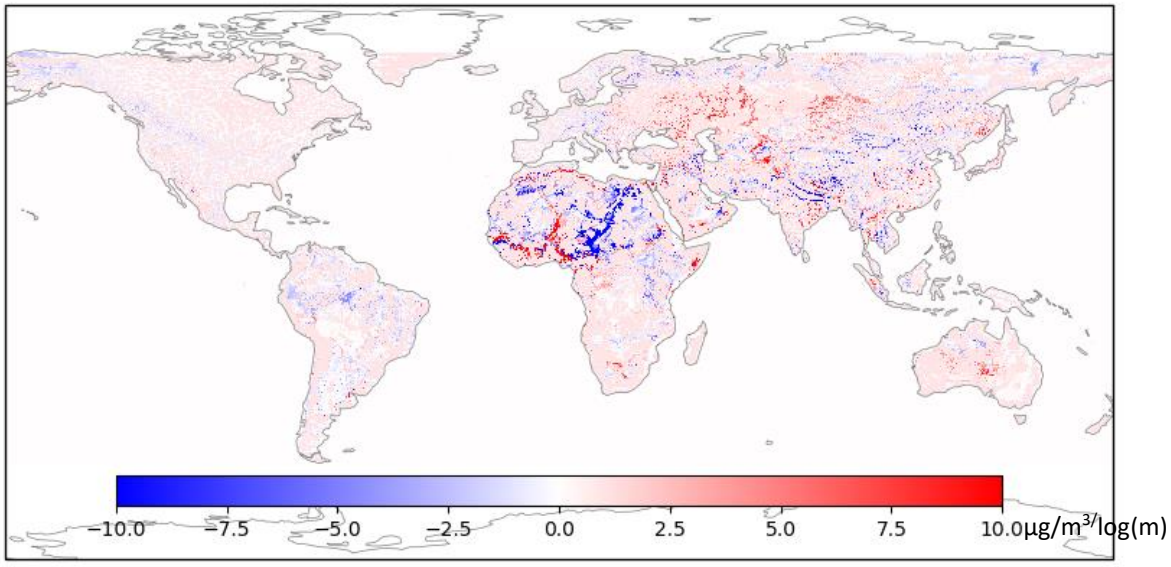

Figure S2-7 Elevation difference between local 0.1° and 2°x2.5° grid cell centre

Chapter S3 Unnormalized Relative Sensitivity Figures

Each figure shows the relative sensitivity of the mean PM2.5 predicted by the model to a single covariate, that is, the fractional local difference in the mean predicted by the model when the model has been perturbed by plus and minus 10%, divided by the size of the total perturbation range. In the case of lat and long, the perturbation of ±0.05°.

Latitude:

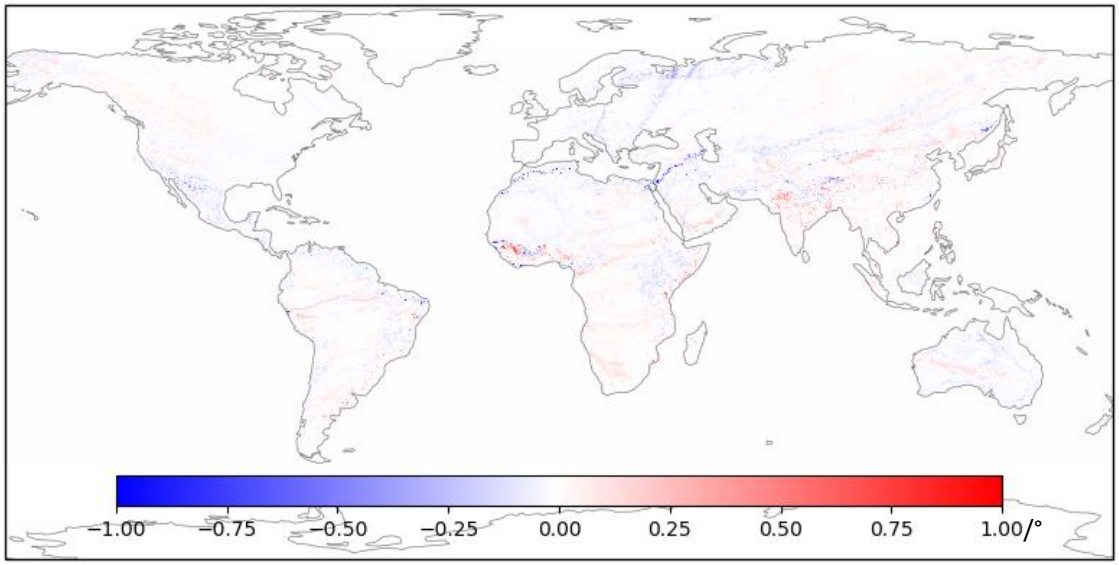

Figure S3-1 Sensitivity of PM with respect to Latitude

Longitude:

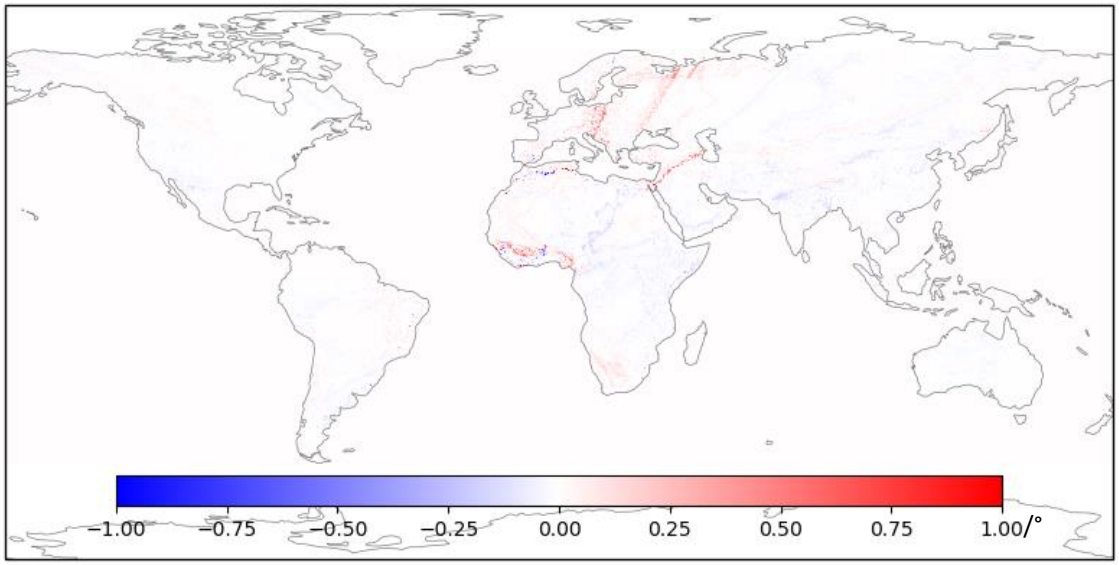

Figure S3-2 Longitude

Satellite-derived PM2.5:

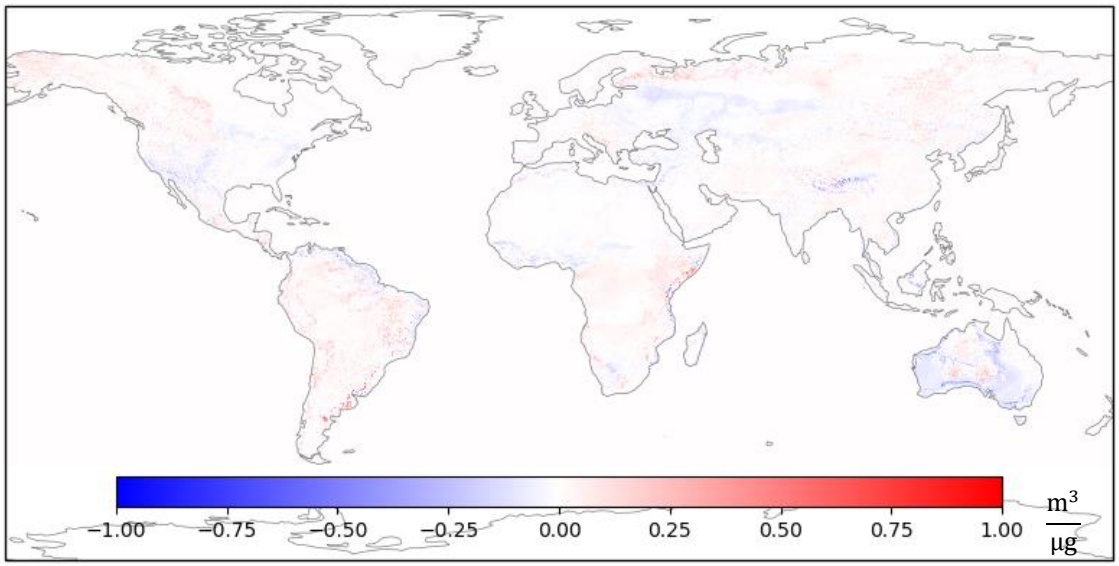

Figure S3-3 Satellite-derived $PM_{2.5}$

Dust fraction:

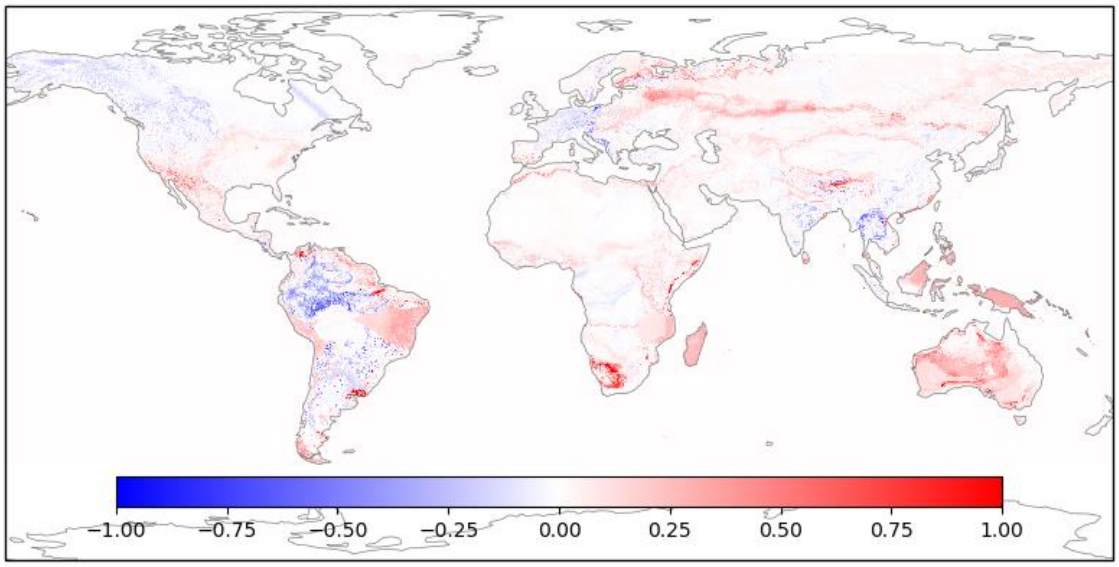

Figure S3-4 Modeled dust fraction

SNAOC fraction:

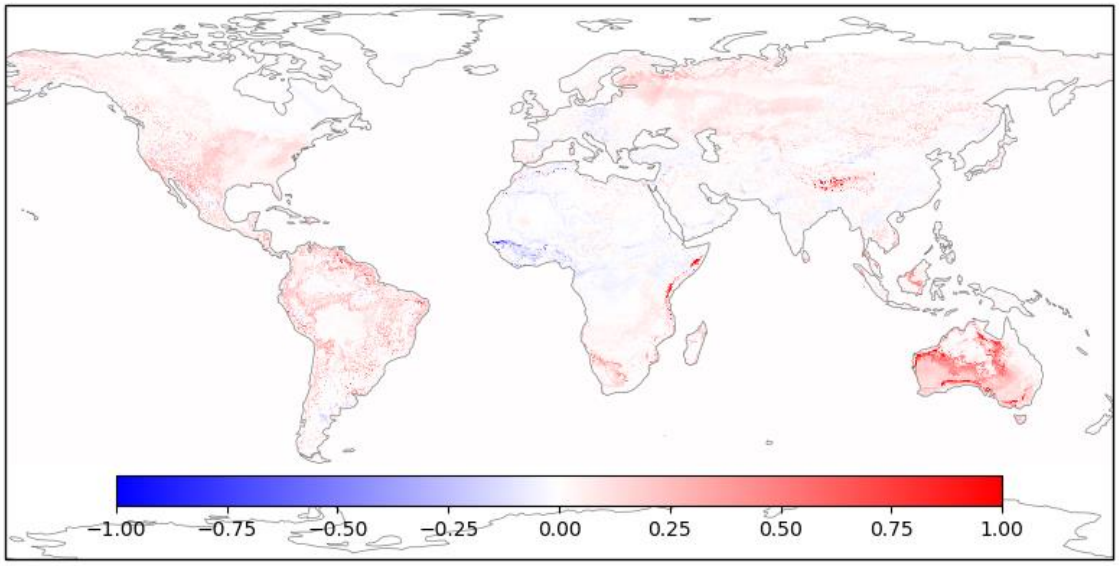

Figure S3-5 Modeled sulphate-nitrate-ammonia-organic carbon fraction

Distance to urban:

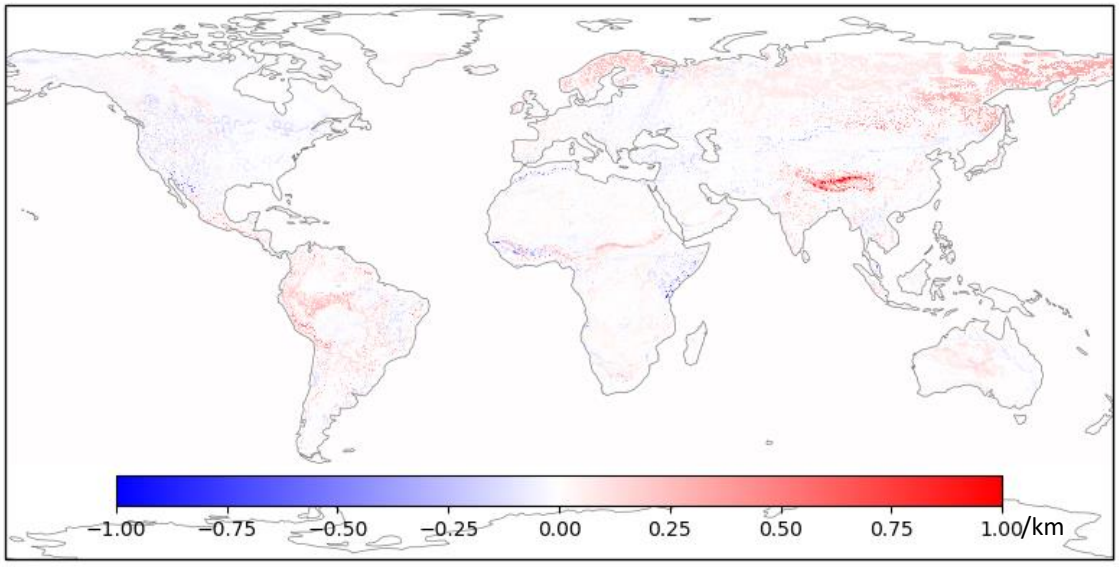

Figure S3-6 Distance to urban land type

Elevation difference w/2°x2.5° grid cell centre:

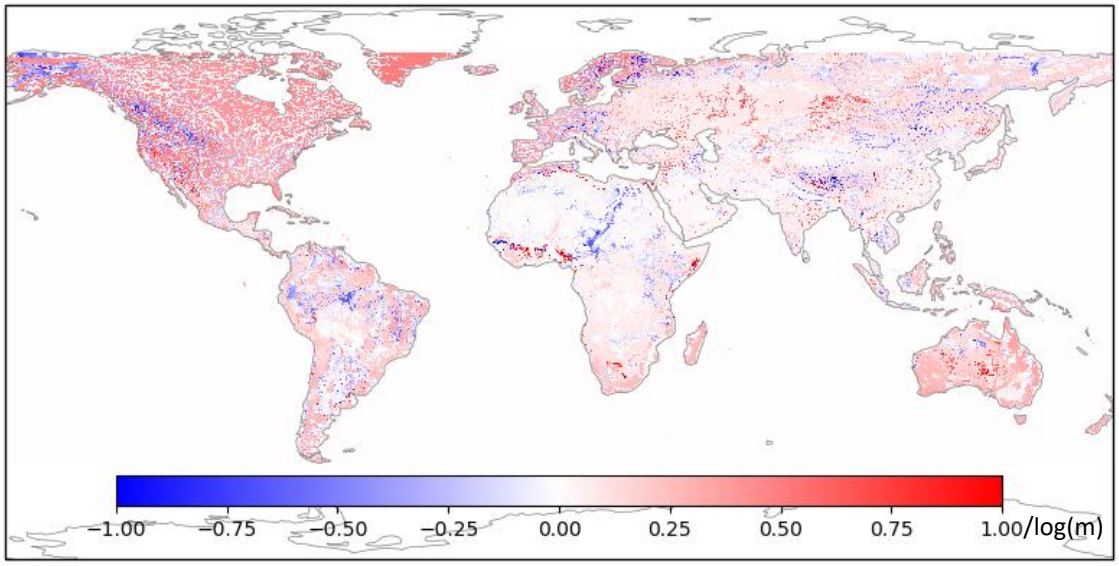

Figure S3-7 Elevation difference between local 0.1° and 2°x2.5° grid cell centre

Chapter S4 Uncertainty of naively trained ML model

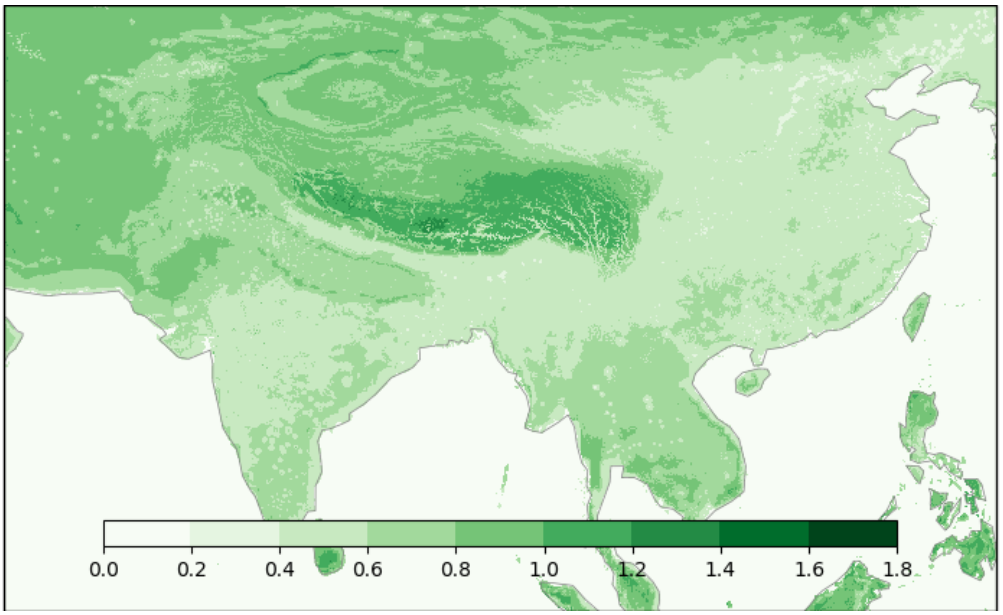

Figure S4-1 Relative standard deviation of WHO2018-trained model for South Asia

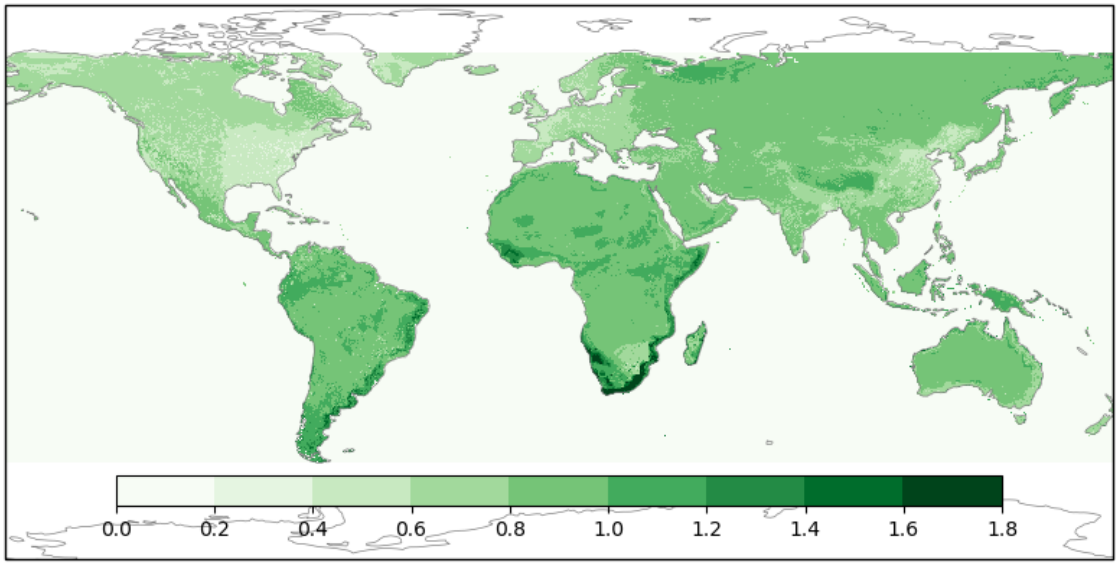

Figure S4-2 Relative standard deviation of predictions made by model trained on WHO2016 + satellite data.

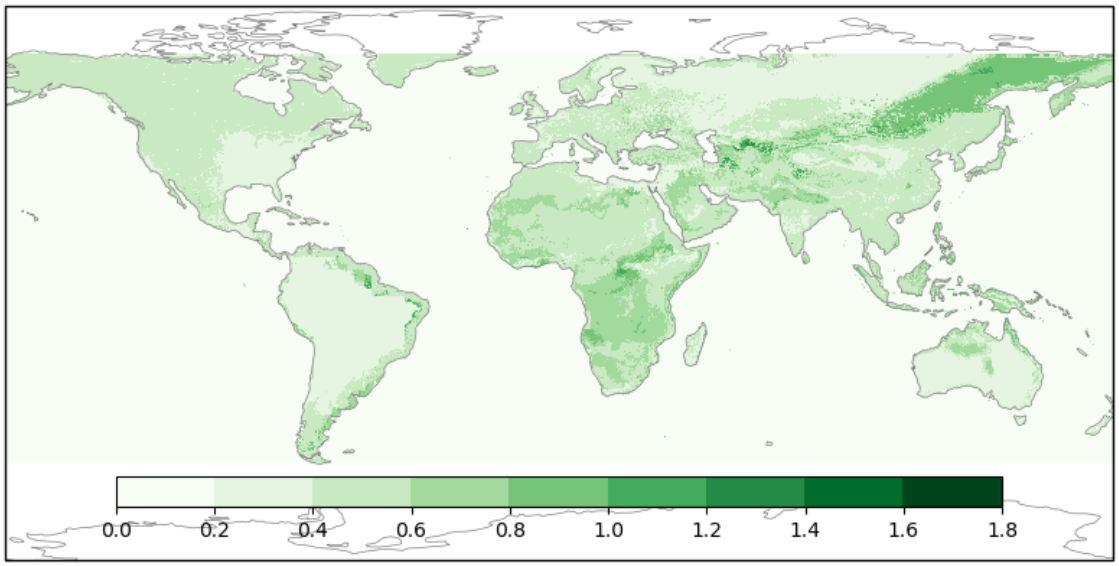

Figure S4-3 Standard deviation predicted by naively trained model using only WHO2018 data.